Modeling and Characterization of Coated Conductors Applied to the Design of Superconducting Fault Current Limiters

THÈSE N^{O} 4721 (2010)

PRÉSENTÉE LE 25 JUIN 2010

À LA FACULTÉ INFORMATIQUE ET COMMUNICATIONS

LABORATOIRE DE SYSTÈMES NON LINÉAIRES

PROGRAMME DOCTORAL EN INFORMATIQUE, COMMUNICATIONS ET INFORMATION

ÉCOLE POLYTECHNIQUE FÉDÉRALE DE LAUSANNE

POUR L'OBTENTION DU GRADE DE DOCTEUR ÈS SCIENCES

PAR

François ROY

acceptée sur proposition du jury:

Prof. M. Hasler, président du jury
Dr B. Dutoit, directeur de thèse
Dr T. Coombs, rapporteur
Dr J.-M. Moret, rapporteur
Prof. F. Sirois, rapporteur

ÉCOLE POLYTECHNIQUE
FÉDÉRALE DE LAUSANNE

Suisse
2010

Résumé

Le limiteur de courant supraconducteur est un appareil qui sera très probablement un composant essentiel des réseaux électriques du futur. Avec les récents progrès fait par les fabricants de rubans supraconducteurs, il y a actuellement un intérêt marqué venant de l'industrie à évaluer le potentiel d'un tel dispositif. Dans le présent travail de thèse, le comportement des supraconducteurs de seconde génération sous champs et courant de transport est étudié. Cette étude a été menée de façon expérimentale et numérique avec comme but de relier les phénomènes physiques observés dans les rubans supraconducteurs au design du limiteur proprement dit.

La transition résistive s'opère de façon non-uniforme dans les supraconducteurs à haute température critique. Dans l'optique de construire un limiteur de courant supraconducteur, il est essentiel d'obtenir une transition résistive rapide et uniforme lorsqu'un courant de défaut apparraît au travers de ces rubans, ceci afin de diminuer un échauffement local qui pourrait endommager le limiteur de courant, le rendant par conséquent inutilisable. Cette propriété de transition rapide est reliée à la vitesse de propagation de l'état normal (NZPV).

Dans ce travail de thèse, la vitesse de propagation est mesurée sur des rubans supraconducteurs commerciaux en utilisant un champ magnétique local comme initiateur de la transition. Pour des impulsions de courant d'amplitude sur-critique, des vitesses supérieures à 14 cm/s ont été mesurées.

Les expériences de propagation menée à des amplitudes de courant près de la valeur critique ont démontrés que la non-uniformité générée par le champ local aide à réduire le délai initial avant l'initiation de la propagation. Cependant, l'effet de la non-uniformité sur le délai devient moins important lorsque l'amplitude du courant de transport est augmenté puisque dans ce cas, la transition résistive s'opère plus par chauffage venant de la couche stabilisatrice (uniforme longitudinalement) et moins selon le seul avancement de la zone normale dans le supraconducteur (propagation longitudinale).

Toujours dans le cadre des mesures expérimentales, il a été observé que la réduction de la température du bain d'azote (sous-refroidie) augmentait les vitesses de propagation. Cet effet a été observé en tenant compte de l'augmentation du courant critique associé à la réduction de température. L'explication de cette augmentation de vitesse n'est pas encore établie avec certitude. Il pourrait s'agir d'un transfert de chaleur entre le dispositif et le bain environnant ou provenir de l'estimation de la variation du courant critique avec la température.

Afin de valider les modèles numériques utilisés dans ce travail, les traces de tension enregistrées lors des expériences de propagation ont été confrontées aux résultats obtenus des modèles. Ceux-ci sont basés sur l'équation de diffusion thermique et électrique. À partir des simulations, il a été démontré que la vitesse de propagation dans les rubans supraconducteur de seconde génération peut être augmentée de trois façons: en utilisant un substrat épais et diffusif thermiquement, en insérant une couche résistive à l'interface du stabilisateur et du supraconducteur et en augmentant la génération de chaleur dans le stabilisateur. À la lumière de ces résultats, il semble que la solution la plus prometteuse pour augmenter la vitesse de propagation serait l'insertion de la résistance d'interface. En effet, les simulations ont démontré que cette méthode augmente la taille de la région normale et permet de garder une température modérée lors de de la transition résistive des rubans.

Avec les modèles développés dans ce travail de thèse, le régime de “flux-flow” dans les rubans supraconducteurs de seconde génération a pu être simulé. En comparant ces simulations aux mesures expérimentales, il est apparu que la loi de puissance utilisée pour les modèles numériques était inappropriée lorsqu'utilisée pour modéliser le régime de “flux-flow” sous un faible champ magnétique externe. D'autre part, le rôle du transfert thermique transitoire n'as pas été formellement abordé dans ce travail. Son étude n'en est pas moins nécessaire afin de bien définir les spécifications du limiteur de courant supraconducteur.

Mots clefs: limiteur de courant supraconducteur, supraconducteur à haute température critique, supraconducteur de seconde génération, propagation de l'état normal, réseaux électriques.

Abstract

The Superconducting Fault Current Limiter (SFCL) appears to be a device of great interest to efficiently build the electrical grid of tomorrow. With the recent progress made by the superconducting wires manufacturers, there are needs coming from the industry to evaluate the potential of such devices. In the present thesis work, the behavior under external field and transport current of the last generation of wire is investigated. This study is conduct both experimentally and numerically in order to link the physics occurring at the wires level to the design of SFCLs as a whole.

From the nature of the material, the resistance appears non-uniformly in high temperature superconductors. For the purpose of building SFCLs it is important to obtain a fast and uniform resistive transition (quench) when a fault occurs through those conductors. This in order to reduce the local heat generation that may damage the device. This fast quenching property is related to the Normal Zone Propagation Velocity (NZPV).

In this work the NZPV is measured using a localized magnetic field to initiate quenches in commercial coated conductors. Those velocities have been measured to be larger than 14 cm/s for pulsed currents above the critical value.

The NZPV experiments have demonstrated that the superconductor non-uniformity (generated by the localized field) helps to reduce the initial delay before the quench initiation for transport currents in the range of the critical value. However, for larger transport currents the effect of the non-uniformity on the delay is less important since, with increasing transport current amplitudes, the normal state transition has shown to occur more as a consequence of the heat generated in the stabilizer than as the unique consequence of the advancement of the normal zone in the superconductor.

From the experimental measurements, it has been shown that a reduction of the liquid-nitrogen temperature (subcoooled) increases the NZPV. This effect has been observed taking into account of the increase of the critical current associated with the temperature reduction. Nevertheless, it is not clear if it is the heat transfer or the estimation of the critical current that is responsible for this effect.

In order to validate the numerical models, time-resolved voltage traces obtained from the experiments have been compared to the outputs of the models. Those are based on the thermal- and electrical-diffusion equations. From the simulations, it has been demonstrated that the NZPV can be increased by three methods: by using a thick diffusive substrate, by inserting a resistive interface between the superconductor and the stabilizer as well as by increasing the heat generation in the stabilizer. In light of those results, it seems that the insertion of a resistive layers is the most promising approach to improve the NZPV in coated conductors. As a matter of fact, a resistive interface increases the normal-zone size and keeps an acceptable temperature level along the conductor during quenches.

The present work allowed to simulate the flux-flow regime in coated conductors. Comparing those simulations to experimental data have shown that the power-law may be inappropriate to simulate this regime under weak external magnetic fields. In addition, it appears that the role of transient heat transfer with the surroundings needs to be studied in more details to determine the specifications of a prospected SFCL made of coated conductors.

Keywords: Superconducting fault current limiters, high-temperature superconductors, coated conductors, normal zone propagation, electrical grids.

Aknowledgments

Many thanks to: Bertrand, Frederic, Francesco, Louis, Michel and Mathieu as well as to the thesis jury. Also I would like to thank the LANOS, André and Peter. Thank to my flatmates Benoît, Mathias, Julie and Maïssa, my friends, my family and Laura.

Contents

Introduction **1**

1 From Superconductors to SFCLs **3**
1.1 Superconductors . . . 3
1.2 Coated Conductors . . . 9
1.3 Resistive SFCLs . . . 12

2 Characterization of Coated Conductors **15**
2.1 Experimental Setup . . . 15
2.1.1 Tape Resistance as a Function of the Temperature . . . 17
2.2 Samples Characterization Under Uniform External Magnetic Fields . . . 19
2.3 Normal Zone Propagation Velocity Initiated by a Localized Magnetic Field . . . 22
2.3.1 Effect of the Defect Strength . . . 24
2.3.2 Subcooled Experiments . . . 26

3 Modeling of Coated Conductors as Resistive-SFCL Elements **27**
3.1 Physical Concepts . . . 27
3.1.1 The Diffusion Equation . . . 27
3.1.2 Pool Boiling . . . 33
3.1.3 Thermal Stability . . . 36
3.2 The Numerical Model . . . 39
3.2.1 Finite Elements Method (FEM) . . . 39
3.2.2 The Coupled Model . . . 40
3.2.3 The Power-Law parameters . . . 41
3.2.4 Meshing and the Analytical Validation of the Thermal Part . . . 44
3.2.5 The Experimental Validation of the Coupled Model . . . 46
3.3 Simulation of Coated Conductors . . . 48
3.3.1 Substrate Thermal Properties . . . 49
3.3.2 Resistive Effects . . . 51
3.3.3 Heat Transfer and MQE . . . 55

Conclusion **59**

Appendix A. Materials Properties **61**

Appendix B. Green's Function of the 3D Homogeneous Heat Equation **69**

Appendix C. Estimation of the Minimum Propagation Zone (MPZ) **71**

Appendix D. Estimation of the Normal Zone Propagation Velocity (NZPV) **75**

Bibliography **85**

Introduction

FOLLOWING the projections of the International Energy Outlook [1], the total world consumption of marketed energy is projected to increase by 44 percent from 2006 to 2030. From this 44 percent, electricity is expected to be the fastest-growing form of end-use energy. This fact implies increasing power delivery on the electrical grids [2, 3, 4]. Consequently, in the near future, the current level under faults *i.e.* short circuits, lightning strikes or any sudden excessive current burst, is expected to largely exceed the ratings of interrupting devices composing the grids and thus, make faults management a major concern to meet the energy needs of tomorrow.

As a consequence of these larger fault currents, the electrical grids need to be upgraded, *e.g.* constructing new facilities or building higher-rated devices, to fulfill the regulation standards of the industry. This implies important capital investment and, for aesthetic and environmental reasons, generates public oppositions. However, those drawbacks may be circumvented by promising alternatives such as the Solid-State and Superconducting Fault Current Limiters (SSFCLs, SFCLs). As a matter of fact, those devices allow, by limiting current, to operate the grid at larger power flows and thus avoid the expensive replacement of the existent protection equipment. Accordingly, there are actually strong interests coming from different research institutions and industrial actors on those emerging technologies. For instance FCL projects are now conducted in many locations around the world *e.g.* Japan, Korea, Europe and United-States [5, 6, 7, 8, 9].

However, there are still obstacles to the commercialization of those emerging technologies. Concerning the SFCLs (for the present work, the word SFCL refers to the resistive type), a major difficulty concerns the slow and non-uniform resistive transition observed in the superconducting wires composing them. In light of this fact, the present thesis work concerns the numerical modeling and characterization of the normal zone propagation occurring in coated conductors (the last generation of superconducting cable). This study is conducted with the aim of improving tools to develop and design those conductors for SFCLs applications made of those conductors.

This dissertation is divided in three chapters. In the first chapter the relation between the behavior of High-Temperature Superconductors (HTS) submitted to transport current above the critical value and the SFCL operation is establish in order to formulate the propagation issue discussed above. To achieve that, the chapter is divided in three sections. The first section presents briefly the superconductors and the mechanisms at the origin of the resistive transition occurring in HTS. Then in the second section, coated conductors are introduced, those are the SFCL components studied in this work. The third section briefly presents the principle of operation of the SFCLs and illustrates the needs of obtaining large Normal Zone Propagation Velocities (NZPVs) in coated conductors to ensure the proper operation of SFCLs.

The second chapter presents the experimental measurements made on commercially available coated conductors. Those experiments allow obtaining the field dependence of a power-law parameters describing the resistive transition occurring in coated conductors under uniform external magnetic field and transport current. In addition, the experiments allow measuring the propagation of the normal state in the samples. The propagation is initiated by an artificial defect induced by a localized magnetic field.

The third chapter presents important concepts used to present the assumptions made in building the numerical model. Starting from those assumptions and from the field-dependent power-law pa-

rameters obtained from the experimental measurements, the numerical model is validated by a direct comparison of the voltage traces observed during the NZPV measurements. The validated numerical model is used to investigate the design parameters of the conductors to improve the NZPV in those conductors.

Note that the experiments and simulations realized in this thesis were all made with a current source and not under real short-circuit conditions, normally driven by a voltage source, such as in the power systems in which the prospected SFCLs are intended to be used. This convenient choice was motivated by the fact that this work focused principally on the behavior of the material composing the SFCL rather than on the interaction between the SFCL and the rest of the system.

Chapter 1

From Superconductors to SFCLs

THE Superconducting Fault Current Limiter (SFCL) presents unique characteristics inherited from the properties of superconductors. This chapter introduces basic elements of superconductivity that are used to present the origin of the electrical resistance occurring in the flux-flow regime in high temperature superconductors. Then are presented the coated conductors, the materials studied in this work. This chapter is concluded by a short description of the resistive SFCL and of the problematic of the low normal zone propagation occurring in coated conductors that represent a major obstacle to the commercialization of SFCLs made of those conductors.

1.1 Superconductors

Superconductivity is a state of the matter characterized by a weak attractive interaction between conduction electrons [10]. In this particular state, that occurs for many elements of the periodic system [11], this weak interaction reduces the system entropy and allows the in-phase motion of correlated-electrons over important distances. This long-range phase coherence is thought to be responsible of the perfect conductivity observed in superconductors. In addition to the zero-resistance hallmark, ideal superconductors are characterized by a perfect and reversible diamagnetism [12]. This special behavior is termed the Meissner effect *i.e.* the nonexistence of any magnetic flux into the material bulk for any initial conditions.

Those unique features of the superconducting state are overcome when an external input of energy (thermal, magnetic or kinetic) is sufficient to break down the fragile phase equilibrium. More specifically, the superconductor becomes a normal metal if the critical surface defined by the critical values (the temperature, magnetic field and current density) is reached – see figure 1.1.

Superconductors are classified in two main groups according to their behavior at the state transition. The left part of figure 1.2 presents the typical responses of these groups to an applied magnetic field. As depicted on the figure, the first group, termed type-I, shows a first-order transition *i.e* an abrupt and complete loss of the Meissner state at $H = H_c$, the thermodynamic critical field. This value is related to the maximal magnetic pressure the material can stand to hold the field out (condensation energy) [13]. For the second group, named type-II, the "pure" Meissner state exist only below a minimum field $H = H_{c1}$. Above this value, the magnetic flux start to penetrate the material. Once the penetration starts to occur the superconductor is said to be in the mixed-state (Shubnikov phase) which is a state characterized by the nucleation, in the superconductor, of normal metal filaments called vortex, each carrying a quantized magnetic flux Φ_0.

$$\Phi_0 = \frac{h}{2q} \approx 2.07 \times 10^{-15} \text{ Wb} \tag{1.1.1}$$

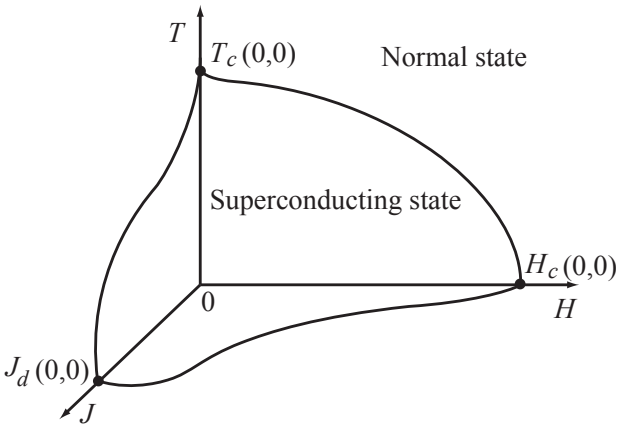

Figure 1.1: The critical surface given by the critical temperature T_c, magnetic field H_c and current density J_d delimit the superconducting and normal phases. Note that J_d is the depairing current, the energy at which the electron interaction vanishes.

Where h is the Planck constant and q the electron charge. For type-II superconductors, the flux penetration allows a second-order phase transition (continuous) that reduces the energy needed to hold the field out. This allows the complete penetration of the magnetic field to occur at a larger field H_{c2} than the thermodynamic critical value H_c. Note that H_{c2} is reached when the whole material is covered in vortices *i.e.* when the material is completely transparent to the external field.

Type-II superconductors show a larger range of operating temperatures and fields than type-I – see table 1.1 on page 5. This is the basic reason why most of the actual applications involving superconductors are currently made of type-II. This is also the type of conductor studied in this work.

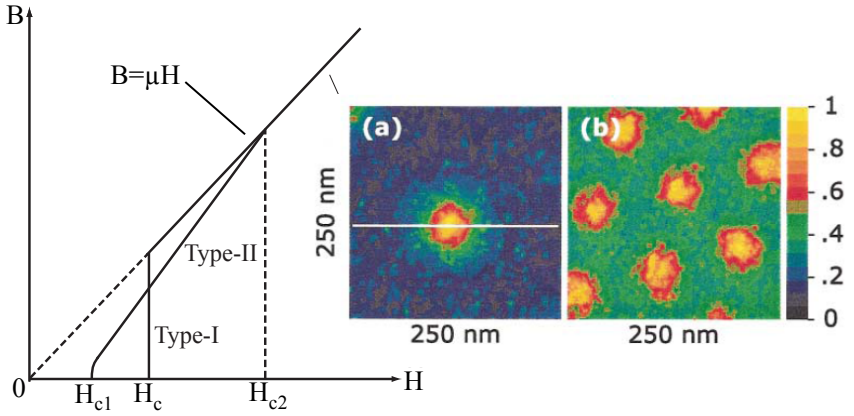

Figure 1.2: On the left is the B-H phase diagram for type-I and type-II superconductors. The superconductor is in the Meissner state when the magnetic flux B is zero for a given applied magnetic field H. Note that the figure is not to scale. For usual type-II superconductor, H_{c1} is more than 10 000 times smaller than H_{c2}. On the right, the colored picture shows vortices in MgB_2 [14]. (a) 250×250 nm^2 false color STS (Scanning Tunneling Spectroscopy) images of a single vortex induced by an applied field of $B_a = \mu_0 H_a$ =50 mT, (b) the vortex lattice at 200 mT. Each vortex carries the quantum flux Φ_0.

Classification and Applications of Superconductors

Table 1.1 lists some characteristics of chosen superconductors. Type-II superconductors are separated in two categories *i.e.* LTS or HTS for Low- or High-Temperature Superconductors according to their critical temperature which is respectively below or above 30 K. This value corresponds to the transition temperature of the Ba-La-Cu-O system, the first HTS discovered by J.G. Bednorz and K.A Müller in 1986 [15].

Up to now, most of the superconductors applications are related to high-field magnets and/or low field measurements *e.g.* Magnetic Resonance Imaging (MRI), Superconducting Quantum Interference Devices (SQUIDs), Magneto-Encephalo-Graphy (MEG), Nuclear Magnetic Resonance (NMR) or high-energy physics accelerators. Those applications are currently made of LTS making this class of conductor the most widely used for technological purposes [16]. Nevertheless, the discovery made by J.G. Bednorz and K.A Müller of superconductivity in cuprates at the end of the 80's initiates the age of HTS [15]. The benefit of working at the liquid nitrogen boiling temperature is probably the most important driving-factor influencing the R&D for applications involving HTS. As a matter of fact, for any application in which liquid nitrogen can replace liquid helium, the refrigeration cost is about 100 times less [17]. Thus, HTS seems to promise a broader range of practical applications than LTS in the near future [18, 19, 16].

Table 1.1: Classification of chosen superconductors.

Type	Material	T_c [K]	B_c or B_{irr} [T]*	Characteristics
I	Al	1.2	0.01 @ 0 K	Metallic/ductile
	Pb	7.2	0.08 @ 0 K	Metallic/ductile
II-LTS	NbTi†	9	10 @ 4.2 K	Metallic/ductile
T_c <30 K	Nb_3Sn‡	18	20 @ 4.2 K	Metallic/brittle
II-HTS	MgB_2	39	5.5 @ 20 K	Anisotropic, Ceramic/brittle
$T_c \geq$30 K	$Bi_2Sr_2Ca_2Cu_3O_{10}$	110	5 @ 26 K	Anisotropic, Ceramic/brittle
	$Bi_2Sr_2Ca_1Cu_2O_8$	85	5 @ 16 K	Anisotropic, Ceramic/brittle
	$YBa_2Cu_3O_7$	90-92	9 @ 86 K	Anisotropic, Ceramic/brittle

* References: [12, 20, 21]. B_{irr} is the irreversibility flux, see the next subsection for its definition.
† Material used for the Large Hadron Collider (LHC) setup [22].
‡ Material expected for making the coils of ITER [23].

Flux Pinning and the Irreversibility Field

For the purpose of this work, the material under study (HTS) is always in the mixed-state. In that state the electrical resistance appears as a consequence of the Lorentz force which makes moving the flux-lines (vortices) when a transport current is applied to the conductor [24, 26, 10]. The dissipation (resistance) can be attenuated if the flux-lines are stopped in their motion by impediments such as grain boundaries or impurities. Under these circumstances, vortices are said to be pinned. Pinning is essential to ensure the proper operation of type-II superconductors. As a matter of fact, one can relates pinning forces to the critical current of a superconductor (different than the depairing current [27]). This relation comes from the fact that, due to circulating current present around vortices, flux-lines repel from each other [12]. Consequently, considering a vortex pinned somewhere in the material, the repulsion impedes the movement of other vortices in its neighborhood and thus a larger amount of current is needed to rise the resistance of the material. From a macroscopic point of view, at the N pinned vortices per unit volume is associated a pinned force f_p which is proportional to the local critical current j_c.

$$f_p \propto j_c N \Phi_0 \tag{1.1.2}$$

If the driving force per unit volume *e.g.* the number of vortices (H), the thermal agitation (T) or the Lorentz force (J), exceeds the pinning force available in the same volume, it is thought that all the pinned vortices of the volume are going to move at once (the flux movement occurs in bundles [28]). This scheme subdivides the mixed-state in two sub-states. One in which vortices are hold in place by mutual repulsion and impediments and the other in which vortices are moving freely without feeling any force. Those two sub-states are respectively termed the vortex-glass state (large J_c) and the vortex-fluid state ($J_c \approx 0$) [24]. The line delimiting those two states is named the irreversibility line, the line above which high dissipation occurs. The origin of this term "irreversibility" comes from the fact that flux pinning is responsible for hysteresis effects in superconductors – see figure 1.3. As a

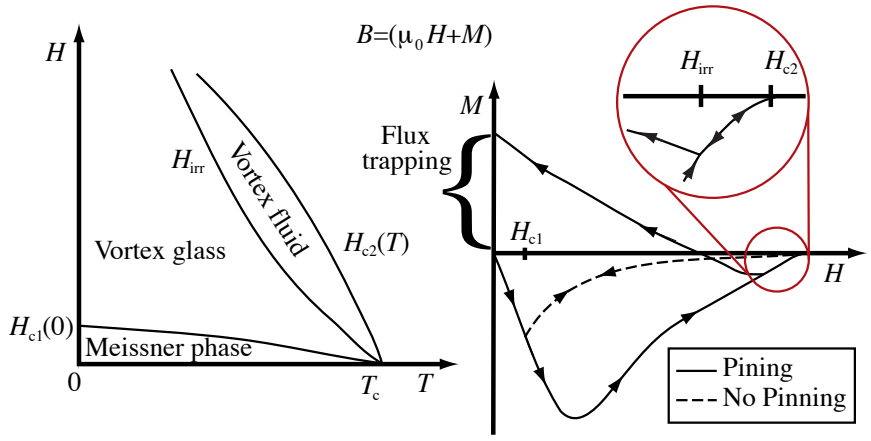

Figure 1.3: On the left is an hypothetical H-T phase diagram for type-II superconductors. Above the irreversibility line (vortex fluid sub-state) vortices are all moving and dissipation occurs. This kind of diagram can be very complicated – for instance see [24, 10]. The right figure displays a fictitious magnetization curve for type-II superconductors with and without pinning [12, 25]. Below H_{c1}, the magnetization M exactly compensates the external magnetic field ($B = 0$) for both cases (with and without pinning). Nevertheless, the effect of pinning hinder the movement of vortices into the bulk of the material, allows larger magnetization than without pinning (M is not minimum at H_{c1}) and leads to hysteresis effects when the field is reduced from H_{irr}. Note that between H_{irr} and H_{c2}, the magnetization curve is reversible since vortices are free to move. In real type-II superconductors, the magnetization is never totally zero when $H = 0$, since flux-lines are trapped in the material. Finally, note that for a perfect type-II superconductor *i.e.* without pinning (dashed line), the magnetization is always reversible up to H_{c2}.

matter of fact, the material imperfections are thought to trap field-lines and influence the magnetization curve [12, 25]. Above a certain field value $H = H_{\text{irr}}$, the flux-lines are not pinned anymore and the reversible behavior of superconductors is restored.

Since type-II High Temperature Superconductors (HTS) generally operate at relatively high temperatures, H_{irr} is smaller than H_{c2} in those conductors (pinning is reduced by thermal activation). Pinning allows to improve the current carrying capability of the conductors under large magnetic field [29]. It is the reason why increasing pinning in HTS is one of the main goal of the wire manufacturers. Section 1.2 introduces the technological methods used to produce these conductors.

A Macroscopic Model

Due to thermal activation, the movement of flux-lines in HTS occurs even without applied field (trapped vortices) or transport current [25, 10]. Thus, the theoretical models used to describe the state transition in those conductors need a deep investigation of the vortex dynamics [24, 26]. However, those models can be simplified if the HTS is submitted to transport currents above the critical value where all the flux-lines are moving. Under this condition, the superconductor is in a dissipative regime termed flux-flow. This regime is characterized by a linear variation of the E-J curve such that the electrical field is proportional to the number of vortex present in the superconductor up to the normal state *i.e.* when the flux-flow resistivity (ρ_{ff}) equals the normal resistivity (ρ_n).

$$E = \rho_{\text{ff}}(H,T)\big(J - J_c\big), \qquad \text{Where, } \rho_{\text{ff}}(H,T) = \rho_n \frac{H}{H_{c2}(T)} \tag{1.1.3}$$

However, obtaining the fraction of conductor covered by flux-lines in motion is not obvious. Accordingly, empirical models are often used to describe the flux-flow regime at a macroscopic scale [30, 31]. For the purpose of this thesis, the flux-flow regime is described by a power-law which gives the behavior of the electrical field as a function of the transport current density passing through the material. The following equation represents the power-law without temperature and magnetic field dependence.

$$E = E_0 \left(\frac{J}{J_c}\right)^n \tag{1.1.4}$$

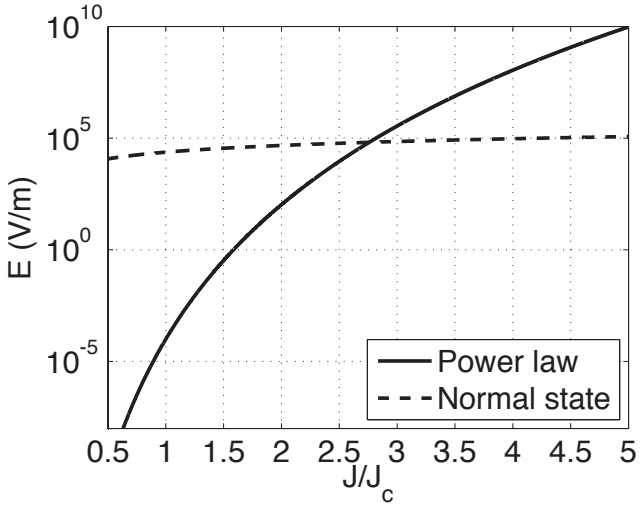

Figure 1.4: Evolution of the electrical field as a function of the transport current density for a power-law with n=20. Considering a normal resistivity of $\rho_n = 100 \times 10^{-8}$ Ω.m, the normal state occurs along the dashed-line. This implies that for a fixed temperature and magnetic field *e.g.* $T = T_{\text{op}}$ and H =0 T, the normal state is reached at a ratio of J/J_c equals to 2.76.

Where, E_0 is the critical field which is usually defined to be 1μV/cm. The exponents n, as well as J_c are values obtained from fits to experimental data. Figure 1.4 shows the behavior of equation 1.1.4 without field and temperature dependence. From figure 1.4, one can see that the power-law is characterized by a non-zero resistance below the critical current that rapidly reaches the normal resistance above J_c. Note that equation 1.1.4 do not shows temperature and magnetic field dependence. For this reason, the normal state is reached at large ratio of J/J_c. For example, with $\rho_n = 100 \times 10^{-6}$ Ωm, the system described by the power-law reaches the normal state at $J =$2.76J_c. Thus, the thermal and magnetic dependences must be added to the models to make it accurate.

1.2 Coated Conductors

Since the beginning of the 90's type-II HTSs have been successfully designed as wires for power applications. The first success was achieve using the Powder In Tube technique (PIT) [32]. Except for the special case of MgB_2, PIT is only found to work with the bismuth compounds (BSCCO) which have a plate-like morphology after the process. However, at liquid nitrogen temperatures, the critical current of such compounds rapidly drops with weak external magnetic fields [33]. Accordingly, PIT-wires must be cooled to temperatures in the neighborhood of 20-30 K for usual high-field applications. The large amount of silver needed to ensure the proper operation of those wire (The PIT method is basically a silver tube filled with HTS powder) as well as the range of operating temperatures make those conductors expensive. This is why PIT-wires are now relegated to the first generation of cables.

To overcome the huge variation of the critical current occurring in presence of external fields, it as been thought to use (Re)BCO compounds instead of bismuth-based materials. Here (Re) refers to rare-earth elements such as yttrium, lanthanum, dysprosium etc. The most common (Re)BCO compound is made of yttrium *i.e.* $YBa_2Cu_3O_{7-x}$ or simply YBCO [34]. It can be deduced from figure 1.5 that YBCO have better intrinsic flux pinning and irreversibility field than BSCCO. In addition, YBCO is able to carry high currents in strong magnetic fields while being cooled by liquid nitrogen [17]. However, YBCO is brittle and highly anisotropic which implies that electric current does not flow well from grain to grain if the conductor is not perfectly aligned. Accordingly, it has been thought to epitaxially grow YBCO coating on metallic strips [35, 36, 37]. This has led to the emergence of the second generation (2G) of conductors named coated conductors [38].

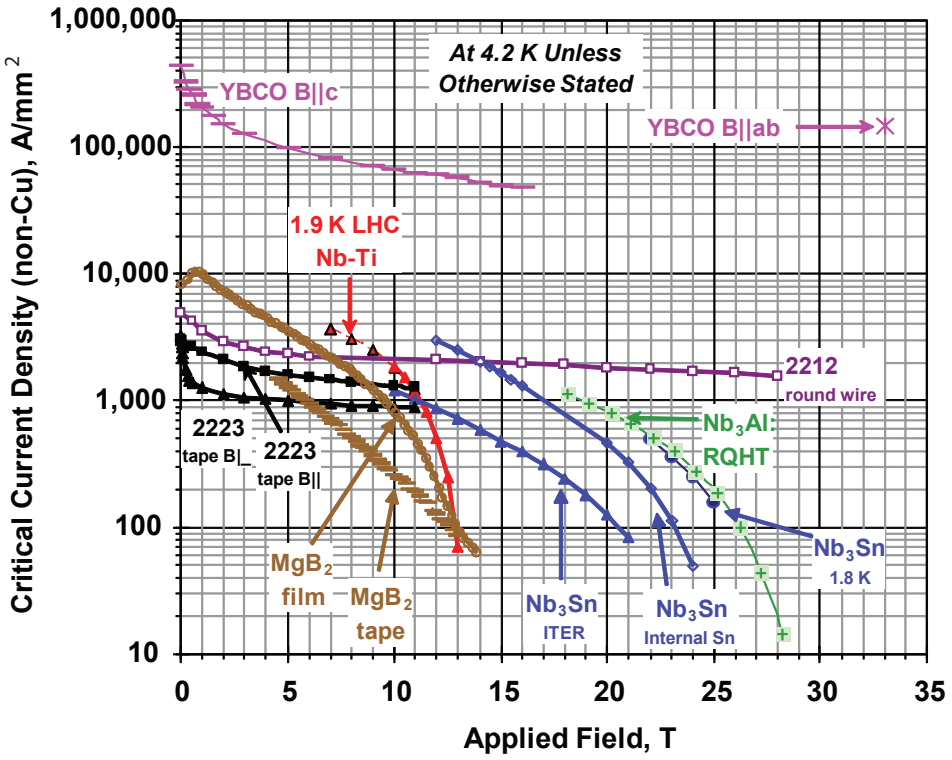

Figure 1.5: Critical current as a function of external magnetic flux for different type-II superconductors [39]. 2223 and 2212 refer respectively to the two usual phases of BSCCO encountered in applications: $Bi_2Sr_2Ca_2Cu_3O_{10}$ and $Bi_2Sr_2Ca_1Cu_2O_8$. This figure shows the larger range of applicability of YBCO.

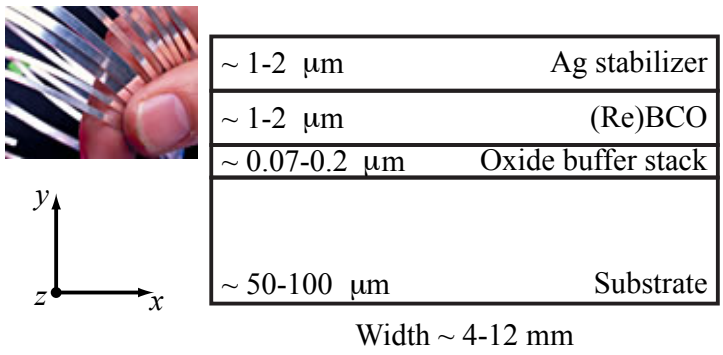

Figure 1.6: Non-scaled cross-section of a typical coated conductor (without copper cladding). The picture at the left shows the actual size of those wires. Note that this kind of wire can carry DC current even larger than 100 A without any losses. Picture from the CCAS website [16].

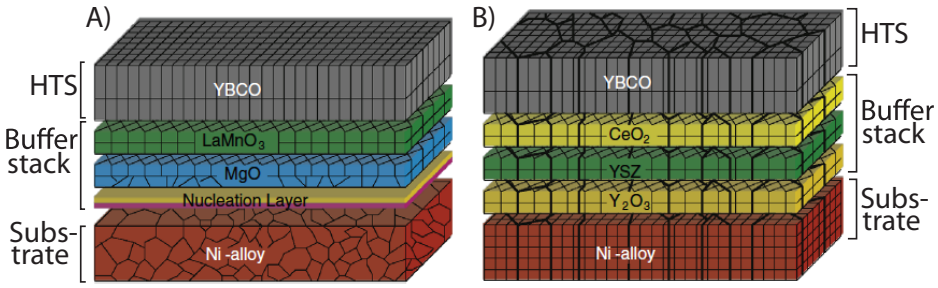

Figure 1.7: Non-scaled pictures of the IBAD (A) and RABiTS (B) conductors without stabilizer [40]. The template for the growth of the YBCO layers is ensured by the buffer stack in the IBAD method. For the RABiTS method this role is ensured by the substrate.

Coated conductors are basically an assembly of layers. From a very simplified view, those conductors are constituted of a thick and electrically-resistive substrate, a stack of oxide buffer-layers, a superconducting film and an electrically-conductive metallic layer *i.e.* the stabilizer – see figures 1.6 and 1.7. Each layer has its own role. For instance, the substrate gives a flexible and smooth mechanical support to the brittle superconductor and also helps thermal stabilization. The buffer layers align the anisotropic HTS and isolate the superconductor of chemically active compounds. The role of the stabilizer is to reduce the heat generation in the superconductor by diverting current (as a shunt resistance) once it becomes normal as well as to reduce the voltage overshoot during quenches. The stabilizer in contact with the HTS is usually made of noble metals such as silver or gold in order to avoid chemical reaction with the superconductor. Finally, note that manufacturers often encapsulate the wires in a copper cladding to reduce the tape overall resistance *i.e.* the temperature excursion while the wire is in the normal state.

There are basically two leading technologies to align grains in (Re)BCO. The Ion-Beam Assisted Deposition (IBAD) [36] and the Rolling-Assisted Bi-axially Textured Substrate (RABiTS) [37]. Each of them are respectively used by two of the actual leading superconductors manufacturers that are SUPERPOWER.INC [41] and AMERICAN SUPERCONDUCTOR.CORP (AMSC)[42].

SUPERPOWER produces coated conductors using the IBAD-MGO/MOCVD technique [43]. The epitaxial (Re)BCO film is grown by Metal Organic Chemical Vapor Deposition (MOCVD) on highly oriented buffer layers (basically $LaMnO_3$/MgO – see figure 1.7) where the MgO layers is obtained by IBAD (bombarding the growing film with an 45° oriented ion-beam of argon). The buffer-stack is deposited on an smooth electro-polished commercial alloy named Hastelloy® (substrate).

AMSC uses the RABiTS/MOD method [37]. The epitaxial (Re)BCO film is grown by Metal Organic Deposition (MOD) on buffer layers (figure 1.7) deposited over an highly oriented nickel-

tungsten substrate obtained by a series of mechanical (rolling) and thermal treatments (annealing).

Coated conductors are still under development. At the time of writing this thesis, research carried at SUPERPOWER is oriented on the removal of the electro-polishing step. They are developing a substrate planarization method to increase the throughput and allows the use of different materials as substrate. They are also reducing the amount of silver that usually covers HTS films to reduce cost and processing time. AMSC orients their work on a new tri-layers composite substrate in order to reduce ferromagnetic losses. They also wish to produce thicker film at a larger fabrication rate. Both companies still do research to enhance pinning using nanostructured dopants [29]. The interested readers can follow the recent developments obtained for 2G wires along the frame of the DOE HTS program [9].

1.3 Resistive SFCLs

SFCLs are devices that present a unique feature: they sit at low impedance nearly all the time in normal-operation (they are almost transparent to the grid) but switch rapidly to high impedance without any external trigger when a fault occurs.

Basically, a resistive SFCL is a superconducting wire. One way of using a SFCL in a power circuit is to place it in series with a current breaker – see figure 1.8. Considering that circuit but without SFCL, the current in the power lines can easily reach ten times the current normally carried when a fault occurs *i.e.* when the load impedance Z_l becomes very small. With the SFCL insertion, a notable increase of the system impedance is automatically triggered. This leads to a reduction of the current flowing in the circuit. Figure 1.9 displays the effect of the SFCL on the current waveform during a typical fault event [44].

The huge amount of energy to be dissipated during the fault period (t_d) and the maximum permissible temperature rise of the conductors are the fundamental specifications for an SFCL [25, 45]. Nevertheless, most of the time, a SFCL is not in the fault-current mode. Accordingly, other design parameters are needed to ensure a very low impedance of the device in its normal-operation mode. For sake of completeness, a non-exhaustive list of design parameters is dressed here. Some other can be found in the specialized literature [6, 44, 4, 7]:

- Rated voltage and current V_L, I_r
- Maximum limited current I_f, Fault duration time t_d, System inductance
- Maximum allowable temperature T_{max} (the SFCL basically absorbs power)
- Operating temperature/pressure T_{op}, p_{op}
- Normal-operating mode impedance (AC- and current-leads-losses)
- Safety, Environment
- Cost (cooling, maintenance etc.)

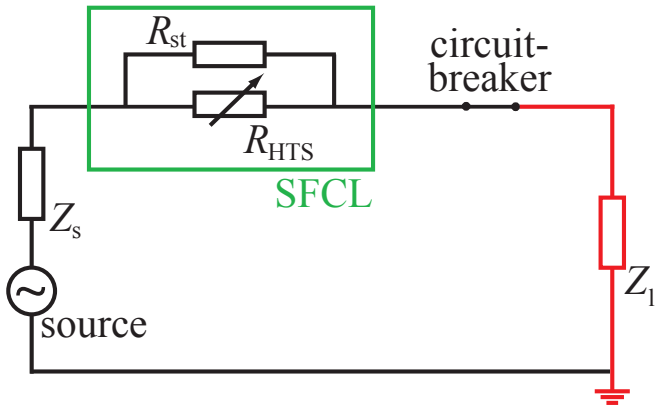

Figure 1.8: The basic concept of a resistive SFCL (a superconducting wire). When a fault occurs, the SFCL becomes resistive and reduces the current in the circuit up to the opening of the breaker. R_{HTS} and R_{st} refers respectively to the superconductor and stabilizer resistance.

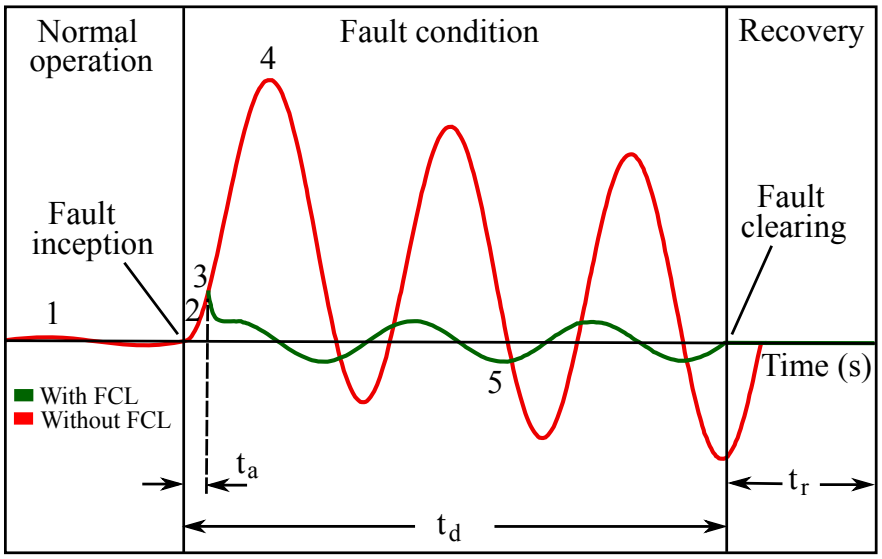

Figure 1.9: The effect of a SFCL on the current waveform during a typical fault event [44]. The points (1) to (5) represent the characteristics parameters of the fault event. Respectively: The peak rated current (1), the minimum initiated current (2), the maximum limited current (3), the peak short-circuit current (4) and the peak follow-current (5). The action time (t_a), is the elapsed time from fault initiation to the maximum limited current (3). The duration time (t_d) is the elapsed time from fault inception to fault current interruption and the recovery time (t_r) defines the time needed by the conductor to cool down and recovers the superconducting state. The phase shift and current asymmetry observed in the red curve are coming from the transient response of the system that decay exponentially with the ratio X/R where R and X are respectively the resistance and reactance of the system. With the SFCL addition, the resistance of the system increase rapidly and thus reduces the time constant of the transient response. It is why the phase shift and asymmetry effects are not observed for the green current waveform (with an inserted SFCL).

The Superconducting Properties of a SFCL

Besides the above design parameters, the question of interest, and the aim of this work, is to know how the wires superconducting properties may affect the design of a SFCL. A description of an idealized SFCL may helps to start this analysis.

From the fundamental SFLC specifications, one may define the maximum allowable energy the device can stand for a period $\Delta t = t_d$.

$$E_{max} = \int_V \int_0^{t_d} P_{max} dt' dV' \leq Q_{st} + Q_c \,, \tag{1.3.1}$$

where Q_{st} is the energy stored in the system of volume V and specific heat C_p up to T_{max}

$$Q_{st} = \int_V \int_{T_{op}}^{T_{max}} C_p(T) dT' dV' \,. \tag{1.3.2}$$

Q_c is the heat transfer with the surrounding and P_{max} is the allowable power generation in the conductors *i.e.*

$$P_{max} = R I_f^2. \tag{1.3.3}$$

The maximum limited current is expressed as:

$$I_f = F I_q \tag{1.3.4}$$

Where F, is an arbitrary factor and I_q is the minimum initiating current *i.e.* the current needed to uniformly quench the superconductor. For sake of simplicity, one may consider that the uniform

transition occurs at the tape depairing current (I_d) *i.e.* the current that just breaks the thermodynamic equilibrium.

$$I_q = I_d \tag{1.3.5}$$

Hence, considering that the normal resistance of the superconductor is much larger than the stabilizer resistance ($R_n \gg R_{\text{st}}$) the resistance of the SFCL is approximately:

$$R = \begin{cases} 0 & I_f < I_q \\ R_{\text{st}} & I_f \geq I_q \end{cases} \tag{1.3.6}$$

where R_{st} is the stabilizer resistance (the SFCL is considered here to be only constituted of parallel superconducting wires). Using 1.3.4 to 1.3.6 and, for simplicity, supposing F =1, equation 1.3.3 becomes

$$P_{max} = R_{\text{st}} I_d^2 \, . \tag{1.3.7}$$

For this idealized case, one can note that the SFCL superconducting properties only fix the fault level and the stabilizer specifications. Note that a large I_d allows to reduce the length of conductor (L) needed for the proper SFCL operation ($R_{\text{st}} \propto L$).

The former analysis is, by far, an over-simplification of the problem. As a matter of fact, the flux-flow resistivity creates losses even below the depairing current and thus participates in the limiting action. In addition, the statistical nature of pinning as well as the difficulty to obtain nano-engineered structures for long lengths make the superconductor response dependent of localized flaws in the material. For fault current in the range of the critical current, weaker regions of the conductors become resistive before other part of the tapes and may locally generate heat without triggering the whole quenching mechanism. For this range of current, the SFCL transition is strongly dependent of the superconducting properties of the wires composing it. Consequently, the quenching mechanism depends on how fast heat generated in the resistive flaws propagates through the material to make the remaining of the tape quenching. This last property is related to the Normal Zone Propagation Velocity (NZPV) which is also the main investigation of this work.

In summary, considering its superconducting properties, a SFCL has to switch rapidly and uniformly to the normal state when a fault occurs and diffuses heat away from weaker zones in order to avoid local damage of the device and reach the idealized behavior presented before.

Chapter 2

Characterization of Coated Conductors

THIS chapter presents the experimental manipulations made on coated conductors. The aim of those experiments is to characterize the resistive transition and normal zone propagation occurring in these conductors under uniform and localized external magnetic fields. This is done in order to determine the field dependence of the power law parameters *i.e.* $J(B)$ and $n(B)$ as well as to develop the numerical model presented in the next chapter. All the measurements are made on SUPERPOWER tapes [41] with pulsed currents of different length and amplitude (above the critical current). This chapter is basically divided in three sections. The first section presents the experimental setup used in this thesis work. The second section, the behavior of coated conductors under uniform external magnetic field. The third section, the measurements of the normal zone propagation in those commercial tapes initiated by a localized magnetic field (local reduction of the critical current).

2.1 Experimental Setup

The setup allows measurements under magnetic field (0-500 mT) and/or at low pressure (0.1-1 atm). The apparatus – see figure 2.1 is basically a 900 mm long cylindrical cryostat (diameter of 50 mm) which crosses the air-gap of a commercial magnetic dipole (μ-BEAM.Sàrl). The latter is composed of 2 coils of 410 turns able to produce DC-magnetic flux as large as 500 mT for an air-gap of 60 mm. The dipole can rotate around the cryostat and allows the user to change precisely the transverse component of the external magnetic field. The cryostat, that is connected to a mechanical pump, is closed and sealed with Teflon® cap, elastomer and vacuum grease. The sealing allows to reduce the pressure down to ≈20 kPa in the cryostat. The Teflon® cap is traversed by the current leads that are connected to a voltage-driven source [46] (Techron-7780RLY, slew rate of 40V/μs) able to sustain DC current as large as 180 A for few seconds (1 Ω load). Those current leads tie the sample holder at the vertical (along the cryostat length). The latter is basically a printed circuit board (PCB) mounted on the current leads and placed in the dipole air-gap (60 mm). Multiple probes, used for different purposes are connected to the sample holder –see figure 2.2. For a typical setup one can find more than 16 voltage taps, 2 Cryogenic Hall-probes (Lakeshore HGT-2100), 3 thermocouples (type-T) as well as 1 silicon diode (Lakeshore DT-470). The electrical signals from the probes (up to 16 differential signals) are simultaneously monitored with a 18 bits, 625 kS/s NATIONAL INSTRUMENTS™ data acquisition card (USB-6719) [47]. External devices such as temperature controller (Lakeshore DRC-91C), oscilloscope (LeCroy-9334), voltmeters (HP-34401) and DC-power-supply are controlled through a General Purpose Interface Bus (GPIB) and some virtual instruments (LABVIEW® [47]).

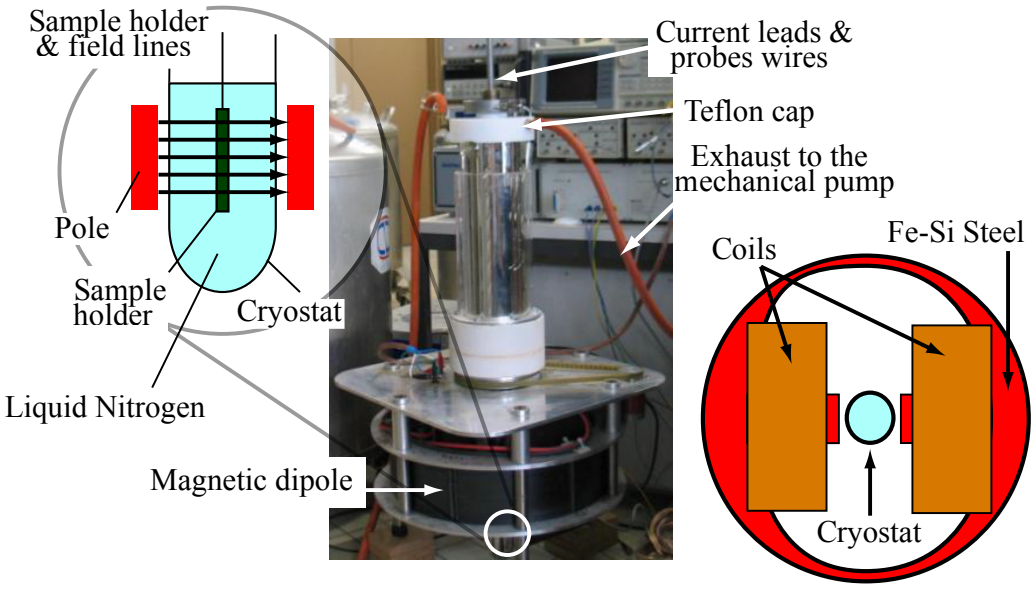

Figure 2.1: Experimental setup. The cryostat crosses the air-gap of the magnetic dipole. The top-left inset shows the location of the sample holder in the dipole air-gap as well as the resulting field-lines coming from the dipole. The bottom-right inset shows a slice-view of the magnetic dipole and cryostat.

The 4 mm wide samples used in this work are basically composed of an hastelloy substrate of 50 μm thick, a buffer stack of approximately 70 nm, a YBCO layer of 1 μm and a silver stabilizer of 2 μm. For the measurements, the samples are divided in sections delimited by small aluminum wires (diameter 26 μm) soldered at the stabilizer surface and acting as voltage taps (figure 2.7 illustrates those ones). The sections are approximately 1 mm long (except for the NZPV measurements –see section 2.3). At the early stage of the flux-flow regime, the voltages monitored in such a small distance are very small. Accordingly two additional taps located 36 mm apart, at the tape ends, are used to increase the signal resolution (tpL1 and tpL2, section 0). The current return is made of a silver strip placed above the superconductor in order to reduce the bending force on the sample as well as to reduce induction effects– see figure 2.2.

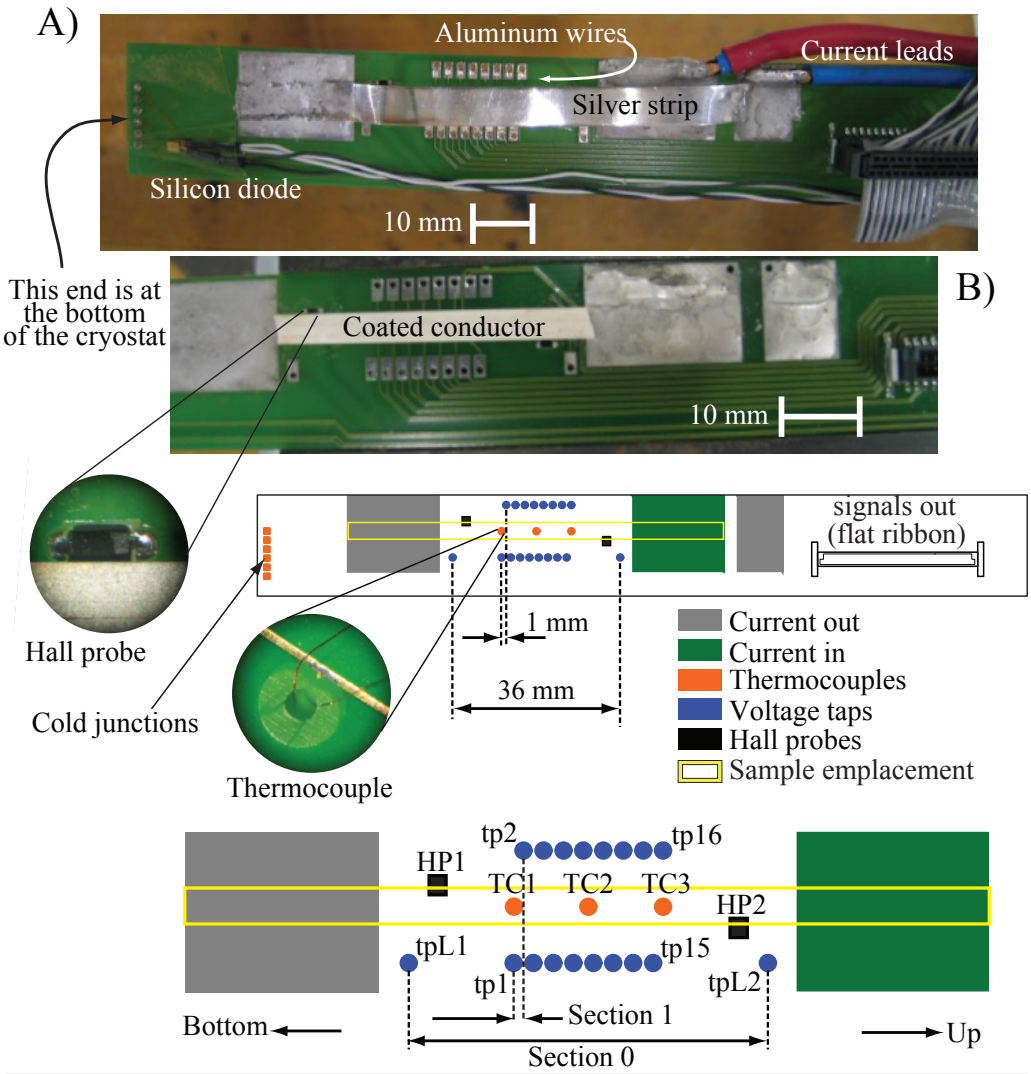

Figure 2.2: Details of the sample holder. A) The sample ready for measurements. B) The sample mounted on the PCB without the current leads, silver strip and aluminum taps. The Hall probes located at the edges of the samples monitor the perpendicular component of the magnetic field (the component normal to the surface of the probes).

2.1.1 Tape Resistance as a Function of the Temperature

Since the measurements made in this work are basically voltage recordings, the temperature of the samples during the current pulses is estimated with the temperature variation of the tape resistance. This variation is obtained by monitoring the section voltages and the thermocouple temperatures while the sample warms-up during the liquid-nitrogen evaporation ($\approx$ 12 hours). Due to the sample vertical arrangement, a temperature gradient appears during the evaporation of the liquid nitrogen (during the evaporation parts of the sample are immersed in the liquid and others are not). In order to estimate this gradient and get the temperature profile along the length of the sample during its warm-up, three copper-constantan thermocouples (diameter 0.025 mm), are disposed along the length of the superconductor. The correction, inherent to the sample vertical arrangement, is made by a linear interpolation between those three temperature measurements. Note that the temperature of

the thermocouple cold junctions, located at the bottom of the sample holder, is monitored with a Lakeshore DT-470 silicon diode.

Figure 2.3 presents the normalized tape resistance for selected sections. Note that the same measurements were reproduced under different external fields and pulse amplitudes (0, 100, 200 mT and 1, 2, 5 A) for two different samples without observing significant modifications of the curve shape. In figure 2.3, the inset shows the resistivity of the tape compared to referenced values for high purity silver, hastelloy and normal YBCO. Since the normal resistance of the superconductor as well as the resistance of hastelloy are very high, one may estimate the tape resistance as being the resistance of the stabilizer (silver). From the figure inset, the resistance of high purity silver is slightly smaller than the measured resistance. This is expected from metals containing impurities [13].

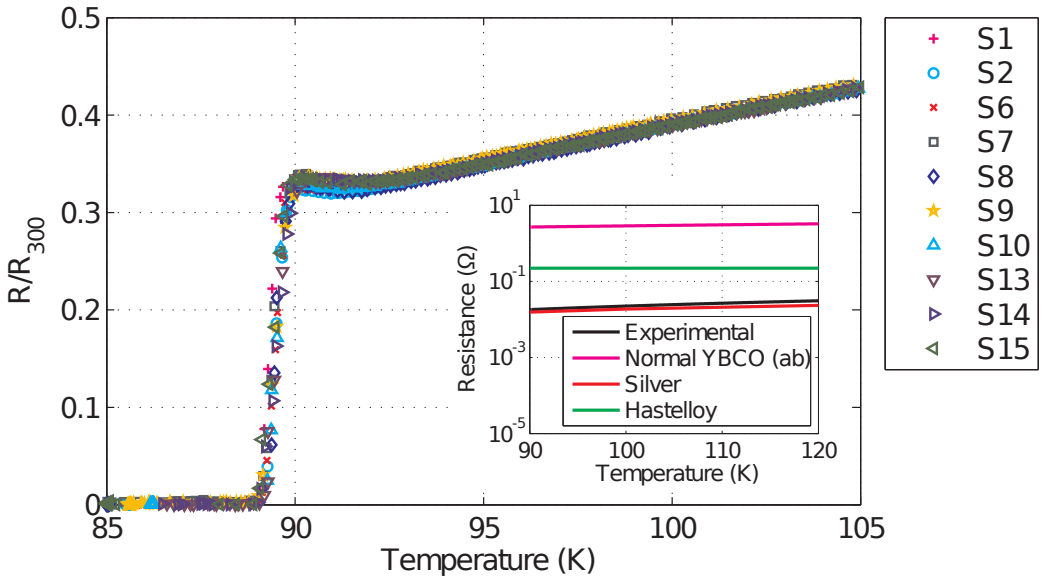

Figure 2.3: R-T curves for selected sections. The stabilizer is $\approx 2\mu$m thick and 4 mm width. The room-temperature resistance (R_{300}) is 0.0569 Ω for a tap spacing of 36 mm. The inset compares the tape resistance with that of one individual materials composing it for the same distance *i.e.* 36 mm.

2.2 Samples Characterization Under Uniform External Magnetic Fields

In this section, coated conductors are submitted to uniform external magnetic fields in order to get the field dependence of the power-law parameters *i.e.* $J_c(B)$ and $n(B)$. Nevertheless, it is difficult to isolate the sole effect of the magnetic field on the resistive transition since heat is also generated during the process. As a matter of fact, for transport current above the critical current, Joule losses become important and heat-up the conductor. That means that the resistivity of the superconductor generates heat that in turns increases the resistivity. This "avalanche effect" may provokes the normal transition and leads to irreversible damage in the conductor if the transport current and field are not reduced to acceptable values. This effect is illustrated in figure 2.4 which depicts the voltage evolution as the temperature of the sample increases due to Joule losses. Those measurements are presented for a constant current (left) and for a constant external magnetic flux (right).

For each part of the figure, the increase in voltage follows two rates. A fast increasing rate (from $V^*(0)$ to ≈20 V/m) characterizing the flux-flow regime (current in the superconductor) and a linear rate occurring once the current has switched into the stabilizer. The linear rate comes from the time derivative of the temperature that is proportional to Joule losses. Note that the slopes in the linear regime show a quadratic dependence with the transport current (Joule losses $\propto I^2$). On the same figure, one may observe (on the left part) that the transition is more abrupt as the external field is reduced. For instance, the voltage slopes in the flux flow regimes (between 10 and 16 V/m) are respectively 3.4, 3.8 and 4.2 V/m.s for the black, green and red curves .

An other interesting feature of the transition is the kink observed in both part of the figure. The kink illustrates the current diversion from the normal-superconductor to the stabilizer. A closer look at the right part of the figure shows that the height of the kinks grows with transport current. This comes from Ohm's law, *i.e.* for a given resistance the voltage is proportional to the current. The dashed-lines represent the expected voltage at 92 K obtained from the temperature-dependent tape resistivity curve presented in figure 2.3. The fact that the transition occurs far below those lines means that the transition occurs at lower temperature than the critical temperature (T_c). This phenomenon is

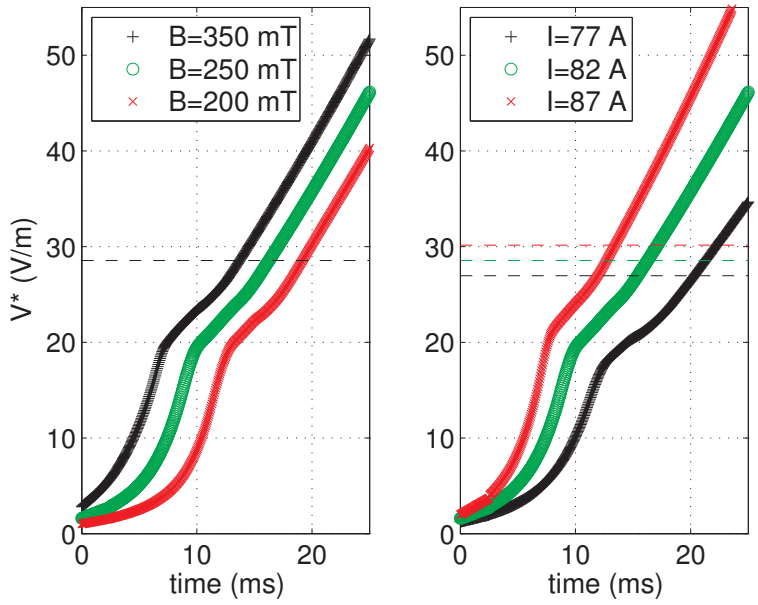

Figure 2.4: Typical voltages traces obtained under external magnetic fields of respectively 200, 250 and 350 mT for a current of 82 A (left) and with an external magnetic field of 250 mT for currents of respectively 77, 82 and 87 A (right). Also presented on the figure is the expected resistance of the section at T=92 K (dashed-lines) obtained from figure 2.3. V^* is the measured voltage divided by the section length.

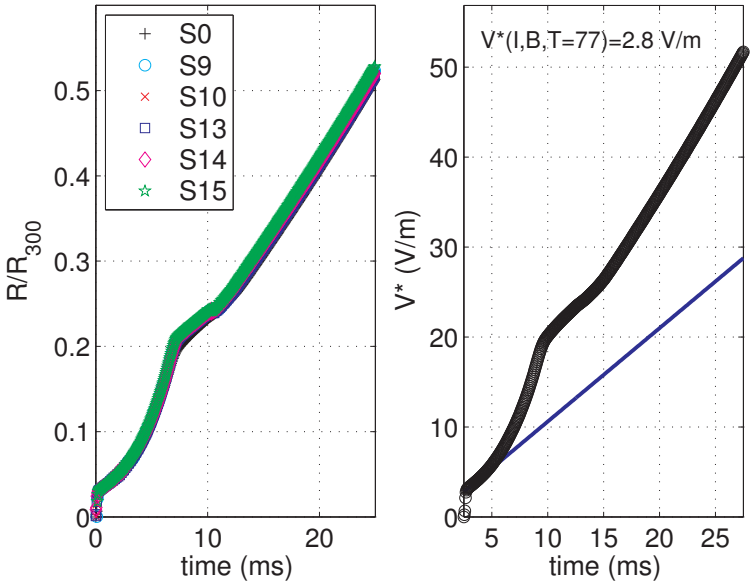

Figure 2.5: Typical resistances and voltages traces obtained for a transport current of 82 A with a uniform external magnetic flux of 350 mT. On the left, all the section resistance rise at the same time implying that the sample temperature is uniform over the whole tape. The right figure shows the way the isothermal voltage is obtained for the V^*-I curve (figure 2.6). The linear variation of voltage at the beginning of the pulse (blue curve) is used to find the y-intercept of the linear curve (displayed at the top of the figure). The value obtained is used to build the curves presented in figure 2.6.

expected from the critical surface. In other words, the critical temperature reduces when the current density and/or the external field increase.

The tape characteristics vary from sample to sample. However, figure 2.5, shows that the tested tapes are uniform along their length (here for 4 cm). As a matter of fact , for a given experiment, all the section shows the same resistance evolution. This observation allows to consider a uniform temperature along the length of the conductor while the tape is submitted to the uniform magnetic field. A similar assumption could be made on the current distribution in the cross-section of the layers, since the pulse duration and amplitude are high enough to allow a fast diffusion of current in respect to the pulse duration. This assumption is crucial for the numerical model developed in this thesis, for instance see section 3.2.2.

As previously said, decoupling the temperature effect from the voltage measurements is not an obvious task. Accordingly, a trick is employed to estimate the flux-flow voltage as a function of the current and the external magnetic field at the temperature of liquid nitrogen. The isothermal voltage of the superconductor is obtained using the slope of the pulsed response at the beginning of the experiment.The right part of figure 2.5 shows the method.

Figure 2.6 presents the V-I curves obtained from current pulses of 25 ms (such as the one presented in the right part of figure 2.5) obtained at various external fields. Note that the values at low external fields are more difficult to obtain at smaller pulse length since the pulse amplitude is limited by the current source. For pulses of 25 ms under zero external magnetic field, the normal state was never reached even for a current pulse of 160 A that burned the sample. From figure 2.4 and 2.6, one can note that increasing external fields reduce the critical current and the voltage slopes in the flux-flow regime. These effects allow a smoother transition that helps to reduce the violent release of energy observed for the transition under zero field.

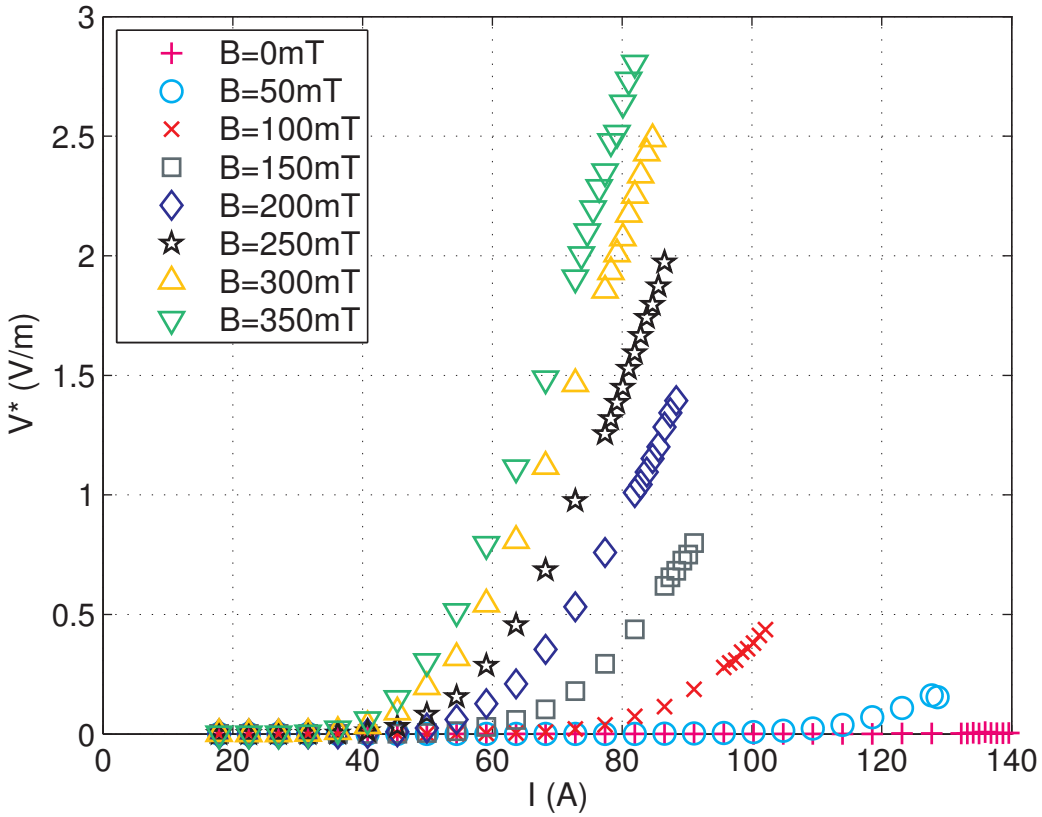

Figure 2.6: Flux-flow voltages as a function of transport current for different external magnetic fields. A reduction of the critical current (value at which the voltage becomes non-negligible) is observed with the increase of the external magnetic flux. The measurements at lower field values are difficult since the time-resolved voltage traces are abrupt (steeper transition). Note that the sample dimensions are the following: tape width=4 mm, hastelloy substrate=50 μm, buffer stack=70 nm, YBCO layer=1 μm and silver stabilizer=2 μm.

2.3 Normal Zone Propagation Velocity Initiated by a Localized Magnetic Field

The ability of superconductors to quench rapidly is defined by the normal zone propagation velocity (NZPV). The normal zone propagation is closely related to the propagation of heat along the materials. As we are going to see in the next chapter, the NZPVs are expected to be very small for coated conductor operating at elevated temperature (around 77 K) [48, 49, 50].

Accordingly, the NZPV is measured here along small samples (4 cm) delimited by voltage taps located 2.5 mm apart. The propagation is initiated using an artificial defect created by a localized magnetic field. Figure 2.7 depicts the sample arrangement.

For the measurements, samples are submitted to current-driven pulses of different amplitudes and durations *i.e.* 70-160 A and 10-500 ms respectively. Quench nucleation is obtained using a small permenorm® electromagnet used to create non-destructive, variable-size field-induced defects in one of the 15 wire-delimited sections of the tape. In order to reach a reasonable magnetic field, the magnet coil is made of 610 turns of 0.2 mm diameter-size copper wires. The localized DC magnetic flux generated by the coil is measured with a small, movable cryogenic Hall probe (0.127×0.127 mm^2 active area) controlled by a steeper motor placed at the exterior of the cryostat (figure 2.8). The magnetic flux obtained from the coil has shown to be as large as 300 mT for a coil current (I_m) of 2 A– see figure 2.8. Considering the field dependence of the critical current (see figure 2.6), the reduction of the critical current is estimated to be as large as 70% for the section located in the magnet air-gap.

To summarize, the measurements methodology is as follows: defects in tapes are produced using a localized DC magnetic field. During the transport-current pulses, quenches are initiated in the magnet air-gap where the external magnetic flux is maximum. Due to current redistribution and heat generation, the normal zone start to propagates in the sections adjacent to the coil air-gap building up an electric potential difference between the end-taps of the corresponding sections. This voltage, directly associated to the normal state arising in the material, gives an estimate of the transition dynamics occurring during the current pulses.

Figure 2.9 illustrates typical time-resolved voltage traces obtained during the experiments. The black-dashed line represents the quench criterion used into this section to defined relevant times. Those are Δt_{ini}, t_1 and t_2 which are obtained for values of the voltage at which the corresponding tape resistance ratio $R/R(300)$ reach 0.1. Δt_{ini} represents the initial delay before the quench apparition, t_1 is the first reference time to determine the NZPV, corresponding to the resistance apparition in section 10, and t_2 is the second reference time corresponding to the resistance apparition in section 9. The NZPV is thus obtained with the following formula:

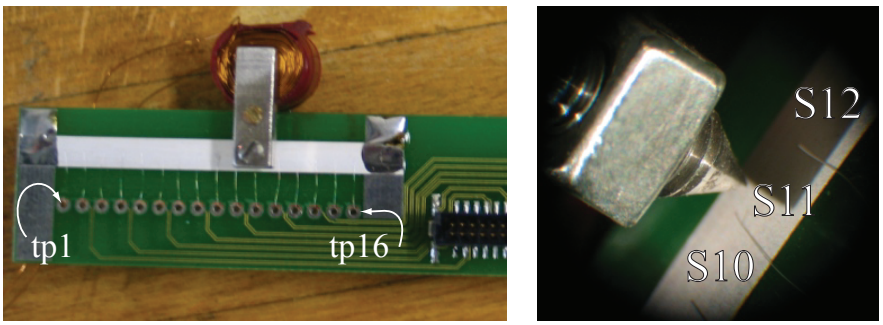

Figure 2.7: Voltage taps (16 overall) are $\approx 2.5 \pm 0.2$ mm apart and made of 26 μm aluminum wire to reduce probe artifacts on the measurements. The permenorm® coil is made of 610 turns of 0.2 mm diameter-size copper wire. On the right picture, S10, S11 and S12 represent wire-delimited sections (respectively section 11, 10 and 12) for which the voltage is monitored.

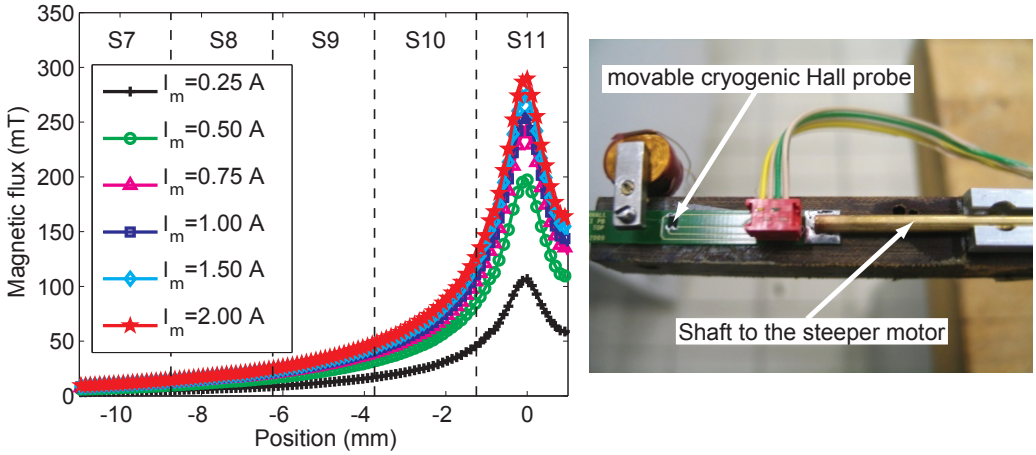

Figure 2.8: Hall probe mapping of the magnetic flux generated by the coil carrying 0.25 to 2.00 A in liquid nitrogen along the length of the samples for an air-gap of 1 mm. Note that the field saturates with the coil-current (I_m). This seems to come from the pole-tips of the magnet which locally reach the saturation field of permenorm® (≈1.5 T). The dashed-lines drawn on the figure delimits the sections which are, from right to left, S11, S10, S9, S8 and S7.

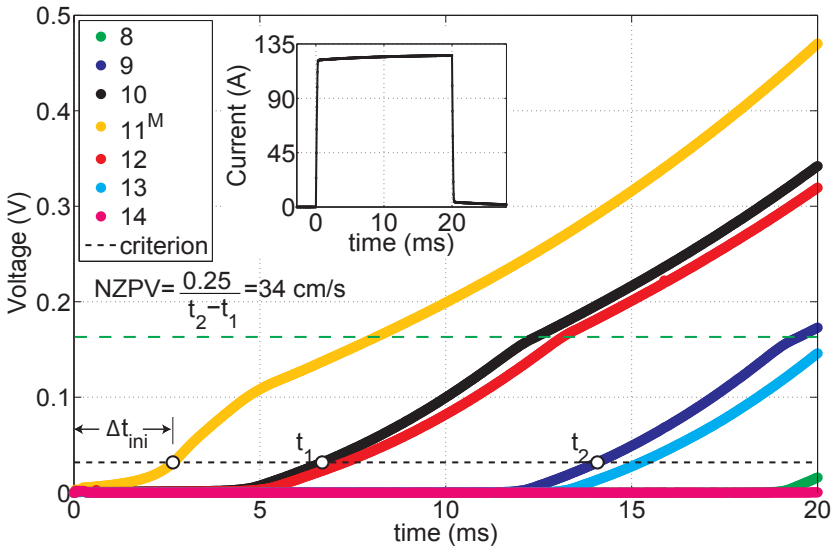

Figure 2.9: Typical time-resolved voltage measurements for a current pulse of 128 A and 20 ms of duration (see the waveform in the inset). Each curve represents the resistance increase coming from the electrical field generated in the sections. Section 11 (labeled with a "M") is the section in which the coil is located. The NZPV is obtained using equation 2.3.1. The DC current in the coil (I_m) is 2 A and the air-gap 1 mm. The black-dashed line represents the quench criterion that corresponds to R =0.1R(300). The green-dashed-line shows the estimated voltage at T =92 K obtained from the temperature-dependent tape resistivity curve (figure 2.3).

$$\text{NZPV} = \frac{0.25\ \text{cm}}{t_2 - t_1} \tag{2.3.1}$$

Sections 9 and 10 are used to determine the NZPV in order to reduced the error due to field overflowing from section 11 – see figure 2.8. This field overflow induces a larger flux-flow resistance nearby the defect that increases significantly the NZPV. Note that the small lag observed between the transition of sections 10/12 and 9/13 might be caused by uncertainty on the taps spacing as well as on the tape orientation in the coolant (the tape is placed vertically along the length of the cryostat). Since the NZPVs are low, current pulses have to be terminated before the whole spreading of the normal

zone through the entire length of the tape. This, in order to avoid thermal runaway (I_c degradation is observed over 600 K [51]) and destructive hot-spots. Accordingly, in the present setup, 5 sections (12.5 mm) are sufficient to estimate the NZPVs.

2.3.1 Effect of the Defect Strength

The first thing to note from figure 2.9 is that, as expected, the first section presenting a growing voltage is the section in which the magnet is located (section 11, yellow curve), followed by the adjacent sections, *i.e.* 10/12, 9/13 etc. One may also notice that all the curves presented in the figure exhibit a kink. The kink is observed once the section under study becomes fully normal. Since the magnetic field generated by the coil (I_c reduction) is more intense in section 11 – see figure 2.8, the kink is observed at a smaller voltage (temperature) in this section than in the others (also observed previously in figure 2.4). The fact that adjacent sections begin to show potential difference once the former sections are fully normal *i.e.* just after the kink appears and without overlap, means that the normal zone front is very steep. This is further supported by the low NZPV values observed in coated conductors.

Figure 2.10 shows NZPV obtained by varying current pulses amplitude and duration for different DC coil-currents. According to this figure, one can notice that the velocities have about twice the magnitude than that usually found in the literature for similar tape – see for example [52, 49, 50]. This is explained by the absence of the copper clad usually present on commercial tape, as well as to the magnetic field overflowing from section 11 that are supposed to respectively increases the heat generation during the current pulse and increases the flux-flow resistance along the tape length. In addition, note that the measurements have been carried out at transport current above I_{c0} (90 A), which also means larger heat generation in the stabilizer. Besides this fact, figure 2.10 shows that over ≈1.2 I_{c0} (109 A) the effect of the coil current (localized magnetic field) is more important than at lower current pulses, where the NZPVs seems independent of the defect strength (I_m). This feature

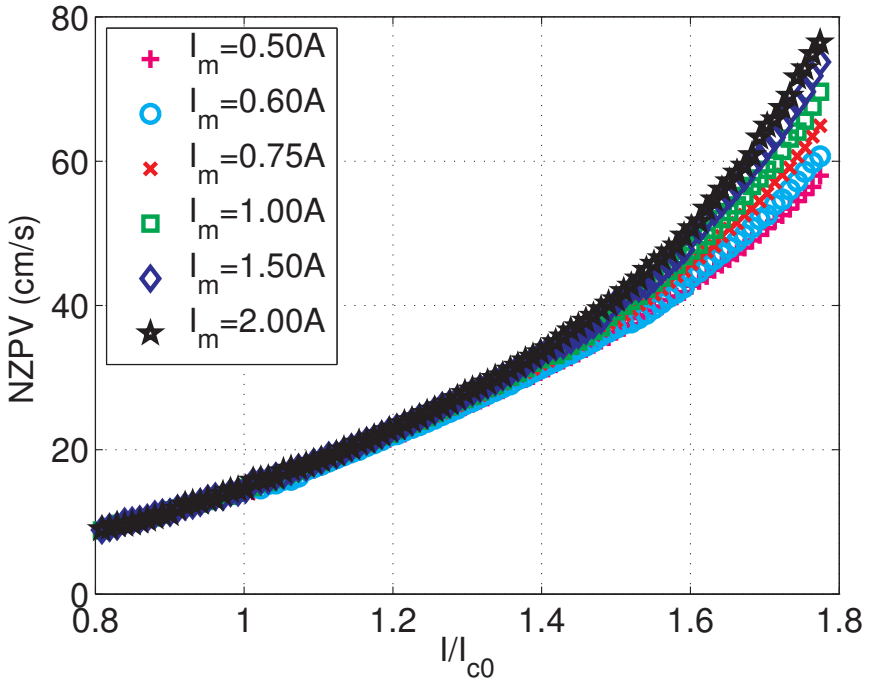

Figure 2.10: NZPV as a function of normalized current (I/I_{c0}). I_m is the DC current passing through the magnet. The magnet air-gap is 1 mm. Note that the critical current at the temperature of liquid nitrogen and without external magnetic field is I_{c0} ≈90 A. At $I = I_{c0}$, the NZPV is approximately 14 ± 1 cm/s for any field-induced defect.

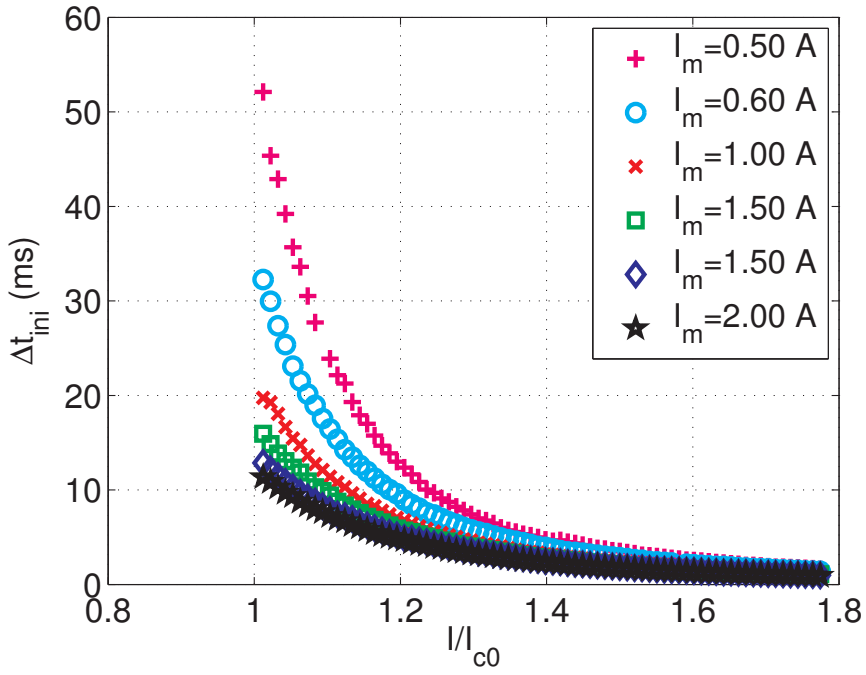

Figure 2.11: Initial time before quenching (Δt_{ini}) for a magnet air-gap of 1 mm. Long initial times make the propagation hard to achieve and lead to thermal runaways. I_{c0} is the critical current at $T = 77$ K and B=0 T.

may come from the reduction of the ratio $I/I_c(B)$. As a matter of fact, an increase of the localized magnetic field allows more current to be diverted into the shunt, which contributes to additional heat and thus increases the velocities. Since losses are proportional to RI^2 (R is the tape resistance), the effect of the magnetic flux becomes less apparent at lower pulse amplitudes. Note that the effect of the coil current above 1.2 I_{c0} may be also due to the way the NZPV is measured since this quantity shows more important variations for shorter elapsed times ($\Delta t = t_2 - t_1$).

Another important feature observed from voltage traces is the time needed for the normal zone to appears in the samples. Following figure 2.11, it can be shown that, at currents below $1.4I_{c0}$ (126 A), smaller defects take more time to make section 11 transiting (large Δt_{ini}). This is also explained by the ratio $I/I_c(B)$ that creates an higher initial resistance near the defect when the coil-current is increased. Since all the experiments leads to quench, larger delays have shown to produce more violent release of energy once the propagation initiates and consequently burned the samples. This observation is related to a feature previously observed in figure 2.4. From that figure, it as been shown that the curvature of the V-t curve is more pronounced at lower field values. However, one can notice that the delay becomes independent of the defect strength (coil-current) as the transport current increases. In fact, larger current implies more heat generation in the stabilizer. When the current is sufficient, heat generated in that layer allows uniform quenches since heat diffuses more rapidly in the stabilizer than in the substrate and superconductor. Therefore, one can separate two different behaviors of coated conductors during quenches. The first one, at lower current ($I < 1.4I_{c0}$) where the propagation initiates at the non-homogeneities and occurs mostly in the superconductor (longitudinally). The other, at higher current ($I > 1.4I_{c0}$) where the heating of the stabilizer lowers the effect of the superconductor uniformity on the quench initiation and allows a more uniform longitudinal propagation (the uniform heating of the stabilizer rise the flux-flow resistance everywhere in the superconductor while its quenching).

2.3.2 Subcooled Experiments

Thermal effects on the NZPV are observed in subcooled nitrogen at ambient pressure (section 3.1.2). Figure 2.12 shows velocities obtained for different ratio of $I/I_c(T)$. Where $I_c(T)$ is obtained from a linear extrapolation (I_c reduces with T [48])

$$I_c(T) = I_c(T_0)\frac{Tc - T}{T_c - T_0}\,, \tag{2.3.2}$$

with, T_0=77 K, T_c=90 and $I_c(T_0)$=90 A. The measurements are done by reducing the pressure into the cryostat which, in turn, induced the temperature reduction – see figure A-1 in Appendix A. Once the minimum temperature is reached (≈70 K), the ambient pressure is re-established inside the cryostat. The response to current pulses of 137 A with a coil current of 2 A is monitored at every 10 seconds during the bath warm-up *i.e.* during the recovery of the saturated phase (≈10 minutes).

Considering the temperature dependence of the critical current, the NZPVs are larger in subcooled nitrogen in comparison to experiments made in the saturated liquid, *i.e.* at 77 K. It is not clear if this fact comes from the improvement of the thermal diffusivity, an ill defined critical current (equation 2.3.2) or from the heat transfer mechanism [53, 54] –see section 3.1.2 for more details.

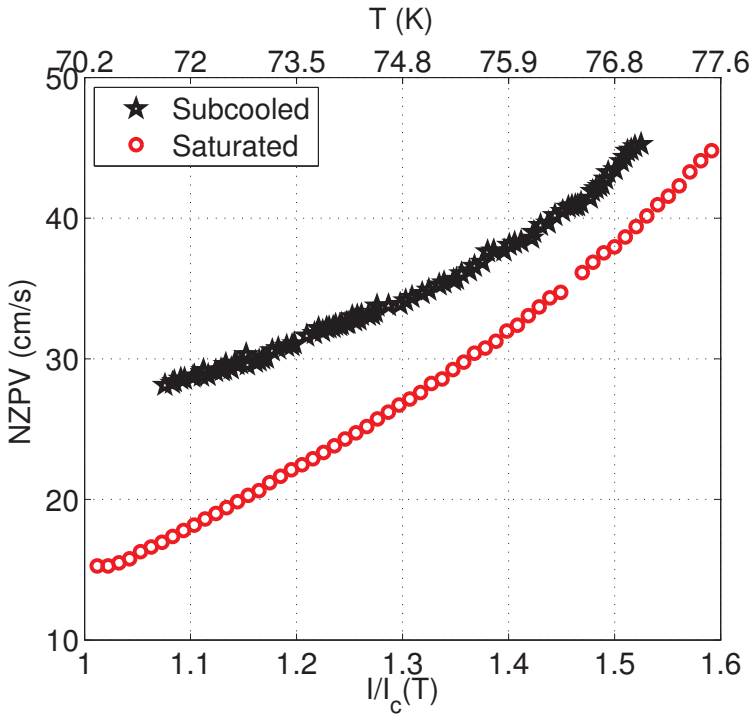

Figure 2.12: NZPVs for a subcooled tape. The black pentagon display the NZPV obtained during the warm-up of the subcooled nitrogen with current pulses of 137 A with a coil current of 2 A. The bottom axis displays the ratio $I/I_c(T)$ =137 A$/I_c(T)$ estimated from equation 2.3.2. For sake of comparison, the red circle show the NZPV obtained for different current in saturated nitrogen *i.e.* at 77 K for I_m=2 A.

Chapter 3

Modeling of Coated Conductors as Resistive-SFCL Elements

DURING this thesis work, a numerical model has been developed in order to investigate the design effects of coated conductors that may enhance the normal zone propagation in these conductors. This chapter is divided in three sections. In the first section, are presented the physical concepts needed to present and justify the assumptions used to build the model. This first section gives also a definition of the thermal stability and of the Normal Zone Propagation Velocity (NZPV). The second section presents the numerical model and its validation. Finally, the last section shows the effect of the design parameters on the NZPV as well as on the thermal stability of coated conductors submitted to transport current above the critical value.

3.1 Physical Concepts

3.1.1 The Diffusion Equation

Many approaches are presently used to model superconductors at a macroscopic scale *e.g.* statistical [55, 56] , numerical [57, 58] and analytical [59, 60]. In this work, a numerical approach based on the thermal and electrical diffusion equation is used.

As observed in the experimental section, whatever are the values of H and J, a superconductor is in the normal state if its temperature is above T_c. Accordingly, knowing dynamically the temperature distribution along the tapes would indicate the state of the superconductor during quenches. This temperature distribution is obtained by solving the heat equation.

$$\rho_m C_p(T)\frac{\partial T}{\partial t} = \nabla\Big(k(T)\nabla T\Big) + Q(T), \quad T = T(\mathbf{x},t),\ \mathbf{x} = (x,y,z) \tag{3.1.1}$$

Where, ρ_m, $C_p(T)$ and $k(T)$ are respectively, the mass density (kg/m^3), specific heat (J/kg.K) and thermal conductivity (W/m.K) of the material. $Q(T)$ is the heat generated in the conductor in W/m^3. Equation 3.1.1 is a parabolic partial differential equation (PDE) *i.e.* a form of PDE encountered in a broad range of applications involving diffusion. To be more specific, equation 3.1.1 allows to represent the heat diffusion as well as the movement of electrical charges in a medium. Since the model presented in this thesis is built in reference to that equation, it is relevant to present some important diffusion lengths that are related to it. Those are the thermal and magnetic diffusion length as well as the Current Transfer Length (CTL). The diffusion lengths are used to justify the numerical formulation used in this work. The CTL to illustrate the origin of the NZPV improvement in coated conductors having a thin interface resistance inserted between the superconductor and the stabilizer.

The Thermal Diffusion Length

Considering the homogeneous form of equation 3.1.1, one can obtain its solution for an initial impulse of temperature at $\boldsymbol{\xi} = (x_0, y_0, z_0)$ – for details, see Appendix B:

$$G(\mathbf{x}, \boldsymbol{\xi}, t) = \frac{\exp\left(-\frac{|\mathbf{x}-\boldsymbol{\xi}|^2}{4D_{th}t}\right)}{\left(4\pi D_{th}t\right)^{3/2}}, \qquad \mathbf{x} = (x, y, z), \quad \boldsymbol{\xi} = (x_0, y_0, z_0) \tag{3.1.2}$$

Where, D_{th} is the thermal diffusivity constant defined as:

$$D_{th} = \frac{k}{\rho_m C_p} \tag{3.1.3}$$

Equation 3.1.2 gives the evolution of the temperature from a single point in space along time. Even if such initial distribution is not "physically" possible (infinite temperature gradient at $\mathbf{x} = \boldsymbol{\xi}$), the evolution of this theoretical temperature allows to define the thermal diffusion length (λ_{th}). This parameter is the distance, at a given time, for which the temperature from the initial point $\boldsymbol{\xi} = (x_0, y_0, z_0)$ drops of 63 % *i.e.* $T(\mathbf{x},t) = T(\boldsymbol{\xi}, t)\exp(-1)$.

$$|\mathbf{x} - \boldsymbol{\xi}| = \lambda_{th} = 2(D_{th}t)^{1/2} \tag{3.1.4}$$

To appreciate the effect of the thermal diffusivity on the thermal diffusion length, one may look at figure 3.1 which shows a comparison of λ_{th} for materials encountered in this thesis work. Table 3.1 lists the scale of different thermal parameters of those materials at the temperature of boiling liquid nitrogen – see Appendix A for additional material properties over a larger temperature range.

Table 3.1: Order of magnitude of relevant materials properties at liquid nitrogen temperature.

Material	ρ_m [kg/m^3]	C_p [J/(kgK)]	k [W/(Km)]	D_{th} [μm^2/s]
Silver	10 500	164	400	232
YBCO$_{ab}$	6 410	156	9	9
YBCO$_c$	6410	156	3	3
MgO	3580	93	504	1514
Sapphire	3 970	62	1 131	4595
Hastelloy C-276	8 890	172	7	5
Nitrogen	809	2000	0.1338	0.08

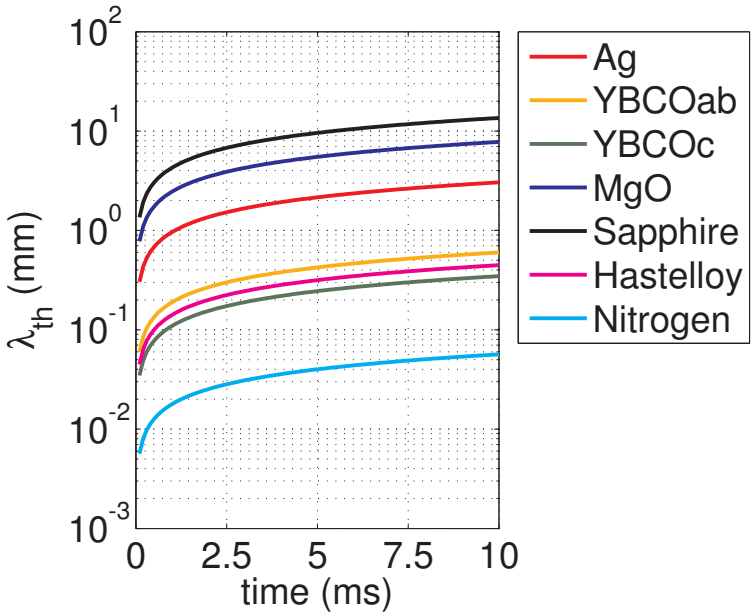

Figure 3.1: Thermal diffusion length as a function of time for different materials encountered in this work. Sapphire has superior thermal diffusivity than other materials and obviously has a larger thermal diffusion length (λ_{th}).

The Magnetic Diffusion Length

Using the quasi-static Maxwell's equations [61] and usual constitutive relations in free-space *i.e.*

$$\begin{aligned} \nabla \times \mathbf{E} + \frac{\partial \mathbf{B}}{\partial t} &= 0 \\ \nabla \times \mathbf{B} &= \mu_0 \mathbf{J} \\ \mathbf{E} &= \rho \mathbf{J} \\ \nabla \cdot \mathbf{J} &= 0 \,, \end{aligned} \tag{3.1.5}$$

one can rearrange them to get the diffusion equation:

$$\begin{aligned} \nabla \times \Big(\nabla \times \mathbf{E} + \frac{\partial \mathbf{B}}{\partial t} \Big) &= 0 \\ \nabla \times \Big(\nabla \times \rho \mathbf{J} \Big) + \frac{\partial}{\partial t} \Big(\nabla \times \mathbf{B} \Big) &= 0 \\ \rho \Big(\nabla (\nabla \cdot \mathbf{J}) - \nabla^2 \mathbf{J} \Big) + \mu_0 \frac{\partial \mathbf{J}}{\partial t} &= 0 \,. \end{aligned} \tag{3.1.6}$$

Thus,

$$\frac{\partial \mathbf{J}}{\partial t} = D_m \nabla^2 \mathbf{J} \,. \tag{3.1.7}$$

where the diffusion constant is,

$$D_m = \rho / \mu_0 \,. \tag{3.1.8}$$

By analogy to equation 3.1.4, one can also obtain the "magnetic" diffusion length,

$$\lambda_m = 2 (D_m t)^{1/2} \tag{3.1.9}$$

Figure 3.2 displays the effect of the transport current on the normalized current diffusion *i.e.* the ratio of diffusion lengths in different medium over the thermal diffusion in the substrate. The ratio

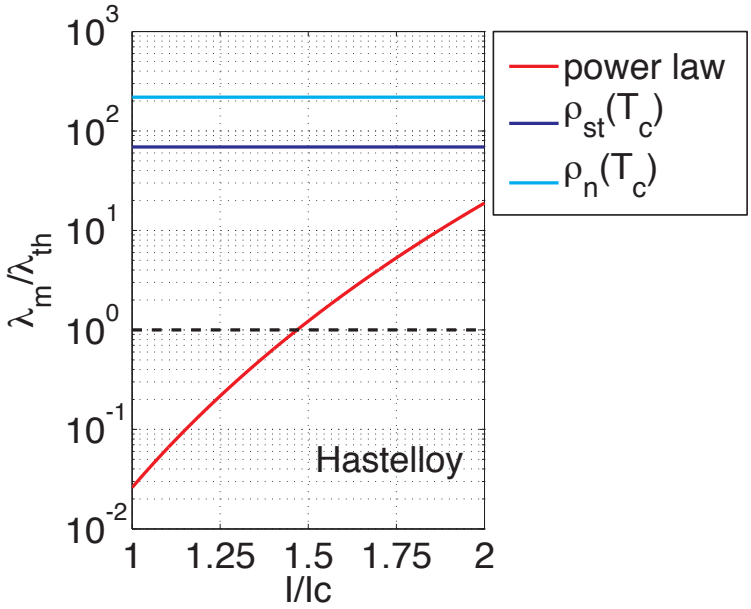

Figure 3.2: The ratio of diffusive length λ_m/λ_{th} as a function of the reduced current I/I_c (I_c =90 A) for the power law ($n = 20$) presented in figure 1.4. The dashed line delimits the conditions for which heat propagates faster than the current (above 1.5 I/I_c). This figure shows that the current may diffuse slowly than heat in the superconductor when it is in the flux-flow regime. The ratio is also presented for the normal and stabilizer resistivity at $T = T_c$.

is displayed for the superconductor in the flux-flow regime (red) and in the normal state (light blue) as well as for the stabilizer (dark blue) for different values of the reduced current I/I_c. Hastelloy is used to define the thermal diffusion length since it represents more than 90% of the coated conductor composition. A power-law independent of the temperature and magnetic field is used to compare the ratio of diffusion lengths for the superconductor in the flux-flow regime and in the normal state. The ratio is also displayed for the current diffusion in the stabilizer at $T = T_c$. From the figure, one can see that the current may diffuse slower than heat for the superconductor in the flux-flow regime (when the reduced current is below 1.5 I_c). Note that, the reduction of the critical current expected from the temperature rise and from the non-zero field value increase the reduced current. The condition of faster current diffusion has important effect on the assumptions used for the numerical model (section 3.2.2).

The Current Transfer Length (CTL)

The Current Transfer Length CTL is defined as the length scale of current transfer between two conductors (when the current is initially imposed only at one conductor) separated by a thin contact resistance [62, 63]. This quantity represents the distance over which the tape cross-section becomes equipotential *i.e.* when the transfer of current becomes negligible between the conductors.

In order to define the CTL, one may look at the differential current ∂I crossing a resistive interface of resistivity ρ_{in} and thickness d_{in} from a point 1 to a point 2 delimiting a differential length of conductor ∂x. Considering the bi-layered conductor of infinite length (x direction) presented on figure 3.3, the following development is made.
From Ohm's law,

$$\begin{aligned} -(V_2 - V_1) &= \partial R_{\text{in}} \partial I \\ &= \frac{\rho_{\text{in}} d_{\text{in}}}{w \partial x} \partial I \\ &= \frac{R^*}{w} \frac{\partial I}{\partial x}, \quad R^* = \rho_{\text{in}} d_{\text{in}} \, . \end{aligned} \tag{3.1.10}$$

Rewriting equation 3.1.11 in terms of the electrical field ($E = -\partial V / \partial x$) gives,

$$\begin{aligned} \left(E_2 - E_1\right) &= \frac{R^*}{w} \frac{\partial}{\partial x} \left(\frac{\partial I}{\partial x} \right) \\ \left(\rho_2 J_2 - \rho_1 J_1\right) &= \frac{R^*}{w} \frac{\partial^2 I}{\partial x^2} \\ \left(\frac{\rho_2}{d_2 w} I_2 - \frac{\rho_1}{d_1 w} I_1 \right) &= \frac{R^*}{w} \frac{\partial^2 I}{\partial x^2} \, . \end{aligned} \tag{3.1.11}$$

Where ρ_1 and ρ_2 are the resistivity of each layers and d_1 and d_2 their thickness. The last equation can be rewritten using the definition $I_0 = I_1 + I_2$ which gives

$$\left(\frac{\rho_2}{d_2} I_2 - \frac{\rho_1}{d_1} (I_0 - I_2) \right) \frac{1}{R^*} = \frac{\partial^2 I}{\partial x^2} \, . \tag{3.1.12}$$

From the conservation of charge at the interface of the conductors,

$$\frac{\partial I}{\partial x} \cdot \partial y = \frac{\partial I_1}{\partial x} \cdot \partial y = \frac{\partial I_2}{\partial x} \cdot \partial y \, , \tag{3.1.13}$$

which implies that,

$$\left(I_2 \left(\frac{\rho_1}{d_1} + \frac{\rho_2}{d_2} \right) - \frac{\rho_1}{d_1} I_0 \right) \frac{1}{R^*} = \frac{\partial^2 I_2}{\partial x^2} \, . \tag{3.1.14}$$

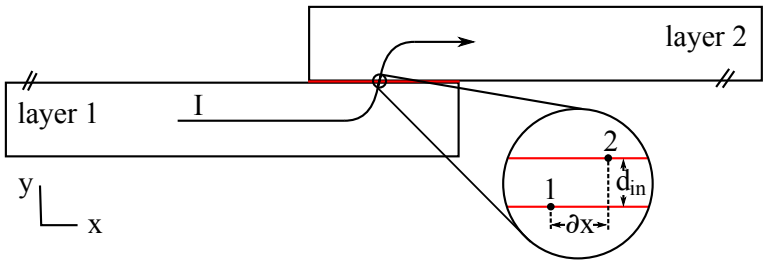

Figure 3.3: A bi-layered conductor with a contact resistance. The x and y axis respectively represents the length and thickness of the conductor. On the figure is displayed the current path and direction (I), the interface thickness (d_{in}) and the differential length of conductor (∂x).

Solving the homogeneous part of equation 3.1.14 gives the following characteristic equations – see Appendix C and D for similar calculations,

$$\Gamma = \pm\sqrt{\gamma}, \qquad \gamma = \frac{\rho_1}{d_1 R^*} + \frac{\rho_2}{d_2 R^*} \tag{3.1.15}$$

This yields to the homogeneous solution

$$I_2(x) = C_1 \exp(-\sqrt{\gamma}x) + C_2 \exp(\sqrt{\gamma}x)\ . \tag{3.1.16}$$

Seeking a constant for the particular solution and inserting it in equation 3.1.14 gives,

$$C_3 = \frac{\beta I_0}{\gamma}, \qquad \beta = \frac{\rho_1}{d_1 R^*}\ . \tag{3.1.17}$$

Using the boundary conditions,

$$I_2(0) = 0, \qquad \text{no current in layer 2} \tag{3.1.18}$$
$$I_2(\infty) = \frac{\beta I_0}{\gamma}, \qquad \text{i.e. } V_1 = V_2\text{, parallel resistance}$$

and superposing the solutions yields to:

$$I_2(x) = \frac{\beta I_0}{\gamma}\Big(1 - \exp\left(-\sqrt{\gamma}x\right)\Big)\ . \tag{3.1.19}$$

It is customary to define the CTL as the distance for which the current in layer 2 is at a factor $\big(1 - \exp(-1)\big)$ of its maximum value. Thus,

$$\lambda_{CTL} = \left(\frac{R^*}{\rho_1/d_1 + \rho_2/d_2}\right)^{1/2} \tag{3.1.20}$$

From a similar calculation, one can get the screening length in each of layer of the conductor using a 2D approach [64]. Considering that layers 1 and 2 are respectively the superconductor and the stabilizer. One can obtain,

$$\Lambda_{CTL} = \left(\frac{R^* J_c^*}{E_0}\right)^{1/2}, \qquad \text{in the superconductor,} \tag{3.1.21}$$

$$\lambda_{CTL} = \left(\frac{R^* d_{\text{st}}}{\rho_{\text{st}}}\right)^{1/2}, \qquad \text{in the stabilizer.} \tag{3.1.22}$$

where J_c^* is the critical current density per unit of length ($J_c^* = J_c/d_{\text{HTS}}$) and E_0 the critical field.

Note that equations 3.1.21 and 3.1.22 are valid as far as the thickness of the stabilizer is much smaller than the thickness of the interface resistance *i.e.* $\rho_{\text{st}} d_{\text{st}} \ll R^*$. In addition, these equations are valid if the variation of the potential in the stabilizer is small along its thickness and if the potential is constant along the thickness of the superconductor. In this work, it is assumed that these conditions are always satisfied.

3.1.2 Pool Boiling

In order to present the thermal stability in superconductors, one must consider the heat balance of the system composed of an heated surface and its surrounding. The following paragraphs introduce the basic mechanism of heat transfer occurring between the heated surface and liquid nitrogen under different time scale and liquid phases *i.e.* saturated and subcooled liquids.

Immersing tapes in liquid nitrogen allows to remove heat generated in the conductive layers. For quiescent liquid at atmospheric pressure, the heat transfer occurring at the interface is termed pool boiling [65, 66]. Pool boiling is basically a convective processes (mixing induced by bubbles) associated with a phase change of the fluid at the heated surface in contact with it. This heat transfer mechanism which involves fluid mechanics as well as thermodynamics is very complex and depends on many factors *e.g.* surface temperature, surface orientation, surface roughness, gravity, surface tension, nature of the coolant *etc*. Because it is difficult to develop the governing equations for pool boiling, it is customary to define a convective heat transfer coefficient h_c which simulates, through the Newton's law of cooling, the complex processes behind this form of heat transfer.

$$\mathbf{n} \cdot \nabla T = h_c(T_s - T_\infty) \tag{3.1.23}$$

Where $\mathbf{n}$ is the unit vector normal to the surface, T_s is the surface temperature and T_∞ is the saturation temperature of the liquid far away from the heated surface. The dependences of h_c can be defined using dimensional analysis [65]. For the purpose of this thesis, the convective heat transfer has been modeled only as a temperature dependent parameter.

Steady-State Heat Transfer

Heat transfer in pool boiling is greatly dependent on the surface superheat $(T_s - T_\infty)$. In steady-state, the heat transfer occurs according to three basic regimes. The first one, when the surface temperature (T_s) is close to the fluid saturation temperature (T_∞). In this regime, the heat transfer is governed by free convection which is basically driven by buoyancy forces. A further increase of T_s causes the apparition of vapor bubbles that nucleate on the heated surface. Due to the latent heat of vaporization (the phase change is endothermic), large thermal exchange occurs in this range of temperature. This regime (the second) is termed nucleate boiling and is actually one of the most efficient way of transferring heat from solid to liquid. As the temperature continues to increase, the heat transfer continues to grows-up to the maximum value (point G in figure 3.5) for which hydrodynamic processes [66] make the heat transfer unstable. Additional heat will completely cover the heated surface by a vapor blanket isolating the surface from its surroundings. This third regime is termed film boiling. Figure 3.4, shows the nucleate and film boiling in action.

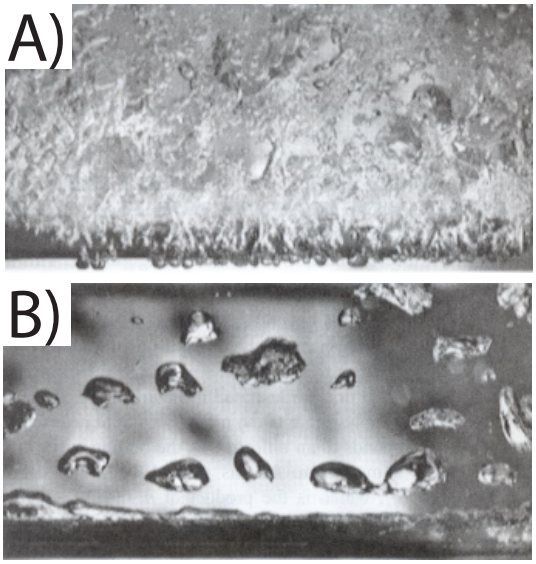

Figure 3.4: Boiling of methanol on a horizontal tube. Nucleate boiling A) and film boiling B) [67]

Transient Heat Transfer

For transient heat transfer, dependently on the heat input rate and amplitude, the film boiling regime is usually reached abruptly without the nucleate boiling phase. However, in certain conditions and for very short inputs, the amount of energy needed to reach the film boiling regime may be larger than the one needed in steady-state [68, 53]. According to the input rate, the mechanism of heat transfer may be of different nature. Basically, at high rates heat transfer is governed by conduction with the coolant. At lower rates, the free-convection equations stick more to the observations. Sakurai *et al.* [53] have investigated the transient heat transfer for different heat inputs in saturated and subcooled nitrogen. According to the heat input, they distinguished three transient regimes (figure 3.5) *i.e.* at a low (dots, orange line), high (circle, red line) and ultra-low (square, blue line) increasing rates.

- **low-rates**: A direct transition from the non-boiling to film boiling regime is observed. The heat transfer is associated to free-convection (as in the steady-state) but changes suddenly to explosive boiling over the whole surface once the surface temperature reaches the point A. Above this temperature, the heat flux enters in a metastable regime (dashed line) that leads to the stable film boiling (point C), which is a constant curve for all the inputs rates (including the steady-state regime).

- **high-rates**: A direct transition is also observed for this regime but this time, the heat transfer is associated to conduction – see [69]. The transition temperature, termed "the heterogeneous spontaneous nucleation temperature" (T_{tr}) is reached at higher flux and surface superheat (point A'). Above this point, the heat transfer changes rapidly to the film boiling regime as in the precedent case.

- **ultra-low-rates**: It is a quasi-steady-state. The mechanism of heat transfer is very similar than in low-rates regimes. Nevertheless, the ultra-low-rates prevents the spontaneous nucleation at the origin of the two precedent mechanism. This allows detachment of bubbles from the surface and causes mixing of the liquid around the surface. This leads to nucleate boiling at point A" slightly below the direct transition (point A). The dashed line (metastable regime) presented in figure 3.5 shows a reduction of the surface temperature. Once the heat transfer reaches the nucleate boiling regime, the heat exchange is identical to the one observed in the steady-state regime (the nucleate boiling curve is independent of the input rates).

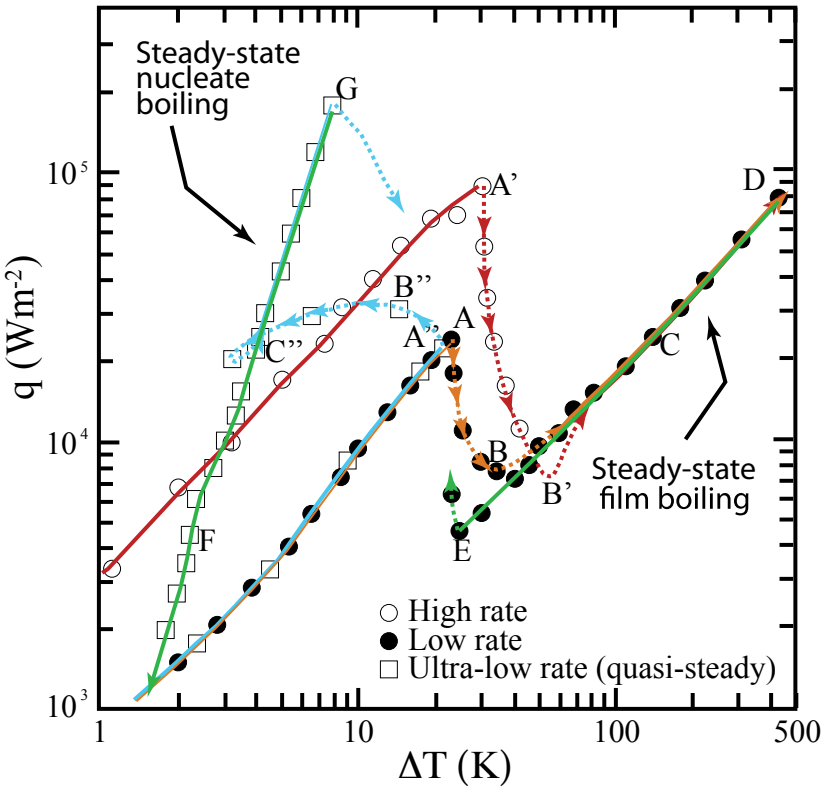

Figure 3.5: Transient heat transfer for exponential heat inputs [53]. The horizontal axis represents the surface superheat and the vertical axis the power per unit of area exchanged with the coolant. See the text for more details.

The green line shown on figure 3.5 represents the recovery from film boiling for transient heat transfer once the vapor blanket has collapsed. The mechanism is similar to the one usually observed in the steady-state but occurs at larger surface superheat. Quantitatively, Sakurai *et al.* have shown that for heat pulses of duration smaller than τ =50 ms, the heterogeneous spontaneous nucleation temperature is approximately constant T_{tr} ≈107.6 K [53] . Armed of this conclusions, it is possible to determine the maximum heat allowable to avoid the direct film boiling transition where the heat transfer rapidly drops.

$$Q_{max} = \int_0^{\tau} \int_S h_c(T(t') - T_\infty) dS' dt' + Q_{st} \tag{3.1.24}$$

where Q_{st} is the heat stored in the material *i.e.*

$$Q_{st} = \int_V \int_{T_\infty}^{T_{tr}} \rho_m Cp(T) dT' dV' \tag{3.1.25}$$

The terms $\int_V$ and $\int_S$ represent respectively the 3D- and 2D-space integration, S is the surface in contact with the coolant and h_c the convective heat transfer coefficient which is basically dependent of the coolant thermal properties, sample geometry and time constant (τ).

For a wire of radius r, having a uniform temperature distribution, Sakurai *et al.* [69] have obtained the following equation for h_c:

$$h_c = \left(\frac{k}{\sqrt{D_{th}\tau}} \frac{K_1(\beta r)}{K_0(\beta r)} \right), \qquad \beta = \frac{1}{\sqrt{D_{th}\tau}} \tag{3.1.26}$$

Where K_1 and K_0 are respectively the first and zero order of the Bessel's equation of second kind. For a given time constant, equation 3.1.26 shows a constant value of the convective heat transfer coefficient, both in the conductive and in the film boiling part.

Subcooled Liquids

If the liquid in pool boiling is maintained at a temperature that is less than the saturation temperature, the liquid is said to be subcooled. In subcooled liquids, the rates observed before are much shorter *i.e.* the ultra-low-rates occur at smaller time constant than in saturated liquids [53]. In addition, the heterogeneous spontaneous nucleation temperature drops of tens of degrees and makes the heat transfer occurring over a smaller range of temperature. Nevertheless, for the quasi-steady state in the nucleate boiling regime, the maximum heat flux can be as much as 2.5 times larger than in saturated liquids. The heat transfer is also improved for higher rates that show a rapid nucleate boiling phase before reaching the film boiling regime. This effect becomes smaller by reducing the input rate. The film boiling curves is not affected in subcooled conditions.

3.1.3 Thermal Stability

This section is ended by the definitions of the thermal stability and of the normal zone propagation velocity. Those concepts are important to define the performance of coated conductors as SFCL elements.

Superconductors are bi-stable systems [70]. As a matter of fact, it is shown that there is a combination of parameters value (J, T and B) for which a defined normal zone initially present in the superconductor remains stationary. Above those values, the normal region grows and below them the normal region collapse. In other words, considering a superconductor containing a weaker region (in terms of J_c), rising one of the parameters of the set (J,T,B) will cause propagation of the normal zone. On the other hand reducing one of them will cause recovery of the superconducting state over the whole sample. Stekly et al. [71] defined a stability criterion based on a steady state interpretation of equation 3.1.1 which stipulates that whatever are the initial conditions, if the current in the sample is below the critical current and if heat generated in the resistive part of the tape is below the heat removed by heat transfer with the surrounding, the recovery is ensured. This criterion is termed cryostability.

$$\alpha = \frac{RI_c^2}{Sh_c(T_c - T_{op})} < 1 \tag{3.1.27}$$

Where S is the surface boundary of the sample, R the tape resistance, T_c and T_{op} the critical and operating temperature. Cryostability is just a special case of a more general theorem developed by Maddock et al. [72] (equal area theorem) which defines the equilibrium condition between a large-normal zone and the cool surrounding far away from its center. Nevertheless this theorem applies only for large perturbation zone which are usually not encountered in typical applications (especially for coated conductor at elevated operating temperature). An other approach is to look at solution for which a specified initial temperature distribution $T(z, 0)$ asymptotically approaches (over time) the operating temperature $T(\pm\infty) = T_{op}$. This solution is termed the minimum propagation zone (MPZ). The MPZ is unstable against small perturbation [73]. That means that the MPZ separates the quenching initial conditions from those that recover. Temperature distributions everywhere greater than the MPZ grow and those everywhere smaller shrink.

Following that, it is generally admitted to set up the MPZ profile as being that required to initiates a quench [74]. Therefore, one may introduce the concept of minimum quench energy (MQE) also termed stability margin, which is defined as the energy required to set up the MPZ. In other word, the enthalpy change of the conductor over the range of the MPZ profile.

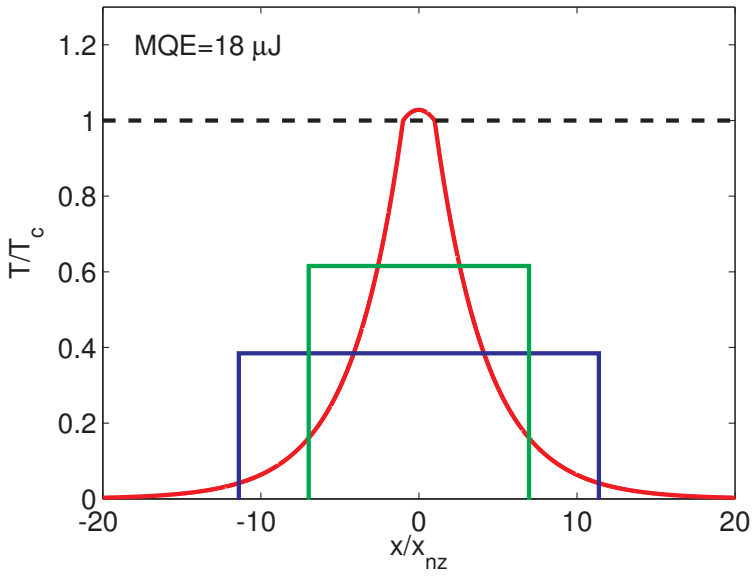

Figure 3.6: Comparison of MPZ profiles. All of them having the same MQE. The red profile is obtained from the calculation presented in Appendix C. The length scale (x_{nz}) of the figure is the part of the red profile that is in the normal state ($T \geq T_c$). The black dashed line is the normalized temperature. This figure shows an hypothetical MQE which is, for instance, of very low value compared to the ones usually found in the literature [48, 50].

$$\text{MQE} = \int_{\mathbf{x}} \int_{T_{op}}^{T(\mathbf{x})} \rho_m C_p dT' d\mathbf{x}' \ , \qquad \mathbf{x} = (x, y, z) \tag{3.1.28}$$

From equation 3.1.28, one can notice that the stability margin depends strongly on the specific heat which usually decreases as the temperature gets lower – see Appendix A. Figure 3.6 shows a typical MPZ obtained from calculations (Appendix C). As observed on the figure, the MQE is quite low compared to the ones found in the literature. Those are orders of magnitude larger [48, 50]. This difference seems to come from the fact that the calculation do not take into account of the heat absorbed by the substrate. More comments on the assumptions made to obtain the MPZ profile are presented in Appendix C.

Traveling Waves and the Normal Zone Propagation Velocity (NZPV)

A boundary between the normal and superconducting phases in a current-carrying wire may be propagated by heat that is generated in normal regions and conducted into adjacent superconducting regions. This conduction of heat raises a portion of the superconducting region above its transition temperature and advances the normal-superconducting boundary. Considering a constant speed of the boundary when the transport current and external field are maintained at a constant level, one may represent the temperature front as a traveling wave [75]. As a matter of fact, starting from the heat balance equation defined by:

$$k\frac{\partial^2 T}{\partial x^2} + \rho_m C_p \frac{\partial T}{\partial x} - \frac{Sh_c}{V}(T - T_{op}) - Q(T) = 0 \tag{3.1.29}$$

V and S being respectively the volume and contact surface of the sample with the coolant. And using the substitution $\xi = x - vt$ (a wave moving along the positive direction) in equation 3.1.29 yields to

$$\frac{\partial T}{\partial t} = \frac{\partial T}{\partial \xi}\frac{\partial \xi}{\partial t} = \frac{\partial T}{\partial \xi} v \tag{3.1.30}$$

$$k\frac{\partial^2 T}{\partial \xi^2} + \rho_m C_p \frac{\partial T}{\partial \xi} v - \frac{Sh_c}{V}(T - T_{op}) - Q(T) = 0 \tag{3.1.31}$$

A tentative of resolution of equation 3.1.31 is made in Appendix D. Using some assumptions, one can obtain an expression of the longitudinal NZPV for adiabatic conditions [75, 76, 73].

$$v = \frac{J}{\rho_m C_p}\left(\frac{\rho_k}{T_c - T_{op}}\right)^{1/2} \tag{3.1.32}$$

Where the thermal parameters in equation 3.1.32, are effective values coming from the sample architecture. Equation 3.1.32, shows a linear variation of the NZPV with the current density (J). This behavior is obviously not observed in coated conductors carrying current above the critical current since the thermal parameters as well as the heat generation term of equation 3.1.1 are varying with the temperature. Nevertheless, this simple model allows to emphasize the role of the specific heat in the NZPV. Comparing equations 3.1.32 and 3.1.28 illustrates the important fact that for a given material operating in given conditions, the stability margin is inversely proportional to the normal zone propagation velocity. Knowing that the specific heat increases with the temperature – see Appendix A, it follows that coated conductors working in liquid nitrogen are very stable in comparison to LTS. However, one side effect is that once a normal zone nucleates in those conductors, it expands very slowly and makes difficult the fault detection.

3.2 The Numerical Model

Getting analytical solutions of partial differential equations (PDEs) is often realized using many simplifications on the equation set for making them "solvable by hands". In addition, solving PDEs, even for simple geometries, is often not possible in an analytical framework (this is specially true for nonlinear PDEs). However, the advent of accessible and efficient computers as well as the development of numerical methods such as the finite element method (FEM) offer now the possibility of solving many practical problems encountered in engineering at a very low cost (in terms of time and personnel). A brief overview of the FEM follows this small introduction, the remaining of this section presents in details the normal zone propagation model constructed during this thesis work as well as the analytical and experimental validation of that model.

3.2.1 Finite Elements Method (FEM)

In few words, the finite element method is a numerical method that allows to approximate the solution of a given problem $u(\mathbf{x})$ in terms of a linear combination of known functions $\phi_j(\mathbf{x})$ (usually polynomials) and undetermined coefficients c_j.

$$u(\mathbf{x}) \approx U_N(\mathbf{x}) = \sum_{j=1}^{N} c_j \phi_j(\mathbf{x}) + \phi_0(\mathbf{x}) \tag{3.2.1}$$

Where, N is the number of problem unknowns and $\phi_0(\mathbf{x})$, functions satisfying the boundary conditions. To achieve this, one must subdivided the problem geometry (domain) in simple shapes termed elements. Each of them being seen as "independent domain" on which the algebraic equations (the elementwise version of equation 3.2.1) are mapped using the properties of the governing equations (PDEs). The final form of the finite elements equations is obtained by assembling the contribution of each element using their mutual relationship. The result is a sparse linear system having basically the form:

$$\mathbf{KU} = \mathbf{f} \tag{3.2.2}$$

Where $\mathbf{K}$ is the coefficient matrix containing the information on the elements relationship and PDEs properties, $\mathbf{U}$ a vector containing the problem unknowns and $\mathbf{f}$ a vector containing the information on the source term and boundary conditions of the PDE.

The FEM is a variational method. Considering correctly posed and imposed the boundary/initial conditions of a given problem, the existence and uniqueness of equation 3.2.1 is ensure if the first variation of the problem functional is minimized [77]. Following the weighted-residuals approach, this condition is achieve by adding a constraint to the system. For instance, the "weighted error" introduced by the approximation of the differential equation. The latter must vanishes over the whole domain *i.e.*

$$\int_{\Omega} w_i(\mathbf{x}) R(\mathbf{x}, c_j) d\mathbf{x} = 0 \tag{3.2.3}$$

$$R(\mathbf{x}, c_j) \equiv \Gamma(U_N) - f \neq 0 \tag{3.2.4}$$

where the weights $w_i(\mathbf{x})$ are orthogonal functions. Following the used method different functions can be chosen *e.g.* $w_i(\mathbf{x}) = \phi_i$ in the Galerkin's method or $w_i(\mathbf{x}) = \delta(\mathbf{x} - \mathbf{x}_i)$ for the collocation method. R is the residual of the operator function $\Gamma(u(\mathbf{x})) = f$. The full description of the FEM is beyond the scope of this thesis. A good introduction to the method can be found in accessible books such as Reddy [77].

3.2.2 The Coupled Model

The FEM numerical model used to simulate the normal zone propagation in coated conductors is based on the coupling of the electrical and the thermal equations where the independents variables (unknowns) are the electric potential V and the temperature T. Those equations are variations of the diffusion equation. The electrical part is the steady-state homogeneous form of equation 3.1.1 *i.e.* with no source and time-derivative:

$$\nabla\big(\sigma\nabla V\big) = 0, \quad \text{in the domain } \Omega \tag{3.2.5}$$

$$V = 0, \quad \text{at } \mathbf{x} = (L, y, z) \tag{3.2.6}$$

$$\frac{\partial V}{\partial \mathbf{n}} = \frac{J_s}{\sigma}, \quad \text{at the left boundary of the superconductor} \tag{3.2.7}$$

$$\frac{\partial V}{\partial \mathbf{n}} = 0, \quad \text{at the remaining boundaries} \tag{3.2.8}$$

where L is the conductor length. The 2D and 3D geometries are respectively displayed in figures 3.7 and 3.14. The thermal part is the transient diffusion equation where the heat transfer with the liquid nitrogen is implemented in the boundary conditions.

$$\rho_m C_p(T)\frac{\partial T}{\partial t} = \nabla\Big(k(T)\nabla T\Big) + Q(T), \quad \text{in the domain, } \Omega \tag{3.2.9}$$

$$\frac{\partial T}{\partial \mathbf{n}} = h(T)\Big(T - T_{op}\Big), \quad \text{at the tape boundary, } \Gamma \tag{3.2.10}$$

The coupling between the electrical and the thermal part of the model operates through the source term $Q(T)$ defined as,

$$Q(T) = \sigma(T)(-\nabla V)^2 \tag{3.2.11}$$

where the conductivity $\sigma(T)$ is implemented using a temperature-dependent power-law

$$\frac{1}{\sigma(T)} = \rho(T) = E(J_s, T)J_s = \frac{E_0}{J_c(T)}\left(\frac{J_s}{J_c(T)}\right)^{n(T)} \tag{3.2.12}$$

Where, $E_0 = 1 \times 10^{-4}$ V/m is the critical field and J_s the current density constraint. This model is based on the assumption that the critical current rapidly drops for $J > J_c(T_{op})$. This drop abruptly increases the resistivity and leads to large magnetic diffusion length in the superconductor [78].

In other words, it is thought that the magnetic diffusion length is much larger than the thermal diffusion length for transport current well above the critical current. Under these circumstances, the overall diffusion is determined by the slowest process *i.e.* the heat propagation. Practically, in the coupled model, the temperature dictates the current density by modifying the magnetic diffusivity constant D_m ($\rho(T)$). At a given time-step, one get the total heat generated in the conductive layers *i.e.* $Q(T)$ by integrating the product $\rho(T)J^2$, where J is fixed by the steady-state diffusion of current.

Based on the diffusivity assumption, there is no needs to use the traditional H formulation [79, 80]. Even if this formulation provides accurate solution for transient currents, it demands to mesh the surrounding of the conductor and solve the transient for additional variables *e.g.* H_x or H_y in 2D. Nonetheless, considering the magnetic diffusion length for the superconductor in the flux-flow regime presented in figure 3.2 (without temperature effects), the thermal diffusion length may be larger than λ_m for transport current values below $1.5I_c(T_{op})$. Taking into account of the results given by the magneto-thermal models [81, 78], the diffusivity assumption seems valid for transport current value above $1.25I_c(T_{op})$. Thus, the simulations presented in this work have been made for transport current values above $1.25I_c(T_{op})$.

3.2.3 The Power-Law parameters

In order to get the field dependence of the power-law parameters and define the flux-flow regime mathematically, fits to experimental curves are made directly in the FEM simulations. To achieve this, recorded voltages such as the one presented in figure 2.4 are compared to the voltage drop observed numerically between two "simulated probes" (figure 3.7). Since the flux-flow measurements are made under uniform magnetic field, the temperature and obviously the field are considered uniform during the simulations (see the left part of figure 2.5). Those facts allow a 2D representation of the problem *i.e.* to model only the length (x) and thickness (y) of the conductor. The coupled model geometry and boundary conditions are presented in figure 3.7. The simulated tape has the following dimensions, *i.e.* respectively 50, 0.1, 1 and 2 μm for the substrate (hastelloy), buffer (for this work, a single layer of MgO), superconductor (YBCO) and stabilizer (Ag). The modeled length is 10 mm. The current constraint (equation 3.2.7), is imposed at the left boundary of the superconductor and the zero voltage constraint (equation 3.2.6) at the right boundary of all the layers. The external magnetic field is directly implemented in the expression of $J_c(B,T)$ and $n(B,T)$ which are the fitting parameters of the model.

In order to have a first guess on those value *i.e.* $J_c(B)$ and $n(B)$, curve fittings (using a Non-Linear Least-Square method) are applied on the curves presented in figure 2.6. The fits allowed to observe that both J_c and n reduces under external magnetic field (figure 3.8). Note that the fits at low external magnetic field are not significant since few measurements are available in this field range – see section 2.2. Thus the parameters under zero-field have bean taken from the manufacturer product-data-sheet [41].

The external magnetic field as well as the transport current are parameters that can be isolated with relative ease during the experiments. Nevertheless, as depicted in the experimental part of this thesis, the condition of constant temperature is difficult to achieve when one is looking at the super-normal transition under transport current above the critical current. It is expected that J_c and probably n vary with the temperature (in the normal state the conductor is ohmic *i.e.* n =1). Nevertheless, the measurements of $J_c(T)$ and $n(T)$ are not obvious considering the equipment at disposition while this work has been done (need to increase the liquid nitrogen temperature above 77 K). However, it is customary to define the critical current density as varying linearly with the temperature [48, 17]:

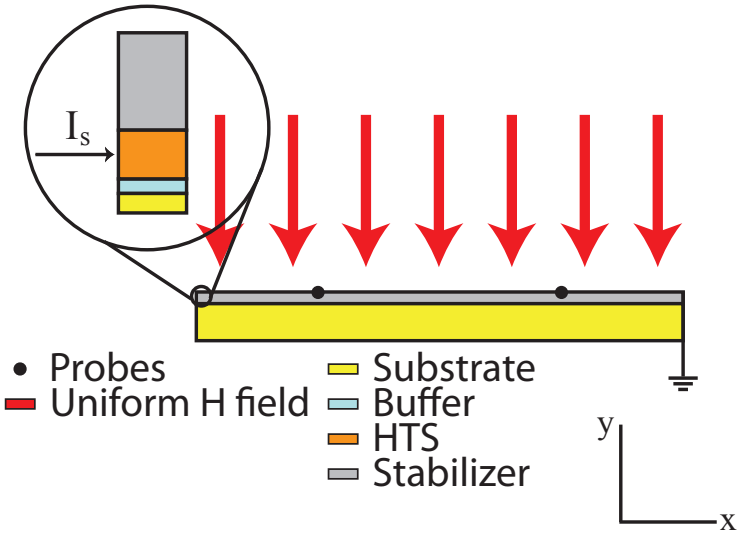

Figure 3.7: Model definition of the 2D model. The red arrows represent the uniform magnetic field. The black dots shows the location of the "simulated voltage probes". Those are located 5 mm apart and used to compare the simulated voltages with the experimental data. The figure is not to scale.

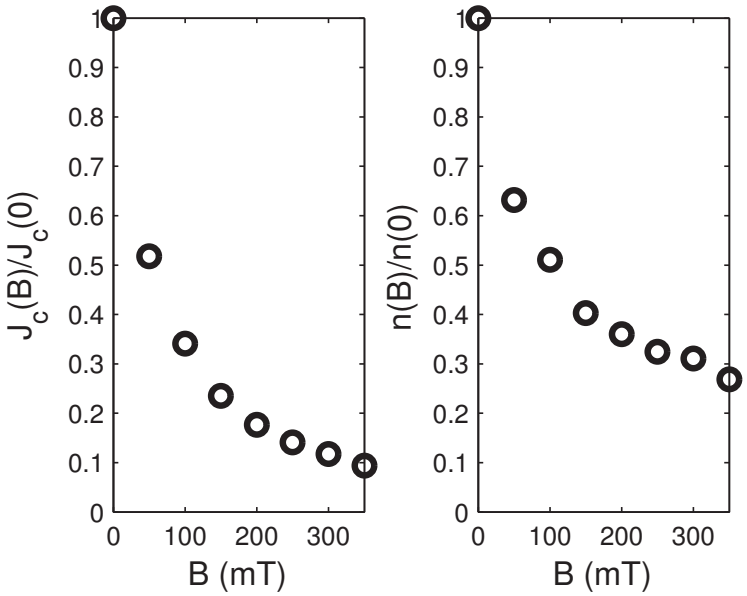

Figure 3.8: Variation of $J_c(B)$ and $n(B)$ obtained from fits to the E-J curves (figure 2.6) and model implementation. The value of $J_c(0)$ and $n(0)$ are respectively of 2.25×10^{10} A/m^2 and 20.

$$J_c(B,T) = \begin{cases} \left(J_c(B) - \frac{E_0}{\rho_{norm}}\right)\frac{T_c - T}{T_c - T_0} + \frac{E_0}{\rho_{norm}} & T < T_c \\ \frac{E_0}{\rho_{norm}} & T \geq T_c \end{cases} \tag{3.2.13}$$

Concerning the power law exponent n. Experiments have shown an abrupt reduction of the exponent at the critical temperature when the conductor becomes ohmic. Since n is a quantity having no real physical significance the following expression, gives good fits to the experimental data, is used for the thermal dependence of the power-law exponent.

$$n(B,T) = \begin{cases} \big(n(B) - 1\big)\left(\frac{T_c - T}{T_c - T_0}\right)^{1/4} + 1 & T < T_c \\ 1 & T \geq T_c \end{cases} \tag{3.2.14}$$

Having acceptable expressions for the temperature and field dependence of the power-law parameters allows to get good fits to experimental data *i.e.* the time-resolved voltage traces obtained during the current pulses. Especially those for which the external magnetic field is important. Figure 3.9 illustrates one example. As depicted on that figure, one may note the typical kink observed at the normal transition *i.e.* when the current is diverted from the superconductor to the stabilizer. The maximum (uniform) temperature reached with this particular simulation is approximately 204 K. This value is in accordance with the estimated temperature coming from the temperature-dependent tape resistivity curve (figure 2.3). Even if good fits are obtained one may note that the flux-flow part of the voltage curve (before the kink) is steeper than the experimental voltage. This phenomenon becomes more important if the external magnetic field is reduced. It is expected that this is coming from the power-law that seems not appropriate at low field values. As a matter of fact, reducing the external field, increase the power-law exponent which in turns amplified the steepness of the flux-flow part of the curve (the empirical factor "n" have important effects on the solution). Ultimately, the error becomes very large under those smaller external fields (figure 3.10). This is happening since the abrupt transition observed experimentally occurs at different times in the simulations. Further investigation have to be done to model the flux-flow regime for the used conditions and then get better fits to experimental data.

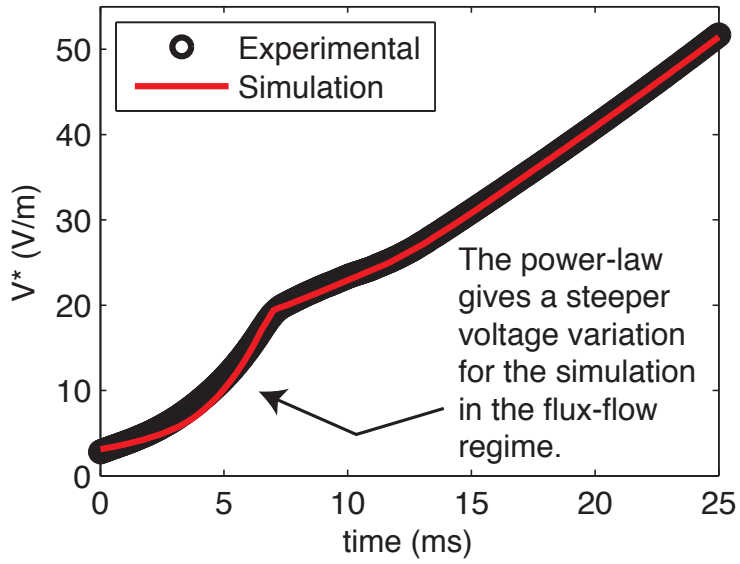

Figure 3.9: A typical comparison of experimental (black circle) and simulated (red line) voltage curve obtained during a pulse of 82 A with a uniform external field of 350 mT.

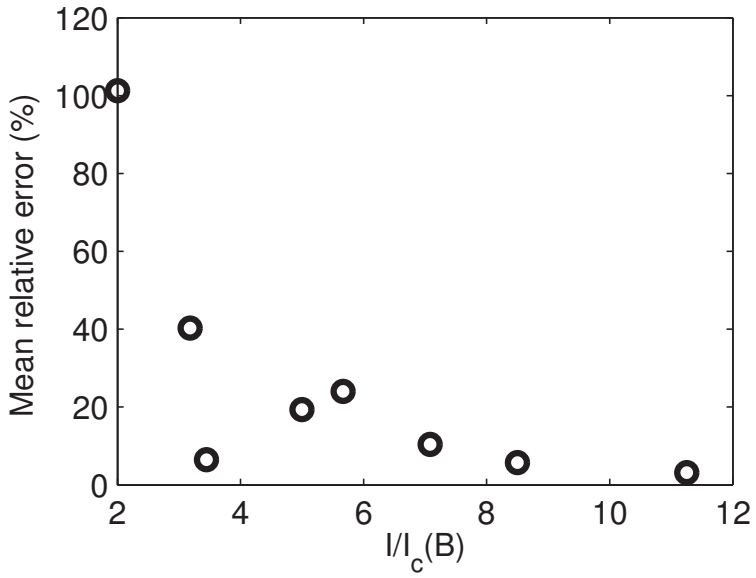

Figure 3.10: Mean relative error defined as $100|T_{\text{exp}} - T_{\text{sim}}|/T_{\text{exp}}$ as a function of the normalized current. Note that better fits are achieved by considering a reduction of the power-law exponent with larger current (self-field effect). The error grows with the reduction of the ratio $I/I_c(B)$ since the high value of the exponent $n(B)$ increases the voltage traces curvature.

During the experiments, there was an electrical contact between the substrate and the conductive layers at the current leads. Accordingly, there was an uncertainty about the amount of current passing into the substrate during those experiments. This complicated the curve fittings to the recorded voltages. For this numerical model, the current is allowed to pass through the buffer layer by assigning a finite resistivity to that layer (the normal resistivity of the HTS).

3.2.4 Meshing and the Analytical Validation of the Thermal Part

Since the FEM solution is dependent on the way the elements are defined in the model, one must consider the effect of the element size and of the interpolation functions on the accuracy of the solution. Since the dynamic of the normal zone propagation is simulated in the thermal part of the model, a comparison is made between the results obtained from a thermal-transient problem solved analytically and its FEM implementation. The problem is defined in two dimensions since the conductor width is usually neglected in this work. The description of the problem is presented in figure 3.11 as well as with the following equations:

$$\begin{aligned} \rho_m C_p \frac{\partial T(\mathbf{x},t)}{\partial t} &= \nabla\Big(k\nabla T(\mathbf{x},t)\Big), \quad \text{in } \Omega \\ T(\mathbf{x},0) &= 1, \quad \text{in } \Omega \\ T(t) &= 0, \quad \text{on } \Gamma \end{aligned} \tag{3.2.15}$$

Using Green's functions (as presented in Appendix B), the analytical solution of equation 3.2.15 is given by the following infinite series [82].

$$\begin{aligned} T(x,y,t) = \frac{16T_0}{\pi^2}\Bigg\{\sum_{n=0}^{\infty}\frac{1}{2n+1}\sin\left[\frac{(2n+1)\pi x}{L}\right]\exp\left[-\frac{\pi^2(2n+1)^2 D_{th}t}{L^2}\right]\Bigg\} \\ \times\Bigg\{\sum_{m=0}^{\infty}\frac{1}{2m+1}\sin\left[\frac{(2m+1)\pi y}{d}\right]\exp\left[-\frac{\pi^2(2m+1)^2 D_{th}t}{d^2}\right]\Bigg\} \end{aligned} \tag{3.2.16}$$

Figure 3.12 displays the accuracies for 1st order mapped meshes with an aspect ratio (width/height) of AR=1. The number of element along the thickness of the geometry correspond respectively to 2, 4, 8, 16, 32 and 64 elements as the increasing order of degrees of freedoms (dofs) displayed on the legend. From the figure, one may show that the error becomes negligible when the FEM model has more than 1 400 dofs. This correspond to 70 elements per square-millimeter *i.e.* when the element size is comparable to 1/16 times the thermal diffusion length. The relative error is defined as $100|T_a - T_n|/T_n$ where T_a and T_n are respectively the analytical and numerical results.

The left part of figure 3.13, depicts the effect of the mesh shape and order as a function of the dofs on the relative error. From this graph, one may note that the error is reduced to an acceptable value above 1000 dofs whatever are the element shape and order. In addition, the right part of figure 3.13 shows that deformed aspect ratio (up to AR=0.03) have little influence on the solution. Thus, as far

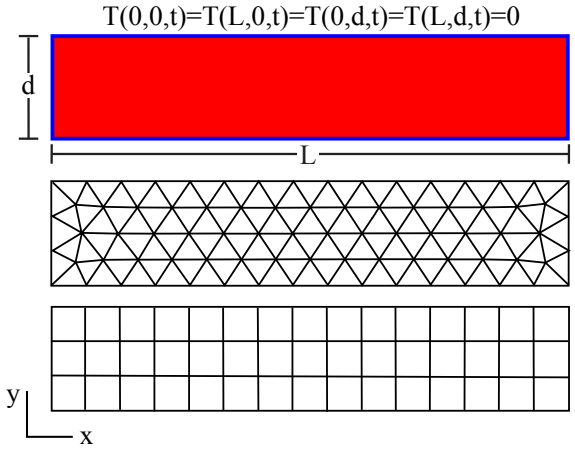

Figure 3.11: The geometry and boundary/initial conditions used to validate the thermal part. The length L (here along the x direction) is 10 mm and thickness d (y direction) is 2 mm. The figure shows different tested mesh *i.e.* triangular and mapped.

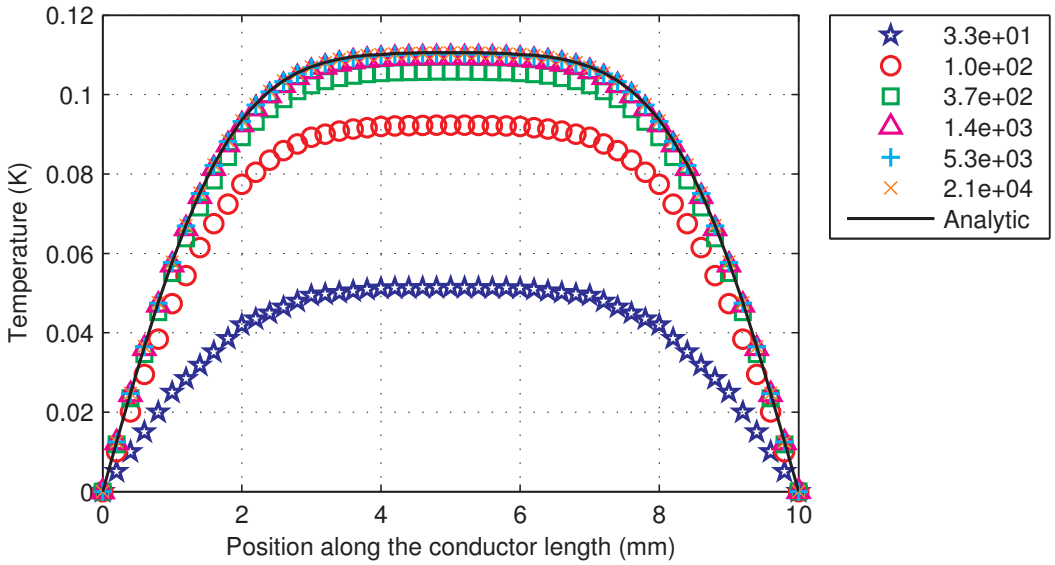

Figure 3.12: Comparison of the analytical solution with the FEM model for the problem defined by equation 3.2.15. The curves show the temperature profile at $t = 160$ ms, the time at which the thermal diffusion length (λ_{th}) is equal to the tape thickness. Each marker represents the number of dofs for square elements (mapped). The element aspect ratio (AR) equals to one for all the case presented here *i.e.* width/height=1. The absolute tolerance used for the solver steps is set to 1×10^{-6}.

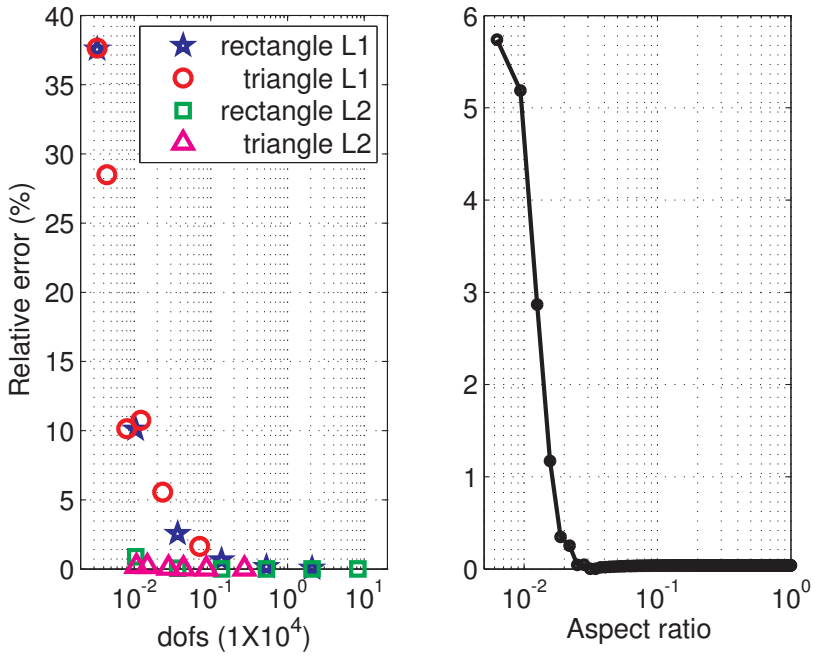

Figure 3.13: Left: Accuracy of the solution as a function of the number of dofs for different element shape and order. Right: Effect of the element aspect ratio for 1st order mapped elements (64 elements along the thickness). L1 and L2 represents respectively 1st and 2nd order elements.

as the size of the elements is smaller than 1/16 times the diffusion length, the solution is accurate independently of the element shape and order. Since 1st order elements have shown to respond better to steep problems [83], those elements are employed for the remaining of this work.

3.2.5 The Experimental Validation of the Coupled Model

To experimentally validate the numerical model, a 3D coupled model is built using the power-law parameters obtained previously as well as using the data acquired from the experiments *i.e.* field maps, voltage traces *etc*. For sake of time computation, this model simulates only half of the sample geometry (symmetry of the problem) but used the usual dimensions, *i.e.* respectively 50, 0.1, 1 and 2 μm for the substrate (hastelloy), buffer (for this work, a single layer of MgO), superconductor (YBCO) and stabilizer (Ag). The modeled length is 10 mm. The results of the 3D-simulations, present good fits to the time-resolved voltage curves obtained experimentally, for instance, see figure 3.15. The small inaccuracies observed on the simulated voltages seems to come from the coarse meshes used for the 3D models as well as to the power-law used to simulate the flux-flow regime that gives steep resistive transition (see figure 3.9). The good match obtained from the fits allows to confirm some observations made in the experimental section – see section 2.3. In the simulation, the transition from section to section occurs once the former section has transited (the kink appears when the current is diverted into the stabilizer). In addition, the temperature range obtained with the model is in the same order of magnitude than the ones estimated from the temperature-dependent tape resistivity curve (figure 2.3). The modeled NZPV is approximately 10% accurate in comparison to the measured values. Due to the size of the 3D problems, few simulations are done here. As a matter of fact, the computation time is roughly 30 minutes for 21 210 dofs with an absolute tolerance of 1×10^{-4} for 1st order mapped elements. The simulations used for comparison are presented in figure 3.16. Those are made at coil-current of 1 A.

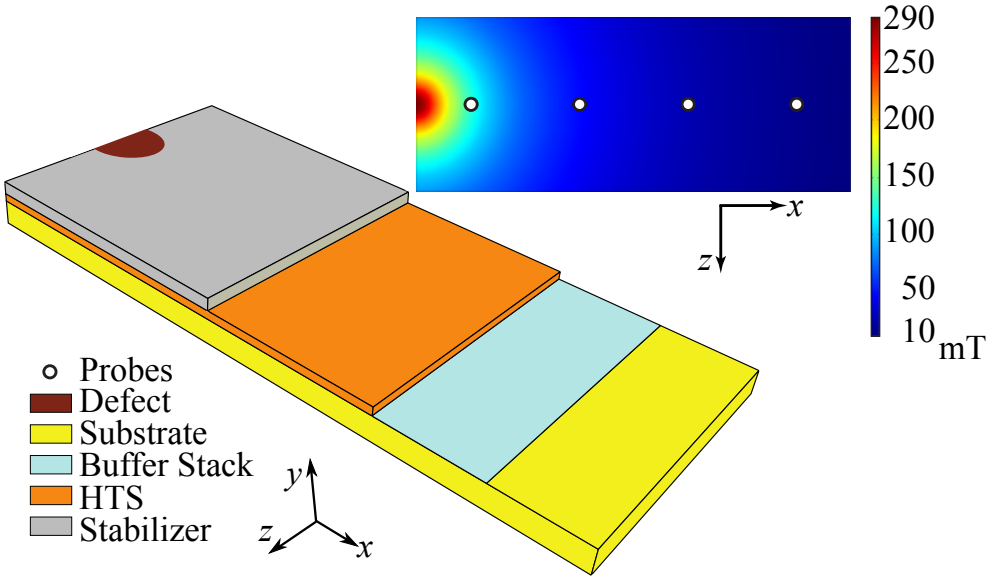

Figure 3.14: The 3D geometry. Simulated "probes" are located at the same location then in the experimental measurements *i.e.* respectively placed at 1.25, 3.75 6.25 and 8.75 mm of the defect center along the tape length on the center of the stabilizer surface (white dots). The boundary conditions are the same as in the 2D case, – see figure 3.7. The 2D surface map of the magnetic field obtained from experimental data is placed in inset. The thickness of the layers are the following: substrate 50 μm, buffer 0.1 μm, HTS 1 μm and stabilizer 2 μm. The tape width is 4 mm and the modeled length 10 mm.

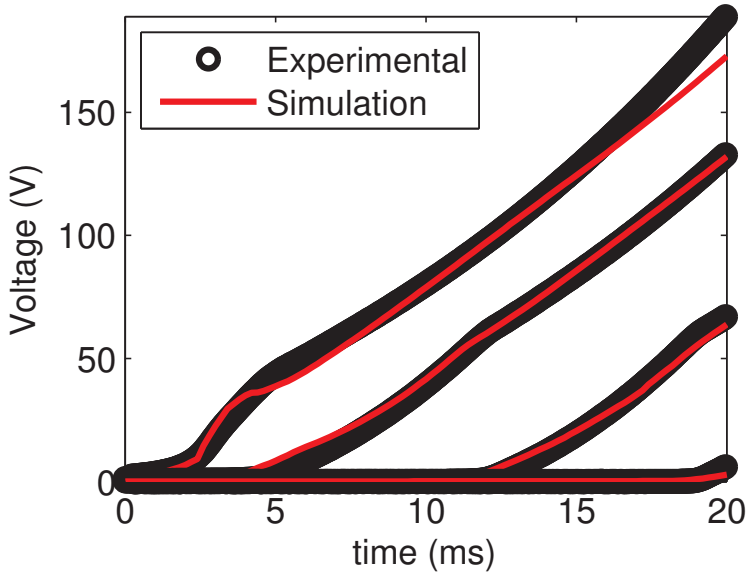

Figure 3.15: A typical voltage comparison for a 128 A pulse with coil-current of 1.0 A . The maximum temperature obtained at the center of the tape is 425 K. The latter is comparable to the estimation made with the temperature-dependent tape resistivity curve (figure 2.3).

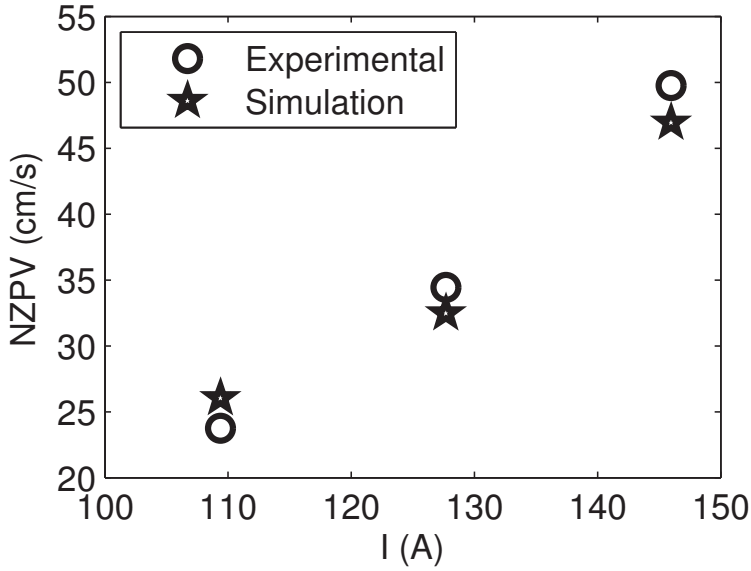

Figure 3.16: Comparison of the NZPV computed by FEM with the experimental results for pulse of I=109, 128 and 146 A for a coil-current of 1 A. The relative error is less than 10% for the simulated cases.

3.3 Simulation of Coated Conductors

The experimental validation of the coupled model allows a deeper investigation of the design features that may affect the behavior of coated conductors as SFCL elements. In the present section, a brief overview of those features is presented. For sake of simplicity, the model is implemented in two dimensions. In other words, this means that a uniform flaw along the width of the conductor is considered. For this case study, the initial defect is implemented as a drop of the critical current along the length of the conductor – see the inset of figure 3.17. This drop is mathematically represented by the following equation:

$$\frac{J_c}{J_{c0}} = 1 - f \exp\left(-d_a(x - x_0)^2\right) \tag{3.3.1}$$

Where f and d_a are respectively the amplitude and width of the Gaussian distribution and x_0 the location of the defect center. Figure 3.17, depicts the geometry (a 10 mm long sample). The used dimensions are respectively 50, 0.1, 1 and 2 μm for the substrate (hastelloy), buffer (for this work, a single layer of MgO), superconductor (YBCO) and stabilizer (Ag). The x and y axis respectively represent the length and thickness of the tape. In order to look at the interface losses [84, 85, 86], an additional layer has been introduced between the superconductor and the stabilizer. The interface acts as a finite contact resistance between those layers.

The remaining of this section presents the effect of the substrate thermal properties as well as of the resistive effects and transient heat transfer on the NZPV. This section is conclude by a brief summary on those parameter effects on the minimum quench energy (MQE).

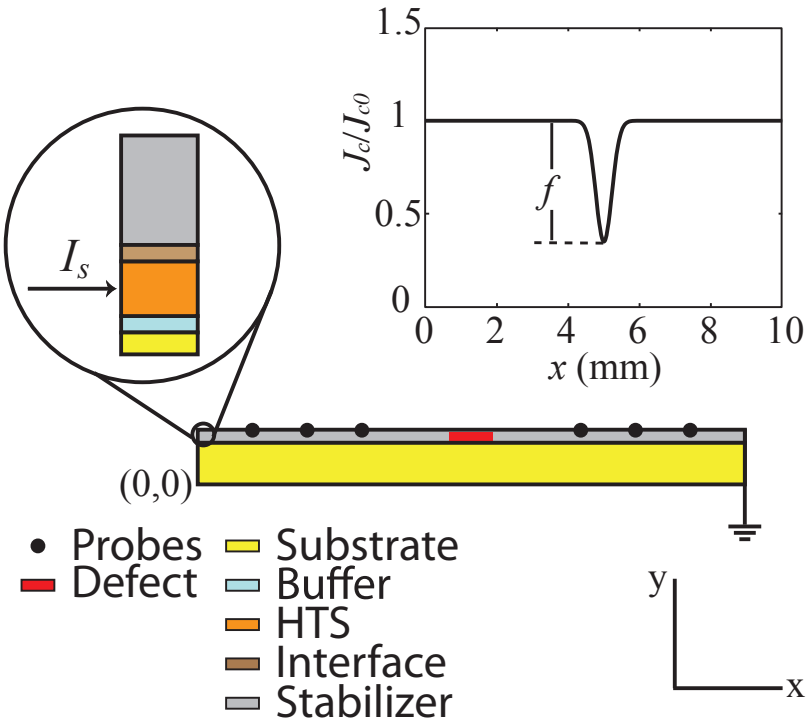

Figure 3.17: Non-scaled geometry of the model used for the simulations. The initial flaw (in red as well as in the inset), is implemented as a drop of the critical current density along the length of the conductor. The "probes" used to monitor the voltage are located at x=1, 2, 3, 7, 8 and 9 mm along the tape length (10 mm). The thickness of the layers are the following: substrate 50 μm, buffer 0.1 μm, HTS 1 μm, interface 0.1 μm and stabilizer 2 μm.

3.3.1 Substrate Thermal Properties

It has been experimentally observed that thermally diffusive substrates ensure a uniform normal zone propagation during quenches [49]. To observe this effect numerically, two usual substrate materials have been compared, that are hastelloy and sapphire. For the simulations, adiabatic conditions are assumed (no heat transfer with the nitrogen bath). In addition, constant parameters are used for the interface layer. Those parameters are: $\rho_{\text{int}} = \rho_n(T_c)$ (the normal resistance along the ab plane), C_p =245 J/kg.K, ρ_m =6 400 kg/m^3 and K =8 W/m.K. Note that it is customary to used the unit-area-resistance defined as $R^*_{\text{int}} = \rho_{\text{int}} d_{\text{int}}$ instead of the interface resistivity (ρ_{int}) for a thin resistive layer. Accordingly, the interface resistance used for this subsection is $R^* \approx 3 \times 10^{-10}$ Ωcm^2. The latter is actually 2-3 order of magnitude lower than the resistance usually observed in commercial coated conductors [84, 85, 86]. The effect of that resistance will be studied latter in this section (page 51).

Figure 3.18, shows the effect of the substrate on the temperature profile for the hastelloy and sapphire case submitted to a current pulse of I =1.25$I_c(T_{op})$ at percentage of time needed to reach the quench (detection) criterion. This criterion having been arbitrary chosen such that the section resistance equals 0.2 mΩ at 4 mm of the defect center (x_0 =5 mm). From that figure, one can note that the low thermal diffusivity of hastelloy and YBCO result in a very localized heat generation in the superconducting film. For the hastelloy substrate, the sample temperature in the conductor may reach 300 K and that even before obtaining the quench criterion. From the simulations, the normal zone propagation velocity is approximately 20 times larger for sapphire than for hastelloy (5.351 m/s vs 0.302 m/s). Note that the low specific heat of sapphire makes this substrate less stable thermally – see figure 3.18. Using sapphire substrate would imply thicker substrate and/or stabilizer (see next

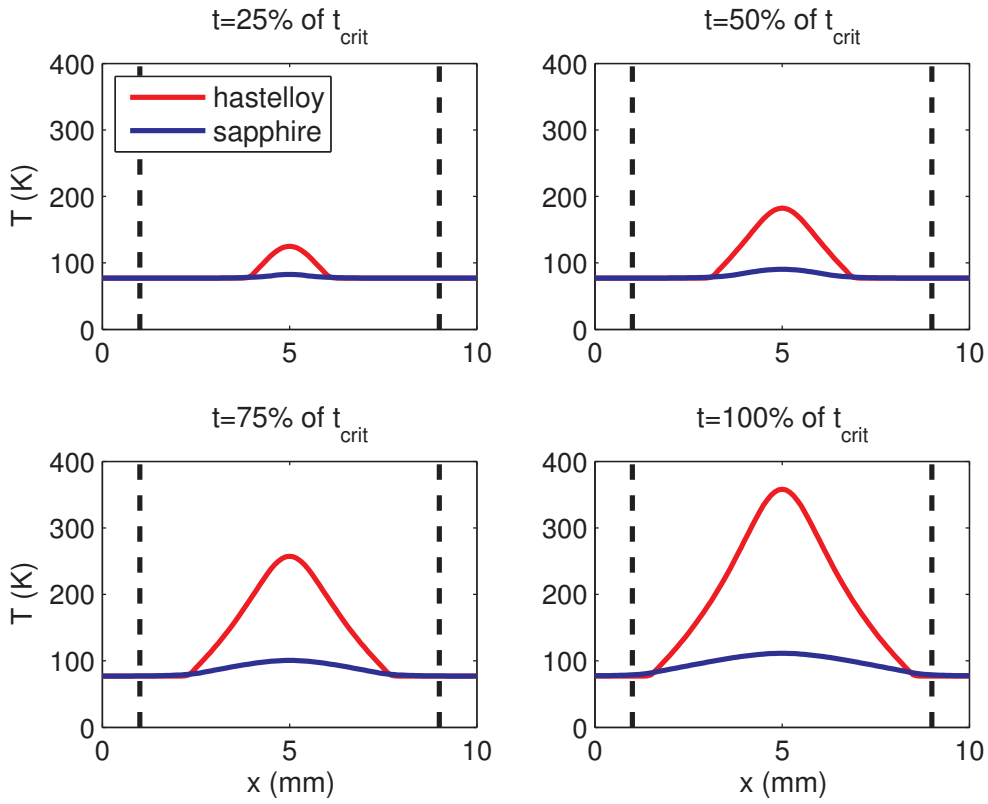

Figure 3.18: Temperature profiles at different time for sapphire and hastelloy substrate under current pulse of I =1.25$I_c(T_{op})$. Each quadrant shows the profiles for fractions of the quench criterion time *i.e.* when R =0.2 mΩ at the black dashed-lines. The criterion time for sapphire and hastelloy is respectively of 0.75 ms and 13.25 ms.

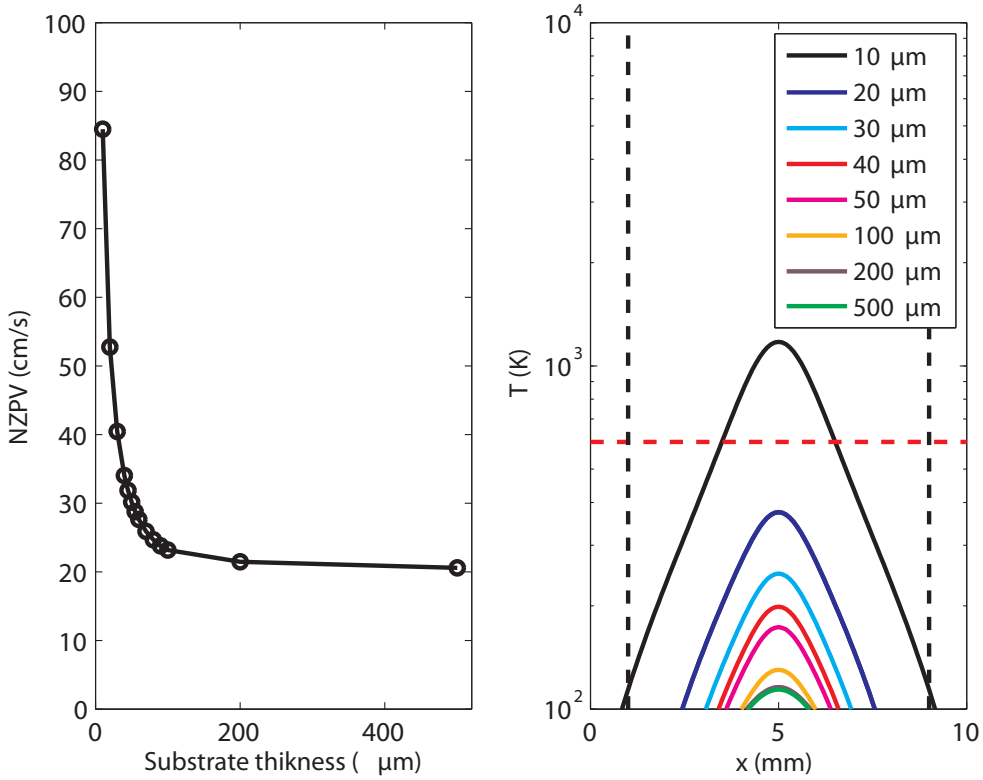

Figure 3.19: On the left: Normal zone propagation velocity as a function of the hastelloy thickness under current pulse of $I = 1.25 I_c(T_{op})$. On the right: Temperature profile corresponding to those simulations at $t = 10$ ms. The red dashed-line correspond to irreversible damage in the conductors ($\approx$600 K) [51]. The black dashed-line shows the quench criterion distance.

page) in order to increase the fault duration that the tape can sustain (reduce the temperature excursion once the tape has transited).

Figure 3.19 shows the simulated NZPV variation for hastelloy as a function of the substrate thickness for transport current of $I = 1.25 I_c(T_{op})$. As expected, thicker substrates (larger mass), absorb more heat and accordingly, reduce the NZPV. However, one may note that the NZPV tends to becomes constant as the substrate thickness increases. Consequently, it seems that thicker substrates would reduce the temperature excursion without notable reductions of the NZPV and thus improve the tape performances. This is observed since the NZPV is mostly driven by heat generated in the conductive layers (hastelloy has a poor thermal diffusivity). Note that reducing the hastelloy thickness improves the NZPV but also increases the risk of generating hot spots.

3.3.2 Resistive Effects

In the NZPV analysis presented in Appendix D, the effect of current sharing with the stabilizer has not been taken into account. Considering tapes submitted to a current source, one may thought that the addition of the stabilizer, which reduces the overall resistance of the tape, may lower losses when the transport current is larger than the critical current and thus reduces the NZPV. Accordingly, rising the resistance of the stabilizer may increases Joule losses and improves the NZPV. This can be achieved using materials of larger resistivity or through a reduction of the stabilizer thickness.

Figure 3.20 compares the effect of different stabilizer configurations on the resistive transition (voltage traces) for the interface-layer-parameters given in the previous subsection (page 49). The red, green and blue curves displayed on the figure show the voltage traces obtain from simulations using different stabilizer of different thickness but having the same resistivity (silver). The yellow curve shows the voltage traces for simulations made with a stabilizer having twice the resistivity of the previous cases (red, green and blue) but having the thickness of the green case. Thus, the yellow and red case have the same resistance (at constant temperature). However it is shown on the figure that, due to its larger resistivity, the transition in the yellow case (twice the resistivity with twice the thickness of the red case) occurs before the red case. Nevertheless, since the resistivity is temperature-dependent, the heat generated in the stabilizer in the thinner layer (red case) rapidly overtake the resistivity of the thicker layer (yellow case) and finally makes a faster transition for the red case. One may note that the voltage slopes of the curves as well as the kink heights are reduced with the resistance of the stabilizer ($R = \rho L/S$, where L and S are respectively the length and cross-section of the stabilizer) *i.e.* the current is diverted into the stabilizer when the superconductor and stabilizer have comparable resistance. The reduction of the voltage slopes illustrates the "electrically stabilizing" role of the stabilizer which also helps to reduce the voltage overshoot that may be observed during the transition.

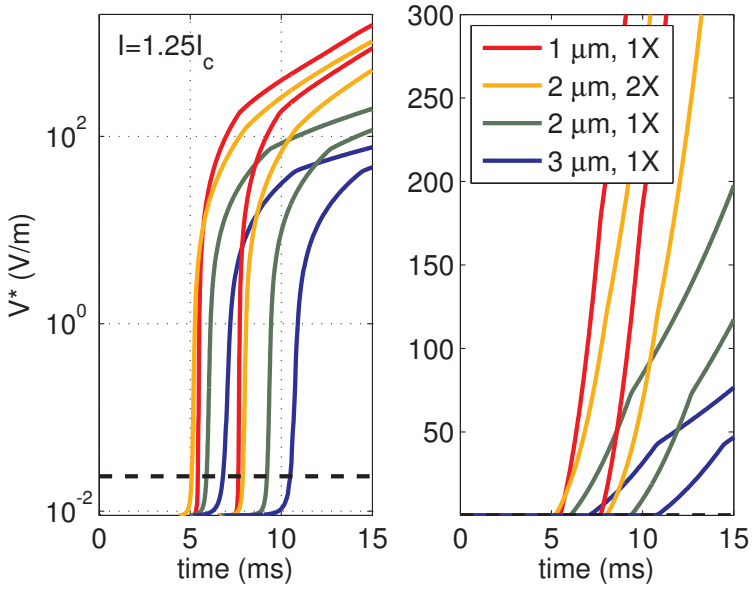

Figure 3.20: This figure shows the built-up voltages (left log scale, right linear) for two adjacent sections of the simulated defect for different stabilizer thickness and resistivity (2x means twice the resistivity). The corresponding NZPV (from top to bottom of the legend) are respectively: 45, 36, 32 and 26 cm/s. The dashed line represent the NZPV criterion. The high voltage values are obviously not observable in our physical world (the tapes would have burned for a while). However, those values show the fault time-scales to not overpass for the associated design in these particular conditions.

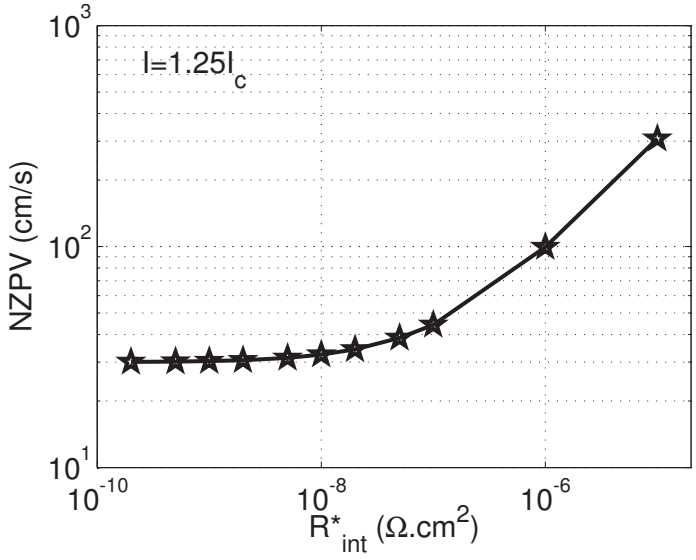

Figure 3.21: Effect of the interface resistivity on the NZPV for a transport current of $1.25I_c(T_{op})$.

Finally, note that the substrate resistance is greatly reduced by its thickness (the substrate is respectively 50 and 25 times thicker than the HTS and stabilizer layers). If we compare the corresponding hastelloy resistance (R_{Ha}) to the resistance of the normal YBCO (R_{HTS}) at 300 K, one can obtain the following factor.

$$\frac{R_{\text{Ha}}}{R_{\text{HTS}}} = \frac{d_{\text{HTS}}}{d_{\text{Ha}}} \frac{\rho_{\text{Ha}}}{\rho_{\text{HTS}}} \approx \frac{1}{30} \tag{3.3.2}$$

This fact allows a certain amount of current to be diverted in the substrate if an electrical path exist with the other conductive layers. The overall effect will be a reduction of the tape resistance and similar effect as those presented in figure 3.20.

Still on the resistive effects, Levin *et al.* [87] have recently observed that increasing the contact resistance between the superconductor and stabilizer allows a decrease of the maximum temperature, an increase of the NZPV and a reduction of the stability margin. Figure 3.21 shows the effect of the interface resistance on the NZPV obtained numerically for a transport current of $1.25I_c(T_{op})$.

The benefit of deliberately adding a resistive layer at the interface is shown by increasing the current transfer length (CTL), *i.e.* increasing the normal zone size. Figure 3.22 and 3.23 respectively show the criterion used to defined the CTL and the variation of the CTL with the interface resistance. From figure 3.22, it is shown that the CTL does not vary along time for a given R^*. This is expected since the temperature profile of the CTL is thought to move with the super-normal boundary (the interface resistance is constant along the length of the conductor).

Figure 3.23, depicts the CTL variation as a function of the interface resistance. The red and blue lines respectively correspond to the superconductor and stabilizer screening-lengths defined by equations 3.1.21 and 3.1.22. The CTL values obtained with the simulations are strangely located in between those lines instead of lying on the blue line. As a matter of fact, it is though that the potential difference between the layers (at the origin of the CTL) is mostly governed by the smallest length, *i.e.* the layer having the largest resistivity, the blue line [64]. Note also that the CTL seems to asymptotically reaches a minimum for values of R^* below 5×10^{-9} Ωcm^2. This value corresponds more or less to the superconductor normal resistivity *i.e.* $\rho_n d_{\text{HTS}} \approx R^*$. It is not clear if the discrepancy observed is coming from numerical artifacts (boundary conditions, mesh *etc.*), from the used definition of the CTL (intersection of curves) or a misunderstanding of the phenomenon. Further investigations have to be done to clarify this result. Nevertheless, one may note that the CTL increases in proportion to the square-root of the interface resistance (at least from $R^* = 1 \times 10^{-8}$ to $R^* = 1 \times 10^{-7}$ Ωcm^2).

Figure 3.25 shows the temperature at the center of the defect as a function of time for different interface resistance. One amazing feature of using highly resistive interface is that an increase of the NZPV is obtained without any additional losses (temperature increase).

In summary, current sharing changes the NZPV. Reducing the stabilizer resistance lower losses and the NZPV. Increasing the interface resistance between the superconductor and the stabilizer may have beneficial effect on the propagation scheme by increasing the NZPV and the CTL without notably increasing the temperature in the normal region.

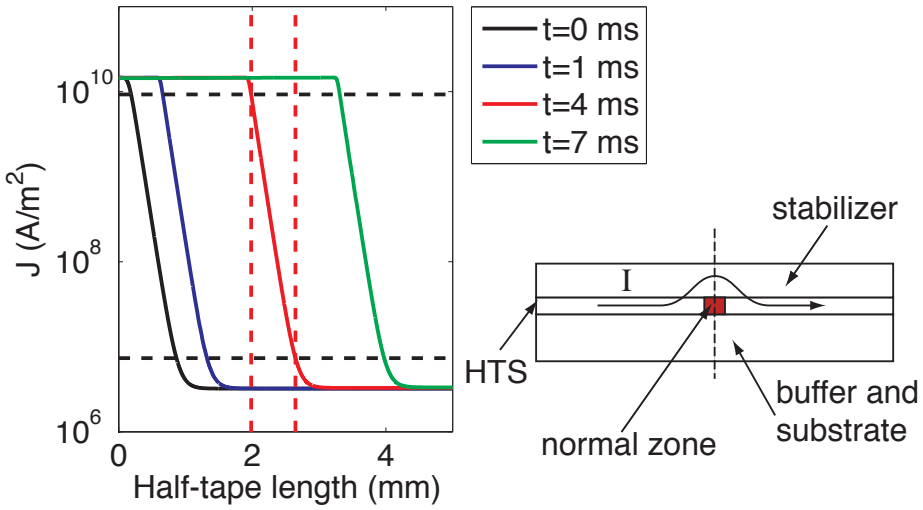

Figure 3.22: When a region of the superconductor is in the normal state, the current is diverted in the stabilizer (right schematic). In this work, the numerical definition of the current transfer length (CTL) is obtained by looking at the distance at which the current density in the stabilizer drops from 63% to nearly 0% of its maximum value *i.e.* when the current returns in the superconductor (right schematic). The black dashed-line corresponds to the CTL criteria *i.e.* respectively J =0.63J_{max} and J =0.0005J_{max} where $J_{\text{max}} = J_c(T_{op})d_{\text{HTS}}/d_{\text{st}}$. This particular figure shows the current density in the stabilizer for an interface resistance of $R^* = 1 \times 10^{-7}$ Ωcm^2 at different times of the simulation. The CTL, delimited by the red dashed-lines, is approximately 0.7 mm for a transport current of I =1.25$I_c(T_{op})$ and is constant at each time step.

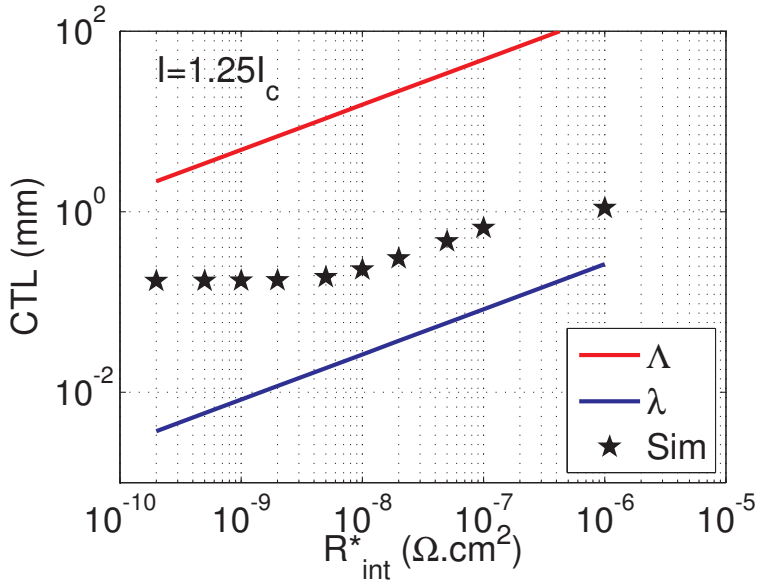

Figure 3.23: Effect of the interface resistance (R^*) on the current transfer length.

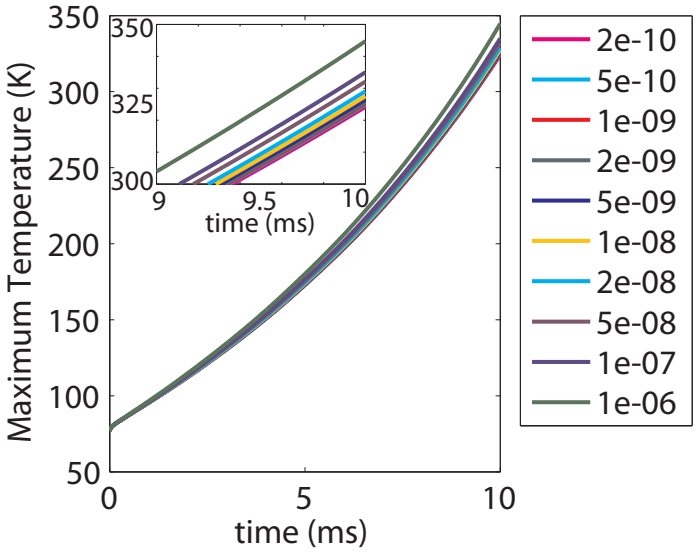

Figure 3.24: The maximum temperature at the center of the defect for different interface resistances as a function of time. The transport current is $I = 1.25 I_c(T_{op})$. The legend displays the interface resistances in Ωcm^2

3.3.3 Heat Transfer and MQE

Quenching of superconductors is thought to be an adiabatic phenomenon since the thermal diffusion is usually expected to be much smaller than the magnetic one *i.e.* $D_{th} \ll D_m$ [73]. In other words the time needed to move heat from one point to another is believed to be much longer than the time needed to create heat (with current) at the same location. This assumption seems right during quenches of tens of milliseconds since, during those pulses, the temperature grows rapidly above the relatively small value of the transition temperature (T_{tr} ≈107 K) –see section 3.1.2. To confirm this assumption a convective heat transfer is implemented in the model. Since the transient heat transfer is difficult to estimate –see section 3.1.2, the steady state curve (nucleate and film boiling) is used to simulate the heat transfer. This choice gives an overestimation of the heat transfer since, at the time scale and range of the pulses energy, lower exchange are expected with the coolant. Figure 3.25 shows the comparison of the NZPV between the adiabatic and pool boiling simulations as a function of the transport current.

For transport current above $I = 1.25 I_c(T_{op})$, the huge amount of energy generated in the stabilizer prevents cooling of the conductor while its quenching. Thus, heat transfer have negligible effects on the NZPV (figure 3.25). However, heat transfer makes coated conductors less sensitive to quench if the fault energy is in the range of the Minimum Quench Energy (MQE) *i.e.* near $I = I_c$. Accordingly, the MQE for four base cases is investigated *i.e.* adiabatic, pool boiling, adiabatic with a sapphire substrate (as opposed to hastelloy) and adiabatic with an increased interface resistivity. The variable of each of these simulations is summarized in the table below:

Table 3.2: Parameters for the four base cases of the MQE investigation. The numbers in parenthesis give the simulation number (figure 3.27).

Simulation	R^* [Ωcm^2]	D_{th} [m^2/s]	h_c
Adiabatic (1)	3×10^{-10}	5	no
Pool boiling (2)	3×10^{-10}	5	yes
Increased interface resistance (3)	1×10^{-6}	5	no
Sapphire substrate (4)	3×10^{-10}	4595	no

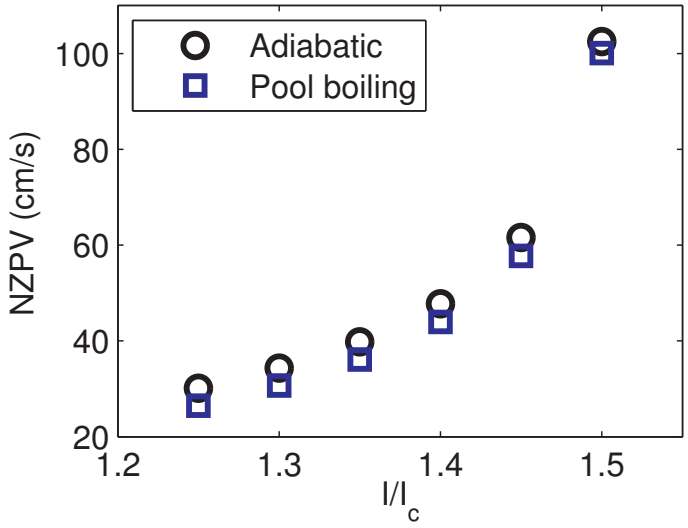

Figure 3.25: Effect of the heat transfer on the NZPV for different transport current.

To estimate the MQE, a perturbation is implemented in the model. In order to achieve this, the J_c drop presented before is replaced by an external field distribution decaying in time (left part of figure 3.26). The external field distribution (perturbation) creates an additional energy input to the already existent one coming from the transport current (I =1.25$I_c(T_{op})$). Here is the mathematical expression of the perturbation:

$$B(x,t) = B_0 \exp\big(-d_a(x-x_0)^2\big) flc1hs\left(t - \frac{t_{\max}}{4}, \frac{t_{\max}}{20}\right) \tag{3.3.3}$$

Where B_0 =200 mT, $flc1hs$ is a a smoothed Heaviside function defined in COMSOL [88], $t_{\max}$ the criterion time and d_a the width of the Gaussian distribution. The left part of figure 3.26 shows the temporal variation of the external field at the center of the tape ($x = x_0$). The right part depicts the evolution of the critical current as a function of the time. The criterion chosen to determine the MQE is the amount of energy needed to reduced the critical current density at the center of the tape to 0.1% of its initial value at $t = t_{\max}$. This energy is obtained by integrating the losses generated in the conductor during the perturbation. The energy generated without the perturbation is removed from the MQE calculation using the "non-perturbed" simulations. Note that, this method of determining the MQE is not equivalent to the formal MQE definition *i.e.* the Joule losses occurring over the time span are not equivalent to the enthalpy change resulting from an initial temperature profile (see page 36 for more details on the MQE definition). However, the simulations provides an estimation of the factors influencing the MQE.

Figure 3.27 shows the normalized MQE using the adiabatic simulation (1) as a reference case. From this figure, one can note that the effect of adding a resistive interface have negligible effect on the MQE. However, the low specific heat of sapphire substrate reduces the MQE drastically. Note that the heat transfer improves by 60% the quench energy of the superconductor which implies that it must be considered if the fault energy is in the range of the MQE.

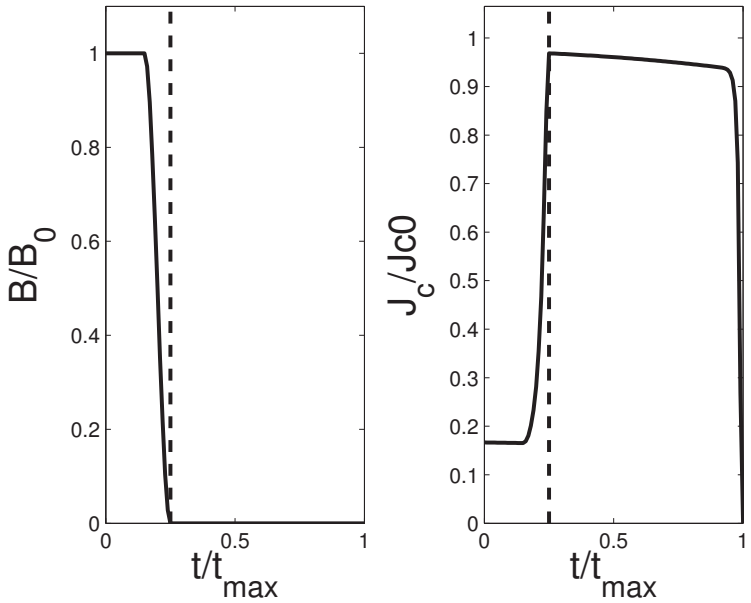

Figure 3.26: At the left, the temporal evolution of the perturbation (external field). The right figure shows the evolution of the critical current. After the perturbation (dashed-line) the critical current drops as a consequence of the heat generated during the perturbation. The drop at $t = t_{\max}$ is used to determine the MQE. J_{c0} is the current density at $T = T_{op}$ and $B = 0$.

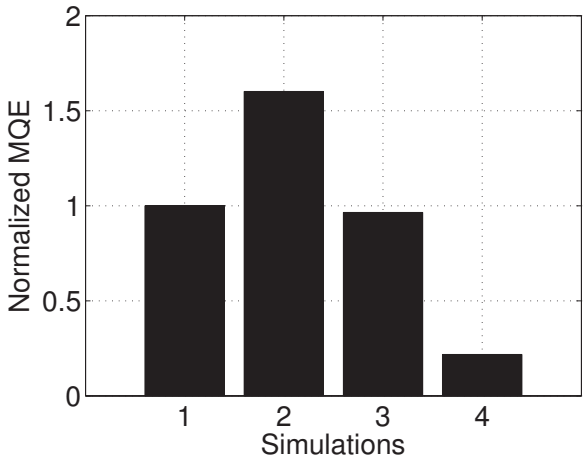

Figure 3.27: Minimum quench energy (MQE) normalized to the reference case (adiabatic). Simulation (1) shows the MQE for the adiabatic case, (2) for the pool boiling case, (3) for the adiabatic case with a increased interface resistance and (4) for the adiabatic case with a sapphire substrate replacing hastelloy. Those simulation are obtained with a transport current of $I = 1.25 I_c(T_{op})$. The calculated MQE for the adiabatic case is 2.3 mJ. This value is two order of magnitude larger than the one previously computed in Appendix C. This seems to originate from the heat absorbed by the substrate.

In summary, heat transfer (pool boiling) has negligible effect on the NZPV at the energy scale of the quench. Nevertheless, improving the heat transfer increases the stability of the conductor. The MQE is reduced for sapphire substrate as well as for interface layer of larger resistance.

Conclusion

A resistive SFCL must transits uniformly to avoid the problems inherent to the non-uniformities observed in HTS such as hot-spots and fault detection issues. Improving the normal zone propagation in coated conductors is crucial for the development of SFCL made of those conductors.

In the present work, experimental manipulations have shown that large transport currents ($I \gg I_c$) allow a fast resistive transition that occurs mainly as a consequence of the heat generation in the stabilizer (silver layer). In this case, the initial delay before the quench initiation is independent of the superconductor uniformity (localized external magnetic field). However, for transport currents in the range of the critical value the delay before the quench initiation is reduced with the non-uniformity (amplitude of the magnetic field).

Numerical simulations have been validated with experimental results. The relative error coming from the model is less than 10% for simulations presenting a non-negligible magnetic field background. From the experimental validation, it seems that the power-law is inaccurate to simulate the normal zone transition under low external magnetic field since the power-law exponent is increased with smaller fields. Nevertheless, the numerical simulations have shown that the propagation speed can be improved by three different methods:

- Using a thick thermally diffusive substrate.
- Adding a thin resistive interface between the HTS and stabilizer.
- Increasing the heat generation in the stabilizer.

Increasing heat generation in the stabilizer is obtained by increasing the stabilizer resistance or by reducing the critical current in the superconductor. Under these conditions, a tape behaves more like a normal metal since the current, that is rapidly diverted in the stabilizer, generates and diffuses heat faster in that layer than in the HTS. The side effect of that method is a reduction of the allowable time the tape can sustain the fault and an important temperature excursion once the tape has transited. The temperature excursion can be attenuated using a thicker substrate. Thicker substrates improve the "heat-sink property" of the layer but can also, under certain conditions, reduce the NZPV. For instance, for thickness larger than $\approx$100 μm, the hastelloy substrate thickness has no additional influence on the NZPV.

Using a thermally diffusive substrate such as sapphire improves the NZPV and the temperature uniformity along the conductor but also reduces the MQE as well as the allowable time the tape can sustain a fault if the thickness of the substrate is not thick enough. However, adding additional metallic clad such as copper would help to reduce the temperature excursion and also reduce the slope of the electrical field in the normal region (avoid voltage overshoot).

Finally, deliberately adding a thin resistive interface between the HTS and the stabilizer increases the CTL as well as the NZPV with a slight reduction of the MQE. This method is more promising than the others for improving the NZPV in coated conductors since the maximum temperature stays at a reasonable level for longer time than with the other methods.

Pool boiling seems to have negligible effect on the NZPV at the energy scale of the quench. Nevertheless, subcooled nitrogen has shown to increase the NZPV. It is difficult to estimate if this effect is coming from an over-estimation of the critical current or from the heat transfer. Improving the heat

transfer increases the stability of the conductor. A better understanding of the transient heat transfer mechanism and superconductor properties may enhanced the accuracy of the phenomenological equations as well as the design of SFCLs.

Appendix A. Materials Properties

Nitrogen (N_2)

Table A-I: Some physical parameters of Nitrogen

Molar mass	28.014 g/mol
Density (liquid)	809 kg/m^3 @ 101.3 kPa
Boiling Temperature	77.3 K @ 101.3 kPa
Triple point temperature/pressure (T_1)	63.14 K / 12.463 kPa)
Enthalpy of vaporization (Latent heat)	198.3 kJ/kg
Thermal conductivity	0.1338 W/m.K
Specific heat	2 000 J/kg.K

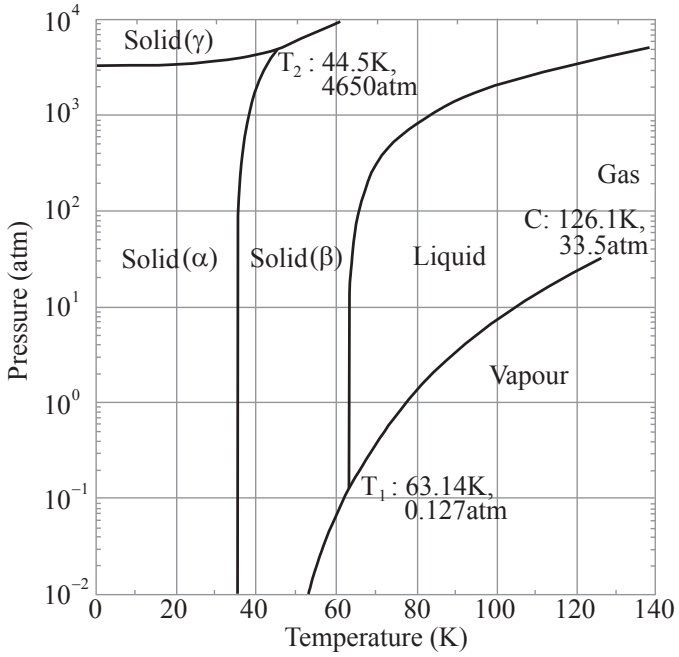

Figure A-1: Phase diagram (P-T) of nitrogen [89]. The normal melting and boiling points at 1 atm are about 63 K and 77 K respectively. C and T_1 denote the critical and liquid-vapour triple points.

Silver (Ag)

Table A-II: Some physical parameters of Silver.

Molar mass	107.8 g/mol
Crystal structure	face-centred cubic
Lattice parameters	a≈4 Å@ room temperature
Density	10 490 kg/m^3 @ room temperature

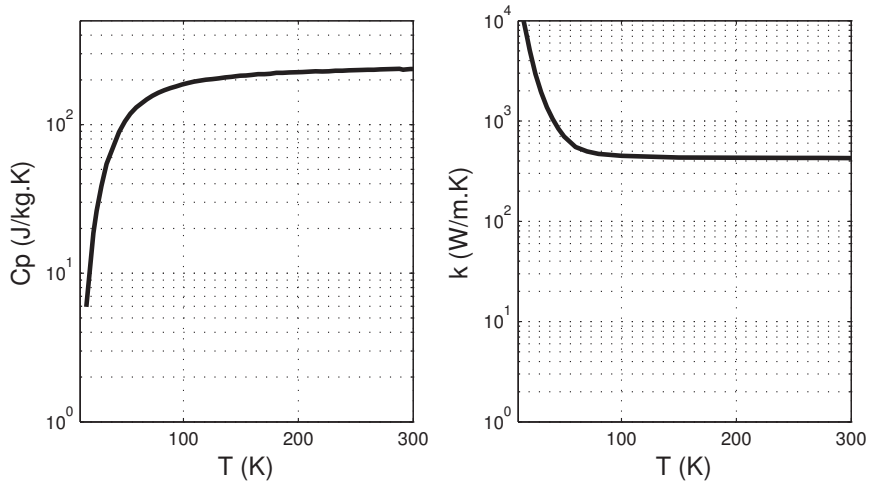

Figure A-2: Specific heat and thermal conductivity of silver as a function of temperature [90].

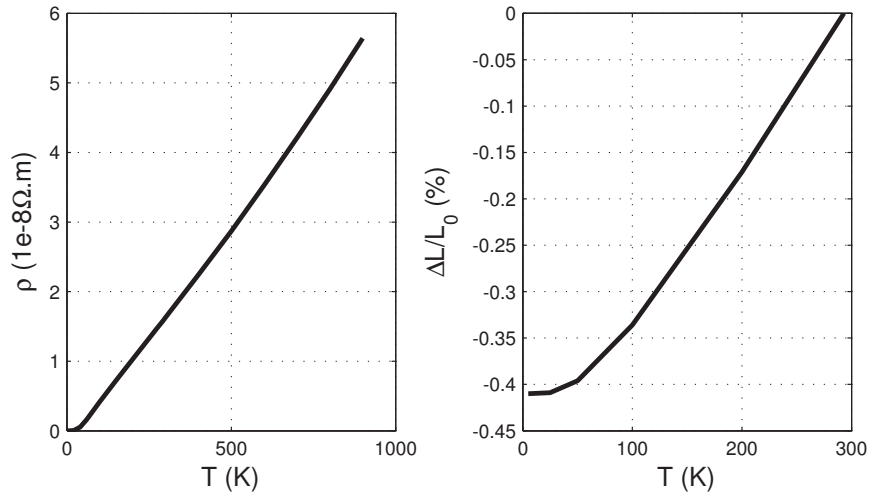

Figure A-3: Resistivity and linear thermal expansion of silver as a function of temperature [91, 90].

YBCO ($YBa_2Cu_3O_{7-x}$)

Table A-III: Some physical parameters of YBCO*.

% mass (approx)	Y: 13.34%, Ba: 41.23%, Cu: 28.62%, O: 16.81%
molar mass	666 g/mol
crystal structure	orthorombic (superconductor)
density	6 372 kg/m^3 @ room temperature
Lattice parameters	a=3.81 Å, b=3.88 Å, c=11.68 Å@ room temperature.
Tc	90-92 K, depends on x
coherence length @ 0 K	ab-plane: 1.64 nm c-plane: 0.3 nm
penetration depth @ 0 K	ab-plane: 149 nm c-plane: 600 nm
B_{c1}	ab-plane: 0.1-0.2 T, c-plane: 0.02 T
B_{irr}	9 T @ 86 K

* More data available in the following reference [21].

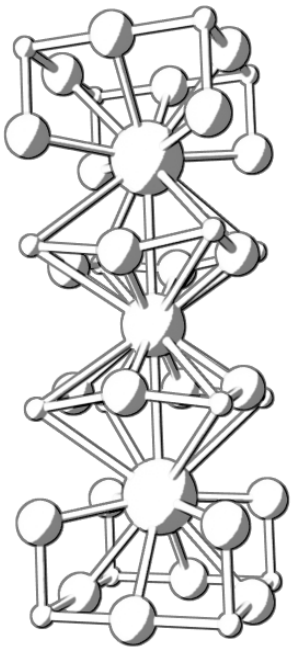

Figure A-4: An artistic view of the perovskite structure for YBCO [92] .The structure presents planes of copper oxide in the center (where the superconducting current flows). The role of yttrium is secondary and can be replaced by any rare earth element. Yttrium principally acts as spacers and contributors to charge carriers. A little more than two oxygen vacancies per unit cell are required for superconductivity.

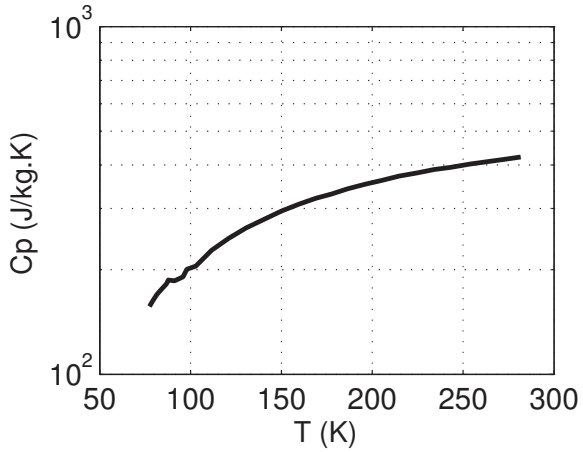

Figure A-5: Specific heat of YBCO as a function of temperature [93].

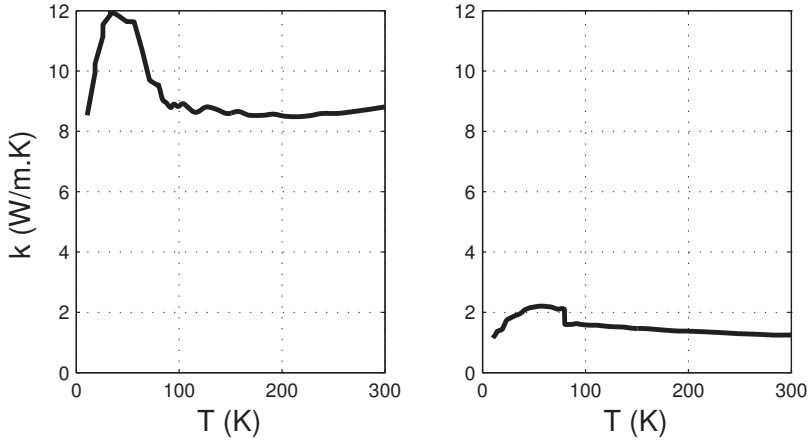

Figure A-6: Thermal conductivity along the ab plane (left) and the c plane (right) as a function of temperature [94].

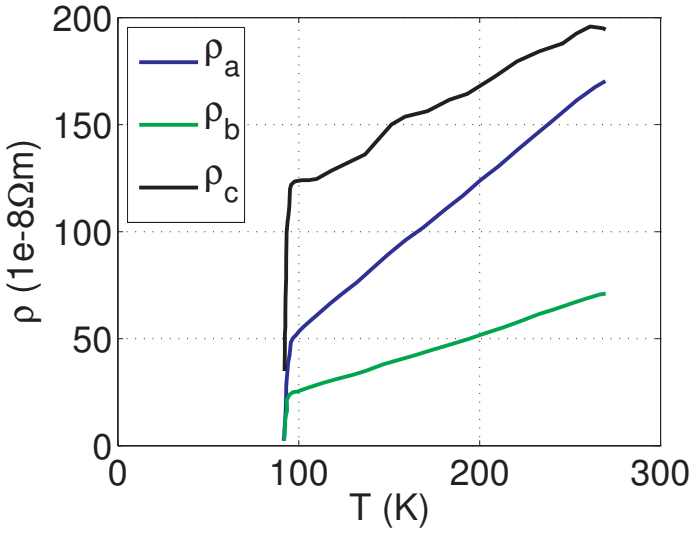

Figure A-7: Resistivity of YBCO along the a, b and c direction [95].

Magnesium Oxide (MgO)

Table A-IV: Some physical parameters of MgO*.

Composition (Weight %)	Mg:60.3% O:39.7%
Molar mass	40.3 g/mol
Crystal structure	cubic
Lattice parameters	a=4.212 Å@ room temperature
Density	3 580 kg/m^3 @ room temperature

* More data available in the following reference [96].

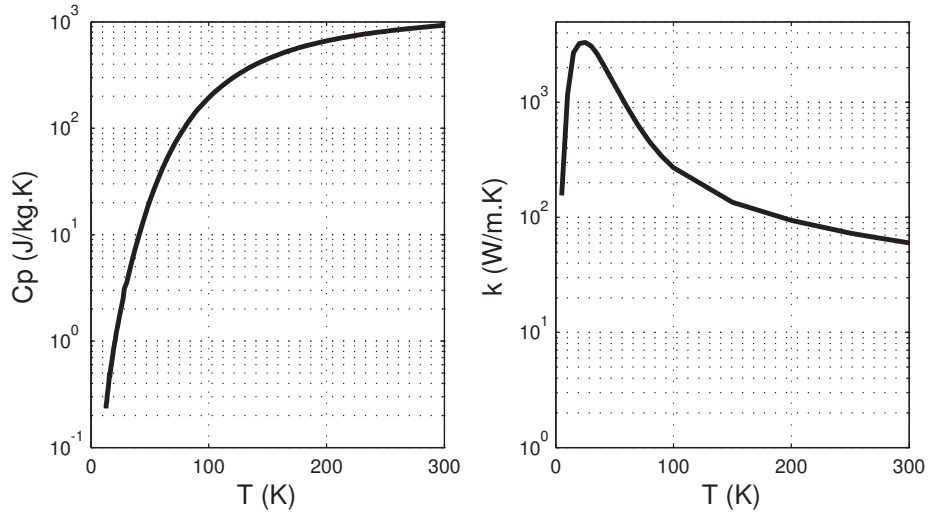

Figure A-8: Specific heat and thermal conductivity of Magnesium oxide (MgO) as a function of temperature [90].

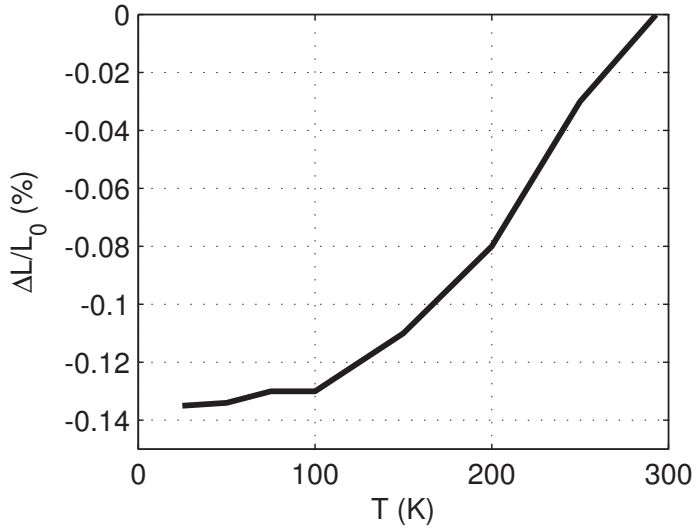

Figure A-9: Linear thermal expansion of Magnesium oxide (MgO) as a function of temperature [90].

Hastelloy® C-276™

Table A-V: Some physical parameters of Hastelloy C-276*.

Composition (Weight %)	Ni: 57, Co: 2, Cr: 16, Mo: 16, W: 4, Fe: 5, Others:
Crystal structure	face-centered-cubic
Lattice parameters	a=3.620 Å@ room temperature
Density	8 890 kg/m^3 @ room temperature

* More data available in the following references [97, 98].

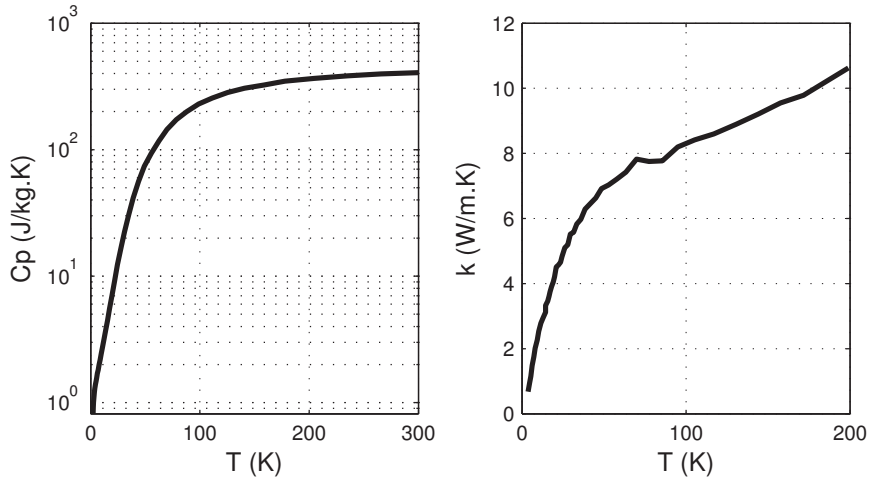

Figure A-10: Specific heat and thermal conductivity of Hastelloy C-276 as a function of temperature [98].

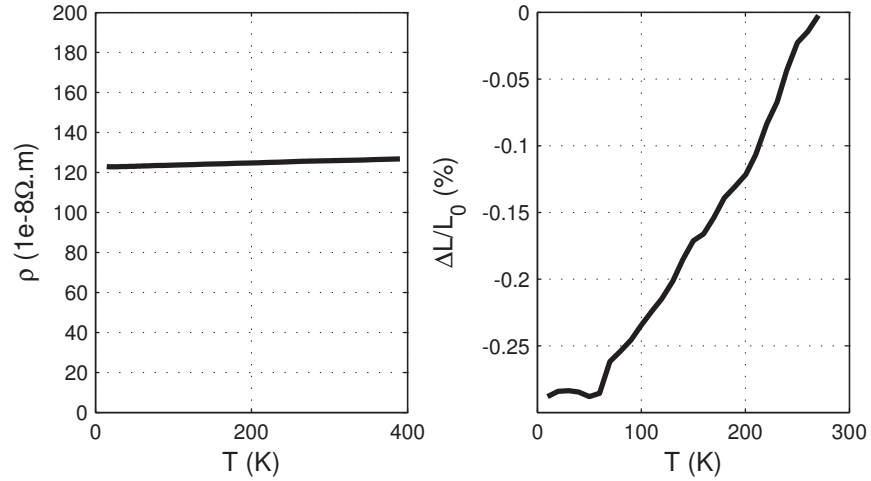

Figure A-11: Resistivity of Hastelloy C-276 as a function of temperature [98].

Sapphire (α-Al_2O_3)

Table A-VI: Some physical parameters of sapphire*.

Composition (Weight %)	Al:52.9250 O: 47.0750
Molar mass	101.9614 g/mol
Crystal structure	Rhombohedral
Lattice parameters	a≈4.8 Å, c≈13 Å@ room temperature
Density	4 000 kg/m^3 @ room temperature

* More data available in reference [99].

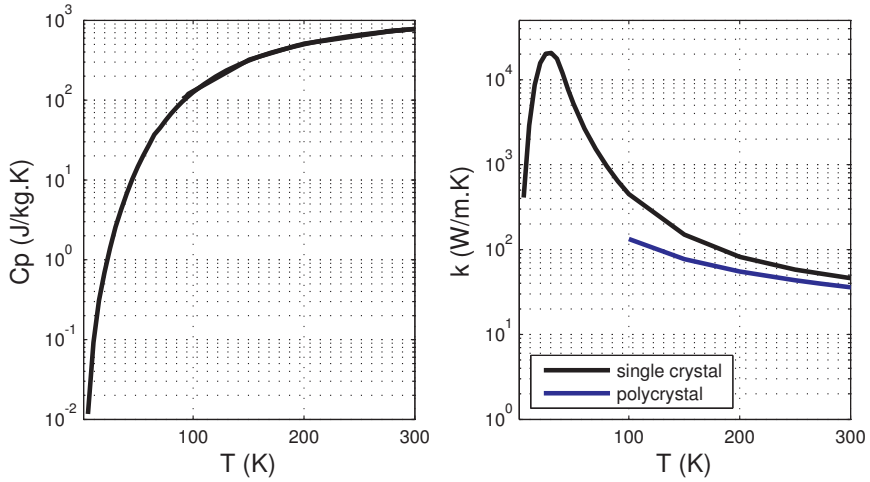

Figure A-12: Specific heat and thermal conductivity of sapphire (Al_2O_3) as a function of temperature [90].

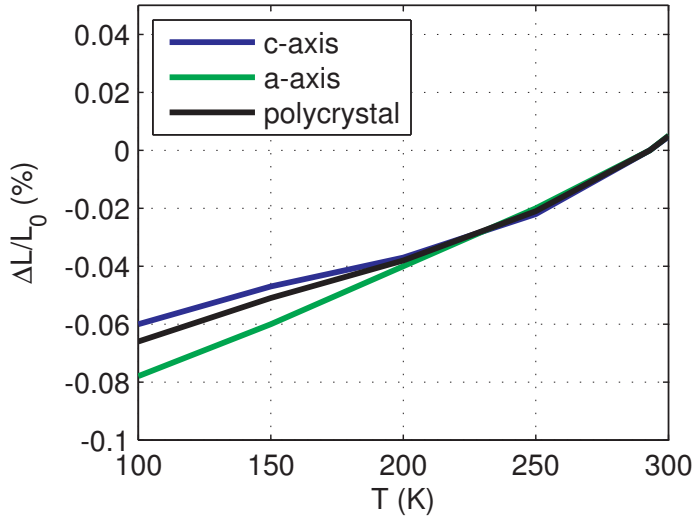

Figure A-13: Linear thermal expansion of sapphire (Al_2O_3) as a function of temperature [90].

Appendix B. Green's Function of the 3D Homogeneous Heat Equation

EQUATION 3.1.1 can be solved analytically under many circumstances. Let's consider the linear homogeneous case in 3D with constant parameters.

$$\frac{\partial T(\mathbf{x},t)}{\partial t} - D\nabla^2 T(\mathbf{x},t) = 0, \qquad \mathbf{x} = (x,y,z) \tag{B.1}$$

Using the assumption that eq. B.1 is linear and separable, the spatial solution of eq. B.1 can be represented in the wavenumber space using Fourier transform:

$$T(\mathbf{x},t) = \int_{\mathbb{R}^3} T_k(\mathbf{x},t) d\mathbf{k} \tag{B.2}$$

Where,

$$T_k(\mathbf{x},t) = \psi_k(t)\varphi(\mathbf{x}) = \psi_k(t)\exp\left(-i\mathbf{k}\cdot\mathbf{x}\right) \tag{B.3}$$

Substituting B.3 in B.1 yields to:

$$\frac{\partial \psi_k(t)}{\partial t} - D \parallel \mathbf{k} \parallel^2 \psi_k(t) = 0 \tag{B.4}$$

Which gives directly the solution for $\psi_k(t)$

$$\psi_k(t) = \psi_k(0)\exp\left(-D \parallel \mathbf{k} \parallel^2 t\right) \tag{B.5}$$

Substituting B.5 in B.2 leads to the following integral:

$$T(\mathbf{x},t) = \int_{\mathbb{R}^3} \psi_k(0)\exp\left(-D \parallel \mathbf{k} \parallel^2 t\right)\exp\left(-i\mathbf{k}\cdot\mathbf{x}\right) d\mathbf{k} \tag{B.6}$$

Using an initial condition, the function $\psi_k(0)$ can be determined. A custom approach would be to use the impulse distribution at the space position $\boldsymbol{\xi} = (\xi,\eta,\zeta)$ as the initial solution:

$$T(\mathbf{x},0) = \delta(\mathbf{x}-\boldsymbol{\xi})\delta(t-0), \qquad \boldsymbol{\xi} = (\xi,\eta,\zeta) \tag{B.7}$$

Substituting B.7 in B.6 and applying the inverse Fourier transform on both side of the equation:

$$\mathcal{F}^{-1}\Big(\delta(\mathbf{x}-\boldsymbol{\xi})\Big) = \mathcal{F}^{-1}\Big((2\pi)^3\psi_x(0)\Big) = (2\pi)^3\psi_k(0) \tag{B.8}$$

Hence,

$$\psi_k(0) = \frac{1}{(2\pi)^3}\int_{\mathbb{R}^3} \delta(\mathbf{x}-\boldsymbol{\xi})\exp\left(-i\mathbf{k}\cdot\mathbf{x}\right) d\mathbf{x} \tag{B.9}$$

At an infinite extent (Cauchy problem):

$$\psi_k(0) = \exp\left(-i\mathbf{k}\cdot\boldsymbol{\xi}\right) \tag{B.10}$$

Substituting B.10 in B.6 gives the Green's function of equation B.1 :

$$T(\mathbf{x},t) = \frac{1}{(2\pi)^3}\int_{\mathbb{R}^3} \exp\left(-D \parallel \mathbf{k} \parallel^2 t\right)\exp\left(-i\mathbf{k}\cdot(\mathbf{x}-\boldsymbol{\xi})\right)d\mathbf{k} = G(\mathbf{x},\boldsymbol{\xi},t) \tag{B.11}$$

Equation B.11 gives the evolution of the temperature from a single initial temperature point in space. This solution is of great interest since the evolution of the system under study can be found from any initial solution by convolution *i.e.*

$$T(\mathbf{x},t) = \int_{\mathbb{R}^3} G(\mathbf{x},\boldsymbol{\xi},t)T(\boldsymbol{\xi},0)d\boldsymbol{\xi} \tag{B.12}$$

One important result coming from the linear and separable heat equation is that diffusion happens in the same way independently in all the dimensions. For instance, rearranging B.11 yields to:

$$G(\mathbf{x},\boldsymbol{\xi},t) = \left(\frac{1}{(2\pi)}\int_{\mathbb{R}} \exp\left(-Dk^2t\right)\exp\left(-ik\lambda\right)dk\right)^3 \tag{B.13}$$

λ being the one dimensional distance from the initial temperature point located at $\boldsymbol{\xi} = (\xi,\eta,\zeta)$. Integrating B.13 over the whole domain i.e. $]-\infty,\infty[$ gives the fundamental solution of the 3D linear homogeneous heat equation.

$$G(\mathbf{x},\boldsymbol{\xi},t) = \frac{\exp\left(\dfrac{-\parallel \mathbf{x}-\boldsymbol{\xi} \parallel^2}{4Dt}\right)}{(4\pi Dt)^{3/2}} \tag{B.14}$$

Appendix C. Estimation of the Minimum Propagation Zone (MPZ)

THE minimum propagation zone can be roughly estimated using the steady-state heat balance. To do this the following assumptions are made.

a) The temperature is uniform along the width and thickness of the conductor.

b) The length of the conductor is much larger than its width which in turns is much larger than its thickness *i.e.* $L \gg w \gg d$.

c) The heat is generated by Joule losses only in the stabilizer (no current sharing) and is constant with the temperature *i.e.* $Q = \rho_{st} J_{st}^2$.

d) All the thermal parameters are taken independent of the temperature.

e) Heat transfer occurs only on one side of the conductor and only for the superconducting region ($T \leq T_c$).

f) The MPZ occurs in response to a perturbation which affect only the conductive region *i.e.* the superconductor and stabilizer. That means the substrate is not considered here.

g) The MPZ is symmetric.

The center of the MPZ is located at the position $x = 0$. For sake of simplification and by symmetry, only the positive x is considered –see figure C-1.

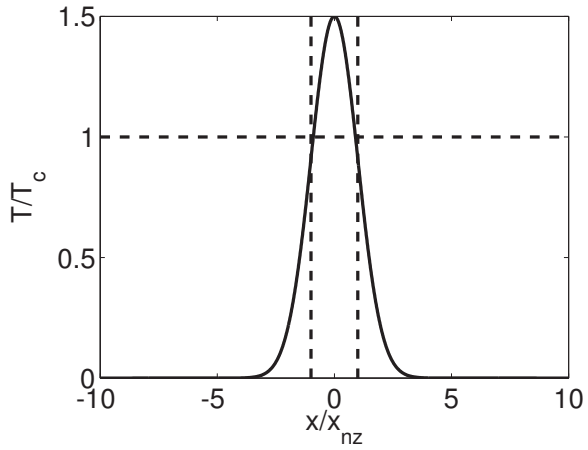

Figure C-1: A temperature profile defining the MPZ along the length of the conductor.

The 1D steady-state heat balance is expressed as:

$$k\frac{\partial^2 T_n(x)}{\partial x^2} + \rho J^2 = 0, \qquad |x| \leq x_{nz} \tag{C.1}$$
$$k\frac{\partial^2 T_s(x)}{\partial x^2} - \frac{S}{Ldw}h_c(T_s - T_{op}) = 0, \qquad |x| \geq x_{nz}$$

Where the exposed surface is $S \approx wL$ (only one side of the conductor is exposed to the coolant). Integrating the equation for the normal region gives directly:

$$\frac{\partial T_n(x)}{\partial x} = -\frac{\rho J^2}{k}x + C_1 \tag{C.2}$$

From symmetry, the temperature gradient of the MPZ is null at $x = 0$ – see figure C-1, meaning that C_1 must be zero. Integrating C.2 again yields to:

$$T_n(x) = -\frac{\rho J^2}{2k}x^2 + C_2 \tag{C.3}$$

At $x = x_{nz}$, $T_n(x) = T_c$. Using that condition in C.3 gives the solution for the normal region.

$$T_n(x) = T_c + \frac{\rho J^2}{2k}(x_{nz}^2 - x^2) \tag{C.4}$$

Using $\Theta = T_s - T_{op}$, the equation for the superconducting region can be rearranged as:

$$k\frac{\partial^2 \Theta(x)}{\partial x^2} - \frac{1}{d}h_c\Theta = 0, \qquad \frac{\partial^2 T}{dx^2} = \frac{\partial^2 \Theta}{dx^2} \tag{C.5}$$

Trying a solution of the form $\Theta(x) = \Theta_0 \exp(\Gamma x)$ and substituting it in C.5 one can easily find the following characteristic equation:

$$\Gamma^2 - \frac{1}{d}h_c = 0 \tag{C.6}$$

There is two solution for C.6, $\Gamma \pm \sqrt{h_c/d}$. Using the definition of the MPZ i.e. $\Theta(\pm\infty) = 0$, Γ can only be negative. Thus:

$$\Theta(x) = \Theta_0 \exp(-\Gamma x) \tag{C.7}$$

Using the boundary condition $T_s = T_c$ at $x = x_{nz}$, and substituting $\Theta = T_s - T_{op}$ in C.7, one get the solution for the profile in the superconductive region.

$$T_s(x) = T_{op} + (T_c - T_{op}) \exp\big(-\Gamma(x_{nz} - x)\big) \tag{C.8}$$

Finally, one can defines the size of the normal zone x_{nz} using the continuity of the temperature gradient at the boundary of the regions.

$$\frac{\partial T_n}{\partial x} = \frac{\partial T_s}{\partial x}, \qquad \text{at } x = x_{nz} \tag{C.9}$$
$$\frac{\rho J^2 x_{nz}}{k} = (T_c - T_{op})\left(\frac{h_c}{d}\right)^{1/2}$$

Thus,

$$x_{nz} = \left(\frac{T_c - T_{op}}{\rho J^2}\right)\left(\frac{h_c k}{d}\right)^{1/2} \tag{C.10}$$

Substituting effective values in C.10 e.g. h_c =2000 Wm^{-2}, $k \approx \frac{2}{3}445 + \frac{1}{3}10$ =300 W/m.K, d =3μm, $(T_c - T_{op})$ =13 K, $\rho = 1 \times 10^{-9}$ Ω.m and $J = 1.25 \times 10^{10}$ Am^{-2} gives values of $2x_{nz}$ in the range of ≈75 μm and maximum temperature $T(0)$ in the range of $T_c + 1.5$ K.

Here is some remarks about the preceding assumptions:

- Concerning a), modeling coated conductors as a 1D geometry is not appropriate, at least neglecting the tape width does not agreed with the MPZ profile which drops symmetrically of 63% of its central temperature at distance $x = 1/\Gamma \approx 40\mu$m.
- Concerning b), usual coated conductors samples have $L >$50 mm $\gg w =$4-12 mm $\gg d =$50-100μm.
- Concerning c), this assumptions and is not validated since the flux-flow resistance in the range $(T_c - T_{op})$ may be significant. For instance – see figure 2.6.
- Concerning d), this assumption is more or less true, for the thermal diffusivity k and electrical resistivity ρ – see Appendix A. Considering the temperature range of the MPZ, the convective heat transfer is somewhere in between the free-convection and nucleate boiling regime. This can change the value of x_{nz} from a factor 4. Nevertheless, the size of the MPZ is so small that we can expect this assumption verified.
- Concerning e). This is true since the substrate isolates the other side of the tape from the coolant. Especially if the substrate have a low thermal diffusivity e.g. Hastelloy.
- Concerning f). The substrate acts as a thermal sink. Neglecting its influence underestimate the MPZ range and size.

Appendix D. Estimation of the Normal Zone Propagation Velocity (NZPV)

USING the 1D travelling wave representation, the NZPV can be estimated under the following assumptions. Some of them have already been treated in Appendix C, they are reminded here for sake of completeness:

a) The temperature is uniform along the width and thickness of the conductor.

b) The length of the conductor is much larger than its width which in turns is much larger than its thickness *i.e.* $L \gg w \gg d$.

c) The heat is generated by Joule losses only in the stabilizer (no current sharing) and is constant with the temperature *i.e.* $Q = \rho_{st} J_{st}^2$.

d) All the thermal parameters are taken independent of the temperature.

e) The temperature front can be regarded as a travelling wave, for this example moving along the positive direction.

f) The temperature far away from the superconducting-normal tends to becomes constant. At one hand is $T(\infty) = T_{op}$ at the other is $T(-\infty) = T_{max}$ which is the equilibrium temperature for which heat generation balance heat transfer with the surrounding. For instance see figure D-1.

g) The temperature gradient is continuous at the interface.

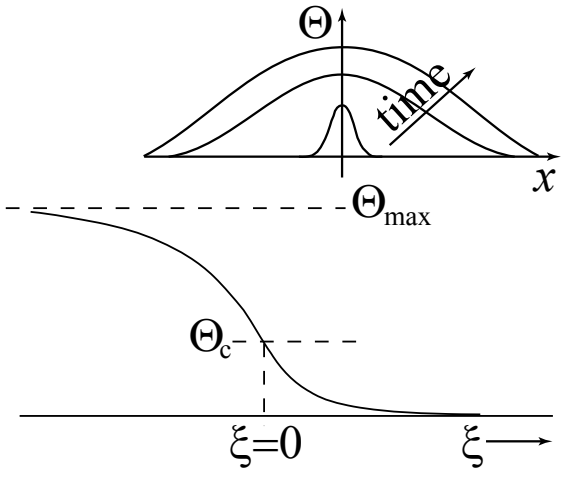

Figure D-1: At the top, time evolution of the temperature profile. At the bottom, the travelling wave representation. The normal-superconducting interface is located at $\xi = 0$.

From the 1D heat balance equation, $S \approx wL$:

$$k\frac{\partial^2 T}{\partial x^2} + \rho_m C_p \frac{\partial T}{\partial t} - \frac{h_c}{d}(T - T_{op}) - Q = 0 \tag{D.1}$$

Where, d is the thickness of the tape, k, ρ_m and C_p the thermal conductivity, mass density and specific heat of the material, h_c the convective heat transfer and Q the Joule losses. With the reduced temperature $\Theta = (T - T_{op})$ and the travelling wave representation *i.e.* $\xi = x - vt$ (the direction of the wave is arbitrary if the boundary conditions are well posed), equation D.1 becomes:

$$\frac{\partial^2 \Theta}{\partial \xi^2} + Av\frac{\partial \Theta}{\partial \xi} - B\Theta - Q = 0 \tag{D.2}$$

Where $A = \rho_m C_p/k$, and $B = h_c/kd$. Each region of the conductor is defined as:

$$\frac{\partial^2 \Theta_s}{\partial \xi^2} + Av\frac{\partial \Theta_s}{\partial \xi} - B\Theta_s = 0, \quad \text{Superconducting zone } (\xi > 0) \tag{D.3}$$

$$\frac{\partial^2 \Theta_n}{\partial \xi^2} + Av\frac{\partial \Theta_n}{\partial \xi} - B\Theta_n - Q = 0, \quad \text{Normal zone } (\xi < 0) \tag{D.4}$$

Solving the heat balance for the homogeneous case *i.e.* equation D.3 gives directly the following characteristic equation (a solution of the form $\Theta(\xi) = \Theta_0 \exp(\Gamma\xi)$):

$$\Gamma_1 = -\frac{1}{2}\left(Av - \left((Av)^2 + 4B\right)^{1/2}\right) \tag{D.5}$$

$$\Gamma_2 = -\frac{1}{2}\left(Av + \left((Av)^2 + 4B\right)^{1/2}\right) \tag{D.6}$$

Inserting the roots given by D.5 and D.6 into the argument of the exponentials gives the homogeneous solution:

$$\Theta_H(\xi) = C_1 \exp(\Gamma_1 \xi) + C_2 \exp(\Gamma_2 \xi) \tag{D.7}$$

In the superconducting region, $\Theta \to 0$ as $\xi \to \infty$, The solution of the 1D heat balance in the superconducting ($\xi > 0$) part is obtained posing $C_1 = 0$ since Γ_1 is always positive (A and B are real positive values). Thus,

$$\Theta_s(\xi) = C_2 \exp(\Gamma_2 \xi), \qquad \text{Superconducting region } (\xi > 0) \tag{D.8}$$

Using the homogeneous solution D.7, one can look at a particular solution of equation D.4. Using the undetermined coefficient method. One can seek a constant solution (Q is constant) of the form

$$\Theta_p = C_3 \tag{D.9}$$

Then, replacing Θ_p into D.4 gives:

$$C_3 = \frac{Q}{B} \tag{D.10}$$

The solution in the normal region is obtained by superposition *i.e.* $\Theta_n(\xi) = \Theta_H + \Theta_p$. With the proper boundary condition $\Theta \to \Theta_{max} = Q/B$ as $\xi \to -\infty$, one can get

$$\Theta_n(\xi) = C_1 \exp(\Gamma_1 \xi) + \frac{Q}{B}, \qquad \text{Normal region } (\xi < 0) \tag{D.11}$$

Considering that $\Theta = \Theta_c$ at $\xi = 0$ and that the temperature gradient is continuous at the same position leads to:

$$C_1 + \frac{Q}{B} = C_2 = \Theta_c \tag{D.12}$$

$$\Gamma_2 \Theta_c = \Gamma_1 \Big(\Theta_c - \Theta_{max} \Big) \tag{D.13}$$

The NZPV under heat transfer can be obtained by simplifying D.13 :

$$\begin{aligned}
\Big(Av - \Big(A^2 v^2 + 4B \Big)^{1/2} \Big) \Theta_c &= \Big(Av + \Big(A^2 v^2 + 4B \Big)^{1/2} \Big) \Big(\Theta_c - \Theta_{max} \Big) \\
2\Theta_c \Big(A^2 v^2 + 4B \Big)^{1/2} &= \Theta_{max} \Big(Av + \Big(A^2 v^2 + 4B \Big)^{1/2} \Big) \\
-Av\Theta_{max} &= \Big(\Theta_{max} - 2\Theta_c \Big) \Big(A^2 v^2 + 4B \Big)^{1/2} \\
A^2 v^2 \Theta_{max}^2 &= \Big(\Theta_{max} - 2\Theta_c \Big)^2 \Big(A^2 v^2 + 4B \Big) \\
\Theta_{max}^2 &= \Big(\Theta_{max}^2 - 4\Theta_c \Theta_{max} + 4\Theta_c^2 \Big) \Big(1 + \frac{4B}{A^2 v^2} \Big) \\
\Big(\Theta_c (\Theta_{max} - \Theta_c) \Big) &= \frac{B}{A^2 v^2} \Big(\Theta_{max}^2 - 4\Theta_c \Theta_{max} + 4\Theta_c^2 \Big) \\
\Big(\Theta_c (\Theta_{max} - \Theta_c) \Big) &= \frac{B}{A^2 v^2} (\Theta_{max} - 2\Theta_c)^2 \\
v &= \frac{B^{1/2}}{A} (\Theta_{max} - 2\Theta_c) \Big(\Theta_c (\Theta_{max} - \Theta_c) \Big)^{-1/2}
\end{aligned} \tag{D.14}$$

Substituting the values of A and B:

$$v = \frac{\big(h_c k/d \big)^{1/2}}{\rho_m C_p} (\Theta_{max} - 2\Theta_c) \Big(\Theta_c (\Theta_{max} - \Theta_c) \Big)^{-1/2} \tag{D.15}$$

Which gives the following temperature profiles:

$$\Theta_s(\xi) = \Theta_c \exp(\Gamma_2 \xi), \qquad \text{Superconducting region } (\xi > 0) \tag{D.16}$$

$$\Theta_n(\xi) = \Theta_{max} + (\Theta_c - \Theta_{max}) \exp(\Gamma_1 \xi), \qquad \text{Normal region } (\xi < 0) \tag{D.17}$$

The adiabatic NZPV is somewhat more complicated to establish since the temperature at $\xi = -\infty$ is infinite [73]. An estimate of the adiabatic NZPV can be obtained considering a linear temperature profile in the normal region nearby $\xi = 0$ [75, 100]. Using this assumption, as well as D.3 and D.4, one gets the following equations:

$$\frac{\partial^2 \Theta_s}{\partial \xi^2} + Av \frac{\partial \Theta_s}{\partial \xi} = 0, \quad \text{Superconducting region } (\xi > 0) \tag{D.18}$$

$$\rho_m C_p v \frac{\partial \Theta_n}{\partial \xi} + Q = 0, \quad \text{Normal region } (\xi < 0) \tag{D.19}$$

The solution in the superconducting region is obtained directly,

$$\Theta_s(\xi) = C_4 \exp\big(-Av\xi \big), \qquad \text{Superconducting region } (\xi > 0) \tag{D.20}$$

At the interface ($\xi = 0$), Θ and $k\nabla\Theta$ are continuous. Thus

$$\Theta_n(\xi) = \Theta_s(\xi) = \Theta_c \tag{D.21}$$

$$k\frac{\partial\Theta_s}{\partial\xi} = k\frac{\partial\Theta_n}{\partial\xi} \tag{D.22}$$

Substituting D.20 in D.21 gives,

$$\Theta_s(\xi) = \Theta_c \exp\big(-Av\xi\big) \tag{D.23}$$

Substituting D.23 in D.22 gives,

$$\rho_m C_p v\Theta_c = \frac{Qk}{\rho_m C_p v}$$

$$v^2 = \frac{Qk}{\Theta_c \rho_m^2 C_p^2}$$

$$v = \frac{J}{\rho_m C_p}\left(\frac{\rho k}{T_c - T_{op}}\right)^{1/2} \tag{D.25}$$

Bibliography

[1] Energy Information Administration, Office of Integrated Analysis and Forecasting. International energy outlook 2009. U.S. Department of Energy Washington, DC : DOE/EIA-0484(2009), 2009. [Online]. http://www.eia.doe.gov/oiaf/ieo/index.html.

[2] Electric Power Research Institute (EPRI). Increased power flow guidebook: Increasing power flow on transmission and substation circuits. EPRI, Palo Alto, CA : 1010627, 2005. [Online]. http://my.epri.com.

[3] Electric Power Research Institute (EPRI). Advanced DER compliant distribution circuits for high reliability-2006 update. EPRI, Palo Alto, CA : 1012771, 2006. [Online]. http://my.epri.com.

[4] Electric Power Research Institute (EPRI). Fault current management guidebook-updated. EPRI, Palo Alto, CA : 1012419, 2006. [Online]. http://my.epri.com.

[5] M. Noe and M. Steurer. High-temperature superconductor fault current limiters: concepts, applications, and development status. *Superconductor science and technology*, 20:R15, 2007. DOI: 10.1088/0953-2048/20/3/R01.

[6] International Council On Large Electric Systems (CIGRE) Working Group A3.10. Fault current limiters in electrical medium and high voltage systems. CIGRE Technical brochure no. 239, 2003. [Online]. http://www.e-cigre.org.

[7] Electric Power Research Institute (EPRI). Survey of fault current limiter (FCL) technologies-update. EPRI, Palo Alto, CA : 1016389, 2008. [Online]. http://my.epri.com.

[8] U.S. Department of Energy. Doe provides up to $51.8 million to modernize the u.s. electric grid system. [Online], June 27, 2007. http://www.netl.doe.gov/publications/press/2007/5180.html.

[9] High Temperature Superconductivity Program Peer Review. Alexandria, VA, August 4-6, 2009. [Online]. http://www.htspeerreview.com/agenda.html.

[10] M. Tinkham. *Introduction to superconductivity*. Dover Publications inc., Mineola, N.Y., 2nd edition, 2004.

[11] Superconductor.org. Type 1 superconductors and a periodic chart comparison. [Online]. http://www.superconductors.org/.

[12] A.C. Rose-Innes and E.H. Rhoderick. *Introduction to superconductivity*. International series in solid state physics, vol. 6. Pergamon Press, Oxford, U.K., 1978.

[13] C. Kittel. *Introduction to solid state physics*. John Wiley & Sons, Ney-York, N.Y., 7th edition, 1996.

[14] M.R. Eskildsen, M. Kugler, S. Tanaka, J. Jun, S.M. Kazakov, J. Karpinski, and Ø Fischer. Vortex imaging in the π band of magnesium diboride. *Physical Review Letters*, 89(18):187003, 2002. DOI: 10.1103/PhysRevLett.89.187003.

[15] J.G. Bednorz and K.A. Müller. Possible high T_c superconductivity in the Ba-La-Cu-0 system. *Zeitschrift für Physik B Condensed Matter*, 64(2):189, 1986. DOI: 10.1007/BF01303701.

[16] Superconductivity Present and Future Applications. Coalition for the Commercial Application of Superconductors (CCAS). [Online], 2008. http://www.ccas-web.org/pdf/ccas_brochure_web.pdf.

[17] J.W. Ekin. *Experimental Techniques for low-temperature measurements: Cryostat Design, Material Properties, and Superconductor Critical-Current testing*. Oxford University Press Inc., New-York, N.Y., 2006.

[18] D. Larbalestier, A. Gurevich, D.M. Feldmann, and A. Polyanskii. High-T_c superconducting materials for electric power applications. *Nature*, 414:368, 2001. DOI: 10.1038/35104654.

[19] W.V. Hassenzahl, D.W. Hazelton, B.K. Johnson, P. Komarek, M. Noe, and C.T. Reis. Electric power applications of superconductivity. *Proceedings of the IEEE*, 92(10):1655, 2004. DOI: 10.1109/JPROC.2004.833674.

[20] J. Wang, Y. Bugoslavsky, A. Berenov, L. Cowey, A.D. Caplin, L.F. Cohen, J.L. MacManus Driscoll, L.D. Cooley, X. Song, and D.C. Larbalestier. High critical current density and improved irreversibility field in bulk MgB_2 made by a scalable, nanoparticle addition route. *Applied Physics Letters*, 81(11):2026, 2002. DOI: 10.1063/1.1506184.

[21] NIST Ceramics WebBook. [Online]. http://www.ceramics.nist.gov/srd/hts/htsquery.htm.

[22] LHC-The Large Hadron Collider. [Online]. http://lhc-machine-outreach.web.cern.ch/lhc-machine-outreach/components/magnets.htm.

[23] ITER-the way to new energy. [Online]. http://www.iter.org/mach/Pages/Magnets.aspx.

[24] G. Blatter, M.V. Feigel'man, V.B. Geshkenbein, A.I. Larkin, and V.M. Vinokur. Vortices in high-temperature superconductors. *Reviews of Modern Physics*, 66(4):1125, 1994. DOI: 10.1103/RevModPhys.66.1125.

[25] T. Sheanhen. *Introduction to high-temperature superconductivity*. Selected topics in superconductivity. Plenum Press, Ney-York, N.Y., 1994.

[26] Y. Yeshurun, A.P. Malozemoff, and A. Shaulov. Magnetic relaxation in high-temperature superconductors. *Reviews of Modern Physics*, 68(3):911, 1996. DOI: 10.1103/RevModPhys.68.911.

[27] M.N. Kunchur. Current-induced pair breaking in magnesium diboride. *Journal of Physics: Condensed matter*, 16(39):R1183, 2004. DOI: 10.1088/0953-8984/16/39/R01.

[28] P.L. Gammel, L.F. Schneemeyer, and D.J. Bishop. Squid picovoltometry of $YBa_2Cu_3O_7$ single crystals: Evidence for a finite-temperature phase transition in the high-field vortex state. *Physical Review Letters*, 66(7):953, 1991. DOI: 10.1103/PhysRevLett.66.953.

[29] T. Haugan, P.N. Barnes, R. Wheeler, F. Meisenkothen, and M. Sumption. Addition of nanoparticle dispersions to enhance flux pinning of the $yba_2cu_3o_{7-x}$ superconductor. *Nature*, 430:867, 2004. DOI: 10.1038/nature02792.

[30] M. Prester. Current transfer and initial dissipation in high-T_c superconductors. *Superconductor Science and Technology*, 11(4):333, 1998. DOI: 10.1088/0953-2048/11/4/002.

[31] I. Aranson, A. Gurevich, and V. Vinokur. Vortex avalanches and magnetic flux fragmentation in superconductors. *Physical Review Letters*, 87(6):067003, 2001. DOI: 10.1103/PhysRevLett.87.067003.

[32] K. Heine, J. Tenbrink, and M. Thöner. High-field critical current densities in $Bi_2Sr_2Ca_1Cu_2O_{8+x}$/Ag wires. *Applied Physics Letters*, 55:2441, 1989. DOI: 10.1063/1.102295.

[33] R.D. Blaugher, R.N. Bhattacharya, and J. Chen. Bi-2212: an HTS coated conductor. *IEEE Transactions on Applied Superconductivity*, 13(2):2496, 2003. DOI: 10.1109/TASC.2003.811830.

[34] M. K. Wu, J. R. Ashburn, C. J. Torng, P. H. Hor, R. L. Meng, L. Gao, Z. J. Huang, Y. Q. Wang, and C. W. Chu. Superconductivity at 93 K in a new mixed-phase Y-Ba-Cu-O compound system at ambient pressure. *Phys. Rev. Lett.*, 58(9):908–910, 1987. DOI: 10.1103/PhysRevLett.58.908.

[35] Y. Iijima, N. Tanabe, O. Kohno, and Y. Ikeno. In-plane aligned $YBa_2Cu_3O_{7x}$ thin films deposited on polycrystalline metallic substrates. *Applied Physics Letters*, 60:769, 1992. DOI: 10.1063/1.106514.

[36] X. D. Wu, S.R. Foltyn, P.N. Arendt, W.R. Blumenthal, I.H. Campbell, J.D. Cotton, J.Y. Coulter, W.L. Hults, M.P. Maley, H.F. Safar, and J.L. Smith. Properties of $YBa_2Cu_3O_7$ thick films on flexible buffered metallic substrates. *Applied Physics Letters*, 67:2397, 1995. DOI: 10.1063/1.114559.

[37] A. Goyal, D.P. Norton, J.D. Budai, M. Paranthaman, E.D. Specht, D.M. Kroeger, D.K. Christen, Q. He, B. Saffian, F.A. List, D.F. Lee, P.M. Martin, C.E. Klabunde, E. Hartfield, and V.K. Sikka. High critical current density superconducting tapes by epitaxial deposition of $YBa_2Cu_3O_x$ thick films on biaxially textured metals. *Applied Physics Letters*, 69:1795, 1996. DOI: 10.1063/1.117489.

[38] C. Cantoni and A. Goyal. *High-T_c superconducting thin- and tick-film based coated conductors for energy applications*. Thin-film metal-oxides: fundamentals and applications in electronics and energy. Springer, Ney-York, N.Y., 2010. DOI: 10.1007/978-1-4419-0664-9_7.

[39] National High Magnetic Field Laboratory. A comparison of superconductor critical currents. [Online]. http://www.magnet.fsu.edu/magnettechnology/research/asc/plots.html.

[40] J.H. Durrell and N.A. Rutter. Importance of low-angle grain boundaries in $YBa_2Cu_3O_{7-\delta}$ coated conductors. *Superconductor Science and Technology*, 22:013001, 2009. DOI: 10.1088/0953-2048/22/1/013001.

[41] SUPERPOWER.INC. [Online]. http://www.superpower-inc.com.

[42] AMERICAN SUPERCONDUCTOR.CORP. [Online]. http://www.amsc.com.

[43] J.R. Groves, P.N. Arendt, H. Kung, S.R. Foltyn, R.F. DePaula, and L.A. Emmert. Texture development in IBAD MgO films as a function of deposition thickness and rate. *IEEE Transaction on Applied Superconductivity*, 11(1):2822, 2001. DOI: 10.1109/77.919650.

[44] International Council On Large Electric Systems (CIGRE) Working Group A3.16. Guideline on the impacts of fault current limiting devices on protection system. CIGRE Technical brochure no. 339, 2008. [Online]. http://www.e-cigre.org.

[45] S.S. Kalsi and A. Malozemoff. HTS fault current limiter concept. *IEEE Power Engineering Society General Meeting*, 2:1426, 2004. DOI: 10.1109/PES.2004.1373103.

[46] AE TECHRON.INC. [Online]. http://www.aetechron.com/index.html.

[47] NATIONAL INSTRUMENTS™. [Online]. http://www.ni.com.

[48] R. Grabovickic, J.W. Lue, M.J. Gouge, J.A. Demko, and R.C. Duckworth. Measurements of temperature dependence of the stability and quench propagation of a 20-cm-long RABiTS Y-Ba-Cu-O tape. *IEEE Transaction on Applied Superconductivity*, 13(2):1726, 2003. DOI: 10.1109/TASC.2003.812874.

[49] L. Antognazza, M. Therasse, M. Decroux, F. Roy, B. utoit, M. Abplanalp, and ø. Fisher. Comparison between the behavior of hts thin film grown on sapphire and coated conductors for fault current limiter applications. *IEEE Transactions on Applied Superconductivity*, 19(3): 1960, 2009. DOI: 10.1109/TASC.2009.2018113.

[50] X. Wang, U.P. Trociewitz, and J. Schwartz. Self-field quench behaviour of $YBa_2Cu_3O_{7\delta}$ coated conductors with different stabilizers. *Superconductor Science and Technology*, 22(8): 085005, 2009. DOI: 10.1088/0953-2048/22/8/085005.

[51] Y.G. Zhou, G.M. Zhang, X.H. Li, Y.S. Wang, L.Z. Lin, and L.Y. Xiao. Performance of $YBa_2Cu_3O_x$tapes with different structures under AC overcurrent conditions. *IEEE Transactions on Applied Superconductivity*, 19(4):3665, 2009. DOI: 10.1109/TASC.2009.2019627.

[52] X. Wang, U.P. Trociewitz, and J. Schwartz. Near-adiabatic quench experiments on short $YBa_2Cu_3O_{7\delta}$ coated conductors. *Journal of Applied Physics*, 101(5):053904, 2007. DOI: 10.1063/1.2435804.

[53] A. Sakurai, M. Shiotsu, and K. Hata. Boiling heat transfer characteristics for heat inputs with various increasing rates in liquid nitrogen. *Cryogenics*, 32(5):421, 1992. DOI: 10.1016/0011-2275(92)90069-M.

[54] P. Tixador, Y. Cointe, T. Nguyen, and C. Villard. Electrothermal phenomena about current limitation with coated conductors. *IEEE Transactions on Applied Superconductivity*, 19(3): 1938, 2009. DOI: 10.1109/TASC.2009.2018512.

[55] K. Yamafuji and T. Kiss. A new interpretation of the glass-liquid transition of pinned fluxoids in high-T_c superconductors. *Physica C*, 258(3-4):187, 1996. DOI: 10.1016/0921-4534(95)00803-9.

[56] B. Zeimetz, B.A. Glowacki, and J.E. Evetts. Application of percolation theory to current transfer in granular superconductors. *Europen Physical Journal B*, 29:359, 2002. DOI: 10.1140/epjb/e2002-00275-9.

[57] A.M. Campbell. A new method of determining the critical state in superconductors. *Superconductor science and technology*, 20:292, 2007. DOI: 10.1088/0953-2048/20/3/031.

[58] R. Brambilla, F. Grilli, L. Martini, and F. Sirois. Integral equations for the current density in thin conductors and their solution by the finite-element method. *Superconductor Science and Technology*, 21:105008, 2008. DOI: 10.1088/0953-2048/21/10/105008.

[59] M. Friesen and A. Gurevich. Nonlinear current flow in superconductors with restricted geometries. *Physical Review B*, 63:064521, 2001. DOI: 10.1103/PhysRevB.63.064521.

[60] Y. Mawatari and J.R. lem. Analytical model of the response of a superconducting film to line currents. *Physical Review B*, 74:144523, 2006. DOI: 10.1103/PhysRevB.74.144523.

[61] K.J. Binns, P.J. Lawrenson, and C.W. Towbridge. *The analytical and numerical solution of electric and magnetic fields*. John Wiley & Sons Ltd., Chichester, U.K., 1992.

[62] J.W. Ekin. Current transfer in multifilamentary superconductors. I. Theory. *Journal of Applied Physics*, 49(6):3406, 1978. DOI: 10.1063/1.325245.

[63] A. Stenvall, A. Korpela, J. Lehtonen, and R. Mikkonen. Current transfer length revisited. *Superconductor Science and Technology*, 20:92, 2007. DOI: 10.1088/0953-2048/20/1/017.

[64] G.A. Levin, P.N. Barnes, and J.S. Bulmer. Current sharing between superconducting film and normal metal. *Superconductor science and technology*, 20:757, 2007. DOI: 10.1088/0953-2048/20/8/006.

[65] F.P. Incropera, D.P. DeWitt, T.L. Bergman, and A.S. Lavine. *Fundamentals of Heat and mass transfer*. John Wiley & Sons, Ney-York, N.Y., 6th edition, 2007.

[66] V.K. Dhir. Boiling heat transfer. *Annual Review of Fluid Mechanics*, 30:365, 1998. DOI: 10.1146/annurev.fluid.30.1.365.

[67] J.W Westwater and J.G Santangelo. Photographic study of boiling. *Industrial & Engineering Chemistry Ressearch*, 47(8):1605, 1955. DOI: 10.1021/ie50548a043.

[68] C. Schmidt. Transient heat transfer to liquid helium and temperature measurement with a response time in the microsecond region. *Applied Physics Letters*, 32(12):827, 1978. DOI: 10.1063/1.89939.

[69] A. Sakurai and M. Shiotsu. Transient pool boiling heat transfer, part l: Incipient boiling superheat. *Journal of Heat Transfer*, 99:547, 1977.

[70] S. Wipf. Stability of the superconductive operating mode in high current-density devices. *IEEE Transactions on Magnetics*, 15(1):379, 1979.

[71] Z.J.J. Stekly, R. Thome, and B. Strauss. Principle of stability in cooled superconducting magnets. *Journal of Applied Physics*, 40(5):2238, 1969. DOI: 10.1063/1.1657964.

[72] B.J. Maddock, G.B. James, and W.T. Norris. Superconductive composites: Heat transfer and steady state stabilization. *Cryogenics*, 9(4):261, 1969. DOI: 10.1016/0011-2275(69)90232-X.

[73] L. Dresner. *Stability of superconductors*. Selected topics in superconductivity. Plenum Press, Ney-York, N.Y., 1995.

[74] M.N Wilson and Y. Iwasa. Stability of superconductors against localized disturbances of limited magnitude. *Cryogenics*, 18(1):17, 1978. DOI: 10.1016/0011-2275(78)90132-7.

[75] W.H. Cherry and J-I-Gittleman. Thermal and electrodynamic aspect of the superconductive transition process. *Solid-State Electronics*, 1(4):287, 1960. DOI: 10.1016/0038-1101(60)90071-X.

[76] Y. Iwasa. *Case studies in superconducting magnets*. Selected topics in superconductivity. Plenum Press, Ney-York, N.Y., 1994.

[77] J.N. Reddy. *An introduction to the finite element method*. McGraw-Hill, New-York, N.Y., 3nd edition, 2006.

[78] F. Roy, M. Therasse, B. Dutoit, F. Sirois, L. Antognazza, and M. Decroux. Numerical studies of the quench propagation in coated conductors for fault current limiters. *IEEE Transactions on Applied Superconductivity*, 19(3):2496, 2009. DOI: 10.1109/TASC.2009.2019600.

[79] R. Brambilla, F. Grilli, and L. Martini. Development of an edge-element model for AC loss computation of high-temperature superconductors. *Superconductor Science and Technology*, 20:16, 2007. DOI: 10.1088/0953-2048/20/1/004.

[80] Z. Hong, Q. Jiang, R. Pei, A.M. Campbell, and T.A. Coombs. A numerical method to estimate AC loss in superconducting coated conductors by finite element modelling. *Superconductor Science and Technology*, 20:331, 2007. DOI: 10.1088/0953-2048/20/4/006.

[81] F. Roy, B. Dutoit, F. Grilli, and F. Sirois. Magneto thermal modeling of second-generation HTS for resistive fault current limiter design purpose. *IEEE Transactions on Applied Superconductivity*, 18(1):29, 2008. DOI: 10.1109/TASC.2008.917576.

[82] A.D. Polyanin. *Handbook of Linear Partial Differential Equations for Engineers and Scientists*. Chapman & Hall/CRC Press, Boca Raton, FL., 2002.

[83] F. Sirois and F. Grilli. Numerical considerations about using finite-element methods to compute ac losses in hts. *IEEE Transactions on Applied Superconductivity*, 18(3):1733, 2008. DOI: 10.1109/TASC.2008.2001740.

[84] A. Kuršumović, R.P. Baranowski, B.A. Glowacki, and J.E. Evetts. Current transfer at superconducting $Bi_2Sr_2CaCu_2O_{8+\delta}$-Ag joints. *Journal of Applied Physics*, 86(3):1569, 1999. DOI: 10.1063/1.370929.

[85] L.A. Angurel, M. Bona, J.M. Andrés, D. Mu noz Rojas, and N. Casa n Pastor. High quality silver contacts on ceramic superconductors obtained by electrodeposition from non-aqueous solvents. *Superconductor Science and Technology*, 18:135, 2005. DOI: 10.1088/0953-2048/18/1/021.

[86] M. Polak, P. N. Barnes, and G.A. Levin. YBCO/Ag boundary resistivity in YBCO tapes with metallic substrates. *Superconductor Science and Technology*, 19(8):817, 2006. DOI: 10.1088/0953-2048/19/8/022.

[87] G.A. Levin, K.A. Novak, and P.N. Barnes. The effects of superconductor-stabilizer interfacial resistance on the quench of a current-carrying coated conductor. *Superconductor Science and Technology*, 23:014021, 2010. DOI: 10.1088/0953-2048/23/1/014021.

[88] COMSOL MULTIPHYSICS™. [Online]. http://www.comsol.com.

[89] E.M. Wray. Real phase diagrams (teaching demonstration). *Physics Education*, 7(4):243, 1972. DOI: 10.1088/0031-9120/7/4/010.

[90] Y.S. Touloukian, editor. *Thermophysical properties of matter*. IFI/Plenum, New-York, N.Y., 1970.

[91] D.R. Lide, editor. *CRC Handbook of chemistry and physics*. CRC Press, New-York, N.Y., 30th edition, 2010. http://www.hbcpnetbase.com/.

[92] United-States Naval Research Laboratory. The 1212c [yba2cu3o7-x] high-tc structure. [Online]. http://cst-www.nrl.navy.mil/lattice/struk/hightc/x1212c.html.

[93] J.E. Gordon, R.A. Fisher, S. Kim, and N.E. Phillips. Lattice and electronic specific heat of $YBa_2Cu_3O_{7-\delta}$. *Physica C*, 162-164:484, 1989. DOI: 10.1016/0921-4534(89)91117-9.

[94] S. J. Hagen, Z.Z Wang, and N.P. Ong. Anisotropy of the thermal conductivity of $YBa_2Cu_3O_{7-y}$. *Physical Review B*, 40(13):9389, 1989. DOI: 10.1103/PhysRevB.40.9389.

[95] T.A. Friedmann, M.W. Rabin, J. Giapintzakis, J.P. Rice, and D.M. Ginsberg. Direct measurement of the anisotropy of the resistivity in the a-b plane of twin-free, single-crystal, superconducting $YBa_2Cu_3O_{7-\delta}$. *Physical Review B*, 42(10):6217, 1990. DOI: 10.1103/PhysRevB.42.6217.

[96] D.K. Smith and H.R. Leider. Low-temperature thermal expansion of LiH, MgO and CaO. *Journal of Applied Crystallography*, 1(4):246, 1968. DOI: 10.1107/S0021889868005418.

[97] HAYNES INTERNATIONAL INC. Brochure H-2002D. [Online], 2002. http://www.haynesintl.com/pdf/h2002.pdf.

[98] J. Lu, E.S. Choi, and H.D. Zhou. Physical properties of Hastelloy® C-276™ at cryogenic temperatures. *Journal of Applied Physics*, 103:064908, 2008. DOI: 10.1063/1.2899058.

[99] E.R. Dobrovinskaya, L.A. Lytvynov, and V. Pishchik. *Sapphire: Material, Manufacturing, Applications*. Springer, Ney-York, N.Y., 2009. DOI: 10.1007/978-0-387-85695-7.

[100] C.N. Whetstone and C.E. Roos. Thermal phase transition in superconducting Nb-Zr alloys. *Journal of Applied Physics*, 36(3):783, 1965. DOI: 10.1063/1.1714218.

Curriculum Vitæ

Personal Informations:

Name	François Roy
Date of birth	21.06.1979
Place of origin	Québec, Qc. Canada
Nationality	Canadian
Adress	EPFL-IC-LANOS BC building, Station 14 1015, Lausanne, Switzerland francois.roy@epfl.ch

Education:

2000-2004	B.Eng. Physical engineering. Université Laval. Québec, Qc. Canada
2004-2006	M.Sc. Energy & Materials Sciences. Institut National de la Recherche Scientifique centre ÉMT. Varennes, Qc. Canada
2007-2010	Ph.D. Sciences. École Polytechnique Fédérale de Lausanne (EPFL). Lausanne, Switzerland

Publications:

1- F. Roy, G. Abel, B. Terreault, A. Reguer, J.-L. Meunier, M. Bolduc and G.G. Ross. Online system for temperature and accumulated dose control in plasma-based ion implantation. *Review of Scientific Instruments*, **78**:023905. 2007. DOI: 10.1063/1.2472601.

2- F. Sirois and F. Roy. Computation of 2-D Current Distribution in Superconductors of Arbitrary Shapes Using a New Semi-Analytical Method. *IEEE transactions on Applied Superconductivity*, **17**(3):3836. 2007. DOI: 10.1109/TASC.2007.902117.

3- F. Roy, B. Dutoit, F. Grilli and F. Sirois. Magneto-Thermal Modeling of Second-Generation HTS for Resistive Fault Current Limiter Design Purposes. *IEEE transactions on Applied Superconductivity*, **18**(1):1. 2008. DOI: 10.1109/TASC.2008.917576.

4- F. Sirois, M. Dione, F. Roy, F. Grilli and B. Dutoit. Evaluation of two commercial finite element packages for calculating AC losses in 2-D high temperature superconducting strips. *Journal of Physics: Conference Series*, **97**:012030. 2008. DOI: 10.1088/1742-6596/97/1/012030.

5- F. Roy, B. Dutoit, F. Grilli and F. Sirois. Magneto-thermal finite element modeling of 2nd generation HTS for FCL design purposes. *Journal of Physics: Conference Series*, **97**:012286. 2008. DOI: 10.1088/1742-6596/97/1/012286.

6- F. Sirois, F. Roy and B. Dutoit. Assessment of the Computational Performances of the Semi-Analytical Method (SAM) for Computing 2-D Current Distributions in Superconductors. *IEEE transactions on Applied Superconductivity*, **19**(3):1051. 2009.
DOI: 10.1109/TASC.2009.2019582.

7- F. Roy, M. Therasse, B. Dutoit, F. Sirois, L. Antognazza and M. Decroux. Numerical Studies of the Quench Propagation in Coated Conductors for Fault Current Limiters. *IEEE Transactions on Applied Superconductivity*, **19**(3):2496. 2009. DOI: 10.1109/TASC.2009.2019600

8- L. Antognazza, M. Therasse, M. Decroux, F. Roy, B. Dutoit, M. Abplanalp and ø. Fisher. Comparison between the behavior of HTS thin film grown on sapphire and coated conductors for fault current limiter applications. *IEEE Transactions on Applied Superconductivity*, **19**(3):1960. 2009. DOI: 10.1109/TASC.2009.2018113

9- F. Roy, S. Pérez, M. Therasse, B. Dutoit, F. Sirois, M. Decroux and L. Antognazza. Quench propagation in coated conductors for fault current limiters. *Physica C*, **469**(15-20):1462. 2009.
DOI: 10.1016/j.physc.2009.05.066.

10- F. Sirois, J. Coulombe, F. Roy and B. Dutoit. Characterization of the electrical resistance of high temperature superconductor coated conductors at high currents using ultra-fast regulated current pulses. *Superconductor Science and Technology*, **23**(3):034018. 2010.
DOI: 10.1088/0953-2048/23/3/034018.

11- F. Roy, F. Sirois and B. Dutoit. Quench nucleation obtained by local reduction of I_c in coated conductors. *Journal of Physics: Conference Series*, in press. 2010.